



JOHANNES GUTENBERG
UNIVERSITÄT MAINZ

The scintillating fiber focal plane detector for the use of Kaos as a double arm spectrometer

Dissertation
zur Erlangung des Grades
“Doktor der Naturwissenschaften”
am Fachbereich Physik
der Johannes Gutenberg-Universität Mainz

von Carlos Antonio Ayerbe Gayoso
gb. in Caracas, Venezuela

Institut für Kernphysik
Johannes Gutenberg-Universität Mainz Mainz,
dem 25. Mai 2012

Zusammenfassung

Der Erweiterung des Elektronenbeschleunigers Mainzer Mikrotron (MA-MI) im Jahre 2007 auf Strahlenergien bis 1.5 GeV erlaubt es, Kanäle mit Strangeness-Produktion durch elektromagnetische Prozesse zu untersuchen. Das Kaonenspektrometer KAOS, welches von der A1-Kollaboration betrieben wird, ermöglicht einen effizienten Nachweis von Kaonen aus Elektroproduktion. Als Einarm-Spektrometer kann es zusammen mit den bestehenden hochauflösenden Spektrometern benutzt werden, um exklusive Messungen im zugänglichen kinematischen Bereich durchzuführen.

Um die Hyperkernproduktion in der Reaktion ${}^AZ(e, e'K^+)_{\Lambda}{}^A(Z-1)$ zu untersuchen, ist der Nachweis von Elektronen unter sehr kleinen Vorwärtswinkeln erforderlich. Hierfür ist die Verwendung von KAOS als Zweiarm-Spektrometer für den gleichzeitigen Nachweis von Kaonen und Elektronen unerlässlich. Daher wurde der Elektronarm mit einem neuen Dektorsystem ausgestattet, das hohe Zählraten verarbeiten kann und über eine große Granularität verfügt, um eine gute Ortsauflösung zu erzielen. Zu diesem Zwecke wurde als Elektrondetektor ein Hodoskop aus szintillierenden Fasern entwickelt.

Das Hodoskop besteht aus zwei Ebenen mit insgesamt 18432 szintillierenden Doppelkernfasern mit einem Durchmesser von 0.83 mm. Jede Ebene besteht aus 72 Modulen. Jedes Modul wiederum besteht aus einem Bündel aus mehreren Lagen, welche um 60° versetzt sind. Jeweils vier Fasern sind zu einer gemeinsamen Auslese zusammengefasst. Die Auslese erfolgt über 32-kanalige Linear-Array-Multianoden-Photomultiplier. Die Signale werden mit einem neu entwickelten Zwei-Schwellen-Diskriminator verarbeitet und parallel weitergeleitet zu totzeitfreien TDC-Modulen und Logikmodulen zu Triggerzwecken.

Tests mit Fasermodulen an einem Kohlenstoffstrahl an der GSI ergaben eine Zeitauflösung von etwa 200 ps (FWHM) und eine Ortsauflösung von etwa $270 \mu\text{m}$ bei einer Nachweiseffizienz von $\epsilon > 99\%$.

Die Beschreibung dieses Spektrometerarms wurde über Simulationen erreicht. Die Transfermatrix für die Spurparameter von der Fokalebene des Faserdetektors bis zum primären Vertex wurde in erster Ordnung mittels Strahltransport-Optik berechnet und überprüft durch eine Messung der quasielastischen Streuung an einem Kohlenstofftarget, wobei die Kinematik vollständig bestimmt wurde durch Messung des Impulses des Rückstoßprotons. Bei diesem erste Test wurde festgestellt, dass die Genauigkeit für die Rekonstruktion der Parameter am quasielastischen Vertex etwa 0.3% beträgt.

Der Entwurf, der Aufbau, die Inbetriebnahme, die Tests und die Charakterisierung des Faserhodoskops werden in dieser Arbeit vorgestellt, die am Institut für Kernphysik an der Johannes Gutenberg-Universität Mainz durchgeführt wurde.

Abstract

The upgrade of the Mainz Mikrotron (MAMI) electron accelerator facility in 2007 which raised the beam energy up to 1.5 GeV, gives the opportunity to study strangeness production channels through electromagnetic process. The Kaon Spectrometer (KAOS) managed by the A1 Collaboration, enables the efficient detection of the kaons associated with strangeness electroproduction. Used as a single arm spectrometer, it can be combined with the existing high-resolution spectrometers for exclusive measurements in the kinematic domain accessible to them.

For studying hypernuclear production in the ${}^AZ(e, e'K^+)_{\Lambda}{}^A(Z-1)$ reaction, the detection of electrons at very forward angles is needed. Therefore, the use of KAOS as a double-arm spectrometer for detection of kaons and the electrons at the same time is mandatory. Thus, the electron arm should be provided with a new detector package, with high counting rate capability and high granularity for a good spatial resolution. To this end, a new state-of-the-art scintillating fiber hodoscope has been developed as an electron detector.

The hodoscope is made of two planes with a total of 18432 scintillating double-clad fibers of 0.83 mm diameter. Each plane is formed by 72 modules. Each module is formed from a 60° slanted multi-layer bundle, where 4 fibers of a tilted column are connected to a common read out. The read-out is made with 32 channels of linear array multianode photomultipliers. Signal processing makes use of newly developed double-threshold discriminators. The discriminated signal is sent in parallel to dead-time free time-to-digital modules and to logic modules for triggering purposes.

Two fiber modules were tested with a carbon beam at GSI, showing a time resolution of ~ 220 ps (FWHM) and a position residual of ~ 270 μ m (FWHM) with a detection efficiency $\varepsilon > 99\%$.

The characterization of the spectrometer arm has been achieved through simulations calculating the transfer matrix of track parameters from the fiber detector focal plane to the primary vertex. This transfer matrix has been calculated to first order using beam transport optics and has been checked by quasielastic scattering off a carbon target, where the full kinematics is determined by measuring the recoil proton momentum. The reconstruction accuracy for the emission parameters at the quasielastic vertex was found to be on the order of 0.3% in first test realized.

The design, construction process, commissioning, testing and characterization of the fiber hodoscope are presented in this work which has been developed at the Institut für Kernphysik of the Johannes Gutenberg - Universität Mainz.

Contents

1	Experimental facility in Mainz	1
1.1	MAMI	1
1.2	The A1 Collaboration	3
1.2.1	The three spectrometers facilities at MAMI	3
1.2.1.1	Optical properties	4
1.2.1.2	Detector package	5
1.2.2	The Kaon Spectrometer	8
1.2.2.1	Kaon Spectrometer (KAOS) in Mainz	8
1.2.2.2	Detector package of KAOS	10
1.2.2.3	Modifications to the beam line	16
2	The Scintillator Fiber Hodoscope	19
2.1	Scintillator Fibers	19
2.1.1	The Kuraray SCSF-78M fiber	23
2.2	Readout electronics	24
2.2.1	The Hamamatsu H7259K photomultiplier	26
2.2.1.1	The HVSys voltage multiplier cell.	28
2.2.2	Front-end board	29
2.3	Data Acquisition	30
2.3.1	Double threshold discriminator	30
2.3.1.1	Double Threshold Discriminator operation principle	32
2.3.2	CATCH Time Digital Converter	36
2.3.3	VME Universal PROcessing Module (VUPROM) Logic Module	37
2.4	Design and Construction of the fiber detector	38
2.4.1	Design of the fiber bundle	38
2.4.1.1	Fibers bundles designed in Mainz	43
2.4.2	Increasing the Light yield	44
2.4.3	Design concept of the fiber hodoscope	48
2.5	Construction of the fiber detector	52

2.5.1	Construction of the fiber bundle	52
2.5.2	Polish of the end side of the bundle	53
2.5.3	Assembly of the fiber bundle with the cookie	53
2.5.4	Bending of the fiber bundle and gluing to the cookie . . .	56
2.5.5	Aluminization of the fiber bundles	59
2.5.6	Alignment of the PhotoMultiplier Tube (PMT) along the fiber bundle	59
2.5.7	Assembly of the fiber hodoscope	63
2.6	Calibration of the fiber detector	64
2.6.1	Position calibration	67
2.6.2	Multi anode PhotoMultiplier (MaPMT) gain measurement and High Voltage (HV) calibration	69
2.7	Fiber detector set-up	71
3	Beam tests at GSI	77
3.1	1st Performance test at GSI	77
3.2	2nd Performance test at GSI	80
3.3	Conclusions from the performance tests	82
4	Electron-Arm Spectrometer	85
4.1	Fiber detector trigger	85
4.1.1	Trigger Control System	88
4.2	In-beam tests at MAMI	90
4.2.1	Background sources and trigger signal filtering	91
4.2.2	2010 beam test	94
4.3	Monte-Carlo simulation of the fiber detector	97
4.4	Fiber detector magnet-optics in KAOS	102
4.4.1	Theory of charged beam transport optics	102
4.4.1.1	Equation of motion in a magnetic field	102
4.4.1.2	Solution and matrix formalism for the trajectory of a charged particle through a magnetic field	102
4.4.2	Characterization of the fiber detector in KAOS	105
5	Summary	115
A	Technical drawings	117
A.1	The fiber-photomultiplier interface	117
A.2	Position matrix plate	117
A.3	Supporting plate	118
A.4	Vacuum chamber	118
B	DTD piggyback channels mapping	127

List of Figures

1.1	Scheme of a microtron race track accelerator	2
1.2	Scheme of the HDSM (MAMI-C)	2
1.3	Floor plan of the MAMI facility and the experimental halls of the Institut für Kernphysik of Mainz (IKPH)	4
1.4	Panoramic view of the three spectrometers hall with the KAOS spectrometer	5
1.5	The drawing of spectrometer's detector package	7
1.6	KAOS platform at measurement position	9
1.7	KAOS entrance window. Collimator ladder and vacuum chamber extention.	10
1.8	Scheme of the working principle of the Multi Wire Proportional Chambers (MWPC)	11
1.9	Plot of the minimum momentum for Cerenkov light production.	13
1.10	Drawing of the diffusion box of the Cerenkov detector.	14
1.11	Photographs of the hadron arm instrumentation of KAOS.	15
1.12	Scheme of the chicane.	17
1.13	Photography of the chicane.	18
2.1	Energy diagram of the process of scintillation	21
2.2	Scheme of the total reflection by light emitted on axis.	22
2.3	Emission spectrum of SCSF-78M fiber.	24
2.4	Linear multianode photomultiplier tube	26
2.5	The H7259K photomultiplier tube	26
2.6	Quantum efficiency and cathode radiant sensitivity of the H7260 phototubes family	27
2.7	Mean value of the output deviation of the anode signal from the phototubes purchased in Mainz	27
2.8	The HVSys voltage multiplier cell	29
2.9	The HVSys512 module	30
2.10	Front-end board	31
2.11	Double Threshold Discriminator	33

2.12	Discriminators Controller Board	34
2.13	DTD operation principle	35
2.14	TDC-CMC card	36
2.15	CATCH working scheme	37
2.16	VUPROM module	39
2.17	Different fibers geometries with inclined columns	40
2.18	Pitch and overlap fraction of the column pitch as a function of the column angle	41
2.19	Mass thickness for $\phi = 0^\circ, 45^\circ, 60^\circ$ and 70° fiber array geometries	42
2.20	Channels multiplicity and efficiency for fiber arrays with slanted columns at $\phi = 45^\circ$ and 60° in function of incident particle angle.	43
2.21	Scheme and picture of the 0° fiber arrangement	44
2.22	Scheme and picture of the 45° fiber arrangement	45
2.23	Scheme and picture of the 60° fiber arrangement	45
2.24	Reflectance spectra of aluminium and silver as a function of wavelength	46
2.25	Vacuum chamber for aluminium vaporization and electrode detail.	47
2.26	Photograph of two vaporized bundles and on without. Logarithmic plot of the Analog Digital Converter (ADC) output before and after the aluminium vaporization.	48
2.27	Computer-Aided Design (CAD) detail drawing of the fiber detector respect to the focal plane	50
2.28	Photography of a bending test of the fibers.	51
2.29	Hit pattern of 3 consecutive bundles on a test beam and mean value.	51
2.30	Photography of the position matrix and cross section detail.	52
2.31	Scheme of the fiber bundle with dummies.	52
2.32	Steps of fiber bundle construction	54
2.33	Polish phase of the end of the fiber bundle	55
2.34	Placing of the fibers into the cookie	56
2.35	Photography of the aluminium plate with the bundle.	57
2.36	Bundle into the oven and glue application	58
2.37	Detail of the cookie polished.	58
2.38	Preparation before the aluminization and photography after the process	60
2.39	Cookie with fasten aluminium plates and PMT fastened	60
2.40	Asymmetry measurement plot from an aligned PMT.	61
2.41	Photography of the module assembled and aligned.	61
2.42	Construction flowchart.	62
2.43	Scheme of how the stress and verticality depends on the starting point of gluing.	63
2.44	Fiber detector plane in a frame.	64
2.45	Photographs of the gluing of the bundles to make the focal plane.	65

2.46	Calibration flowchart.	66
2.47	Fiber detector calibration set-up.	67
2.48	Typical hit position distribution and calibration	68
2.49	Deviation of the channel positions for a complete fiber detector plane.	69
2.50	Typical ADC distribution for signal height measurement of one channel.	72
2.51	Measured signal heights for the 2304 channels of one detector plane.	72
2.52	Relative signal height as a function of the applied voltage.	73
2.53	Measured signal heights of three neighboring modules before and after the voltage adjustment.	73
2.54	Scheme of how to connect the RJ-45 cables in the triple board.	74
2.55	Scheme of the connection of a single module.	75
2.56	Photographs of the cabling of the fiber detector in KAOS.	76
3.1	Layout of the three fiber bundles forming two detection planes.	77
3.2	Photograph of the fiber detector used at Gesellschaft für Schwer-Ionenforschung (GSI) and photograph of the piggyback board for analog output from the Double Threshold Discriminator (DTD)	78
3.3	Residual time and track position of the fiber detector from the ^{12}C beam test at GSI	79
3.4	Gray-scale plot showing the strong correlation between the hit time defining channel and the channel of maximum pulse height in detector plane A. Figure from [124].	80
3.5	Photograph of the fibers bundle for the test in Cave A of GSI	81
3.6	Residual time and track position of the fiber detector from the cocktail beam and ^{12}C beam test at Cave A at the GSI	81
3.7	Multiplicity of the two planes of the fiber detector test in Cave A of the GSI with a cocktail beam	82
3.8	Residual track position of the fiber detector and sum pulse height distribution over all channels from the cocktail beam at Cave A at the GSI	83
4.1	Trigger scheme used during the beam-test of the electron-arm detectors	86
4.2	Scheme of the logic unit for finding clusters.	87
4.3	Composition of the different stages of the trigger system	89
4.4	CAD drawing of the set-up of the in-beam test	90
4.5	Plot of scatter Møller electron energy vs laboratory scatter angle	92
4.6	Møller scattering production cross section	93
4.7	Rate comparison of signals in X-plane during 2009 beam time	94
4.8	Typical event display of the fiber detector.	95
4.9	X plane vs Θ -plane hits plots for different KAOS magnetic field	96

4.10	Scheme for incident angle reconstruction	97
4.11	Reconstructed incident particle angle plot	98
4.12	Scheme of the relation between cartesian angles and spherical angle	99
4.13	Pictures from the GEometry ANd Tracking (Geant4) simulation of the KAOS spectrometer	100
4.14	Correlation hits between fiber detector planes and reconstructed angle. Overlap between real and simulated data.	101
4.15	Coordinate system used in the derivation of the equations of motion	103
4.16	Momentum acceptance for different magnetic fields	106
4.17	Momentum acceptance reduced with respect to the central momentum	107
4.18	Angular acceptance as a function of different momenta	107
4.19	Momentum angular acceptance as a function of different emission angle	108
4.20	Variation of the path length with respect to the position corrected, for different emission angles	109
4.21	Variation of the path length with respect to the reduced momentum, for different emission angles	109
4.22	Variation of the path length with respect to the emission angle, for different momenta	110
4.23	Graphical scheme how to determine the transfer matrix elements	111
4.24	Proton momentum reconstructed	113
4.25	Beam energy reconstructed	114
4.26	Emission angle reconstructed	114
A.1	Picture of the cookie.	118
A.2	Crimping column for the fiber plane	119
A.3	Photography of the new vacuum chamber.	119
A.4	CAD drawing of the cookie.	120
A.5	CAD drawing of the aluminium clamping plates.	121
A.6	CAD drawing of the supporting plate.	122
A.7	CAD drawing of the supporting plate.	123
A.8	CAD drawing of the new vacuum chamber.	124
A.9	CAD drawing of the new vacuum chamber.	125
B.1	Connection scheme of the DTD piggyback	128

List of Tables

1.1	Summary of the characteristics of MAMI	3
1.2	Main parameters and CAD scheme of the magnetic spectrometers A,B, C	6
2.1	SCSF-78M characteristics.	25
2.2	H7260K characteristics.	28
4.1	Measured Trigger Rates in the Electron-Arm of the KAOS spectrometer during beam tests in 2009	97
4.2	Transfer matrix elements for the KAOS spectrometer.	110
4.3	Backward transfer matrix elements for the KAOS spectrometer. .	112

Acronyms

ADC Analog Digital Converter

BNL Brookhaven National Laboratory

CAD Computer-Aided Design

CATCH COMPASS Accumulate Transfer and Control Hardware

CEBAF Continuous Electron Beam Accelerator Facility

CERN European Organization for Nuclear Research

COMPASS COMmon Muon Proton Apparatus for Structure and Spectroscopy

CPLD Complex Programmable Logic Devices

CPU Central Process Unit

DAC Digital Analog Converter

DAΦNE Double Annular ring for Nice Experiments

DAQ Data Acquisition

DSP Digital Signal Processor

DTD Double Threshold Discriminator

FIFO First In - First Out

FINUDA Fisica Nucleare a DAΦNE

FLT First Level Trigger

FPGA Field Programmable Gate Array

Geant4 GEometry ANd Tracking

GEM Gas Electron Multiplier

GSI Gesellschaft für SchwerIonenforschung now GSI Helmholtzzentrum für
Schwerionenforschung

HKS High Resolution Kaon Spectrometer

HMS High Momentum Spectrometer

HV High Voltage

IKPH Institut für Kernphysik of Mainz

JLab Thomas Jefferson National Accelerator Laboratory

JTAG Joint Test Action Group

KAOS Kaon Spectrometer

KEK High Energy Accelerator Research Organization

LVDS Low Voltage Differential Signal

MaPMT Multi anode PhotoMultiplier

MAMI Mainzer Mikrotron

MWPC Multi Wire Proportional Chambers

PMT PhotoMultiplier Tube

PWD Pulse-Width Discriminator

QCD Quantum Chromodynamics

SOS Short Orbit Spectrometer

TDC Time to Digital Converter

TDC-CMC TDC-CATCH Mezzanine Card

TCS Trigger Control System

TOF Time of Flight

VDC Vertical Drift Chamber

VHDCI Very High Density Cable Interconnect

VUPROM VME Universal PROcessing Module

Experimental facility

1.1 MAMI

The Mainzer Mikrotron (MAMI) is an electron accelerator complex operated by the Institut für Kernphysik of the Johannes Gutenberg Universität Mainz. It consists in a electron source with a linear accelerator (linac), three constant wave (cw) race track microtrons (RTM) and the new concept of Harmonic Double Sided Microtron (HDSM).

The electron source delivers a beam current up to $100 \mu\text{A}$ from thermionic source and $40 \mu\text{A}$ based on photoelectron emission from a GaAsP cathode with 80% polarization, then accelerated by a linac to 3.5 MeV directed to the first RTM [76].

The RTM is an accelerator evolved from the concept of microtron¹ in order to reduce the technical and economic limitations due to the increment of the size of the magnets and therefore the increased energy of the particles. In this case, the magnet of the microtron is divided in two halves and separated as shown in fig. 1.1. In the space within, on the common path to all orbits, a short linear accelerator allows the acceleration of particles, reducing the number of orbits necessary to reach higher energies [77].

The HDSM was developed to rise the energy of the electron beam up to 1.5 GeV with the stability provided by the last stage of MAMI, using the same design of the race track, which implies the construction of two magnets of 2000 t weight²[76]. The HDSM consists in 4 magnets, each of them bend the electron beam 90° ³ driving it within the same path at both sides of the

¹A microtron is an accelerator where particles increase their kinetic energy a constant amount by a radio frequency (rf) cavity within a constant magnetic field). Particles emerging from a source pass through the cavity and form a circular orbit which lead to the accelerating cavity due to the synchronicity condition given by the oscillating period for the rf.

²The size of a magnet is proportional to the third power of the bending radius which is direct proportional to the energy, therefore the mass of the desired magnet goes as the third power of the maximum energy of the particle.

³Instead than 180° as regular RTM

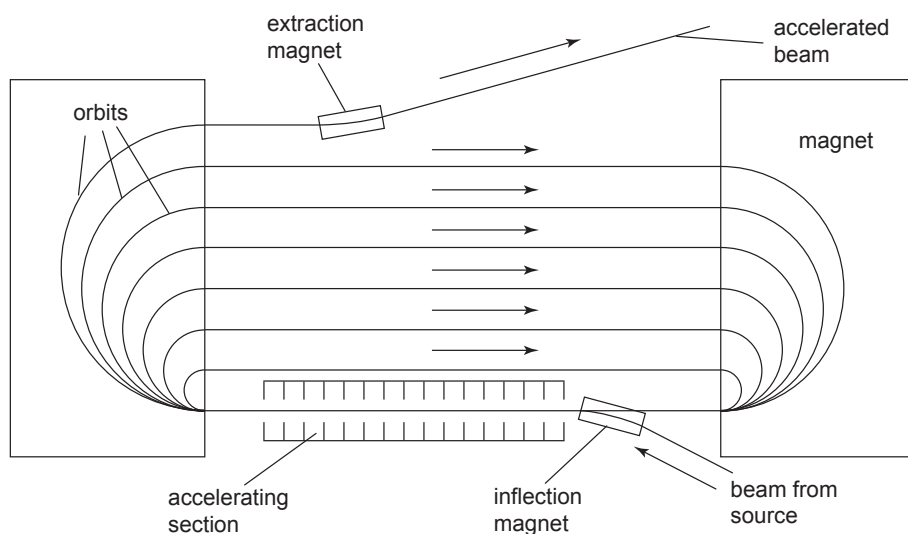


Figure 1.1: Scheme of a microtron race track accelerator, similar to the MAMI concept for the RTM stages.

system, and two linacs in the common beam paths (fig. 1.2). In order to have the highest longitudinal stability, the two linacs have a frequency relation of 2:1 with respect to the fundamental frequency of the linacs in the previous stages.

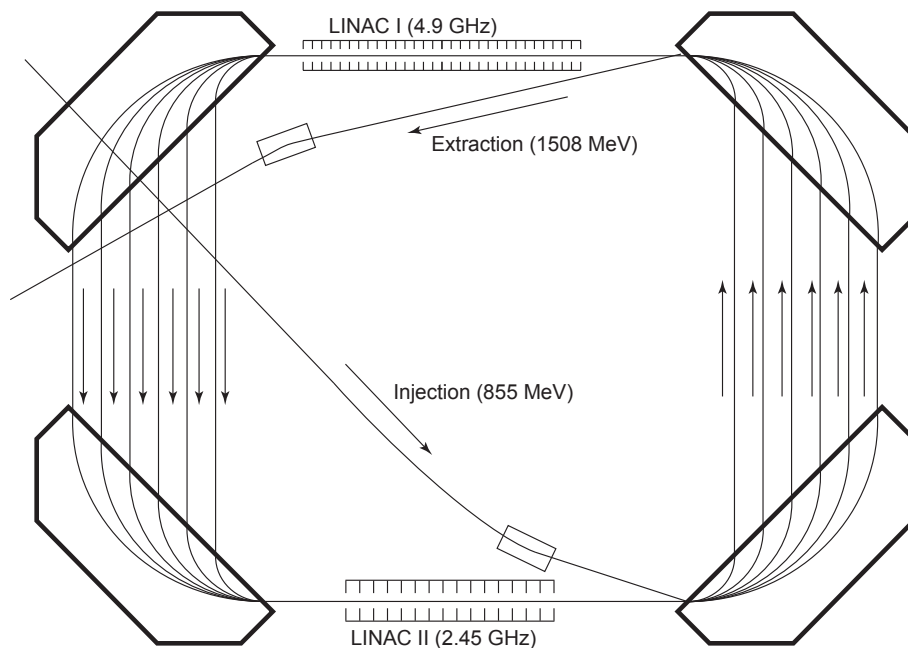


Figure 1.2: Scheme of the HDSM (MAMI-C). The beam coming from MAMI B at 855 MeV is injected in the machine and is accelerated after 43 rounds up to 1.5 GeV, then is extracted to the experimental halls.

The microtrons are connected in cascade in a way that each RTM works as a booster for the next RTM and finally to the HDSM. A summary of the characteristics of the 4 stages is given in table 1.1. The accelerator is able to

deliver beam in the range of 180 MeV to 1508 MeV in steps of approx 15 MeV with very good energy stability, 30 keV@855 MeV and 110 keV@1.5 GeV RMS.

Table 1.1: Summary of the characteristics of MAMI. (Source: B1 Collaboration (MAMI) [78])

	RTM1	RTM2	RTM3	HDSM
General	MAMI A1	MAMI A2	MAMI B	MAMI C
In/Output energy (MeV)	3.97/14.86	14.86/180	180/855.1	855.1/1508
No of recirculations	18	51	90	43
RF System				
Frequency (GHz)	2.45	2.45	2.45	2.45/4.90
No of Klystrons	1	2	5	4/5
Energy gain/turn	0.599	3.24	7.50	16.64-13.9

The MAMI accelerator delivers beam at present to three experimental halls, each of them directed by “collaborations” [79], as it can be seen in the fig. 1.3:

- A1: “Coincidence Experiments with Electrons”
Comprise the three spectrometers facility and the KaoS spectrometer, besides other detectors for specific coincidence experiments alongside the existing spectrometers [see section 1.2].
- A2: “Real Photons”
Consists principally in the Glasgow Tagger, the Cristal Ball developed in SLAC and the TAPS detector as a forward detector [80].
- A4: “Parity Violation Electron Scattering”
It comprises two halls to allocate the PbF_2 crystal calorimeter and the Compton polarimeter [81].

1.2 The A1 Collaboration

1.2.1 The three spectrometers facilities at MAMI

The A1 Collaboration is an experimental group of the Institut für Kernphysik in Mainz dedicated to coincidence experiments of fixed target with electrons. The collaboration operates the three high resolution magnetic spectrometers, which are labeled A, B and C [82], and since 2007, from GSI in Darmstadt, the spectrometer KAOS. The three spectrometers can rotate around the target and they can operate in single, double or triple coincidence mode

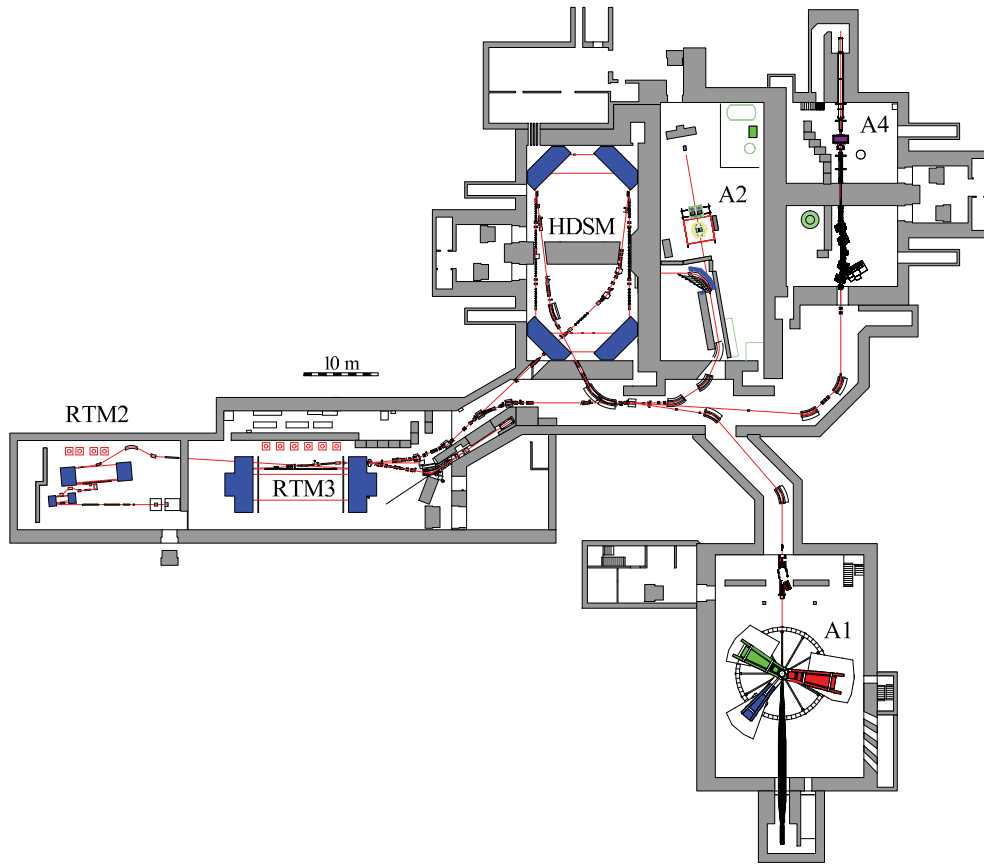


Figure 1.3: Floor plan of the MAMI facility and the experimental halls of the IKPH. Note that it does not show the modification done in the three spectrometers hall (A1) to include the KaoS spectrometer and the chicane in the beam line.

which allows an optimal setup for the study of fundamental properties of the nucleon as charge distribution by elastic form measurements and generalized polarizabilities by virtual Compton scattering. Also, the complex is optimal for study of resonance structure of the nucleon by meson production experiments. A proton recoil polarimeter, in combination with the polarized MAMI beam and a polarized helium-3 gas target, gives access to a broad variety of spin observables. A view of the hall is shown in fig. 1.4.

Next sections summarize the optical properties and the detector packages of the spectrometers A, B and C. KAOS spectrometer is described in section 1.2.2

1.2.1.1 Optical properties

Spectrometer A uses quadrupole-sextupole-dipole-dipole (QSDD) configuration of the magnets which enable measurement of high particle momenta and a relatively large acceptance (28 msr). Spectrometer B uses a single magnet (clam-shell dipole) which enables higher spatial resolution, but smaller



Figure 1.4: Panoramic view of the three spectrometers hall with the KAOS spectrometer showing the direction of the electron beam from MAMI (ca. 2009).

acceptance (5.6 msr). It is relatively compact so it can be positioned at small scattering angles (down to 7°). Spectrometer C is 11/14 down-scaled version of spectrometer A. Their main properties are summarized in table 1.2.

The central magnetic field in the spectrometers, and thus the central momentum, are determined by means of Hall and NMR probes. While the Hall probes give a rough measure of the magnetic field, the NMR makes very precise measurements with an error smaller than the energy spread of the electron beam.

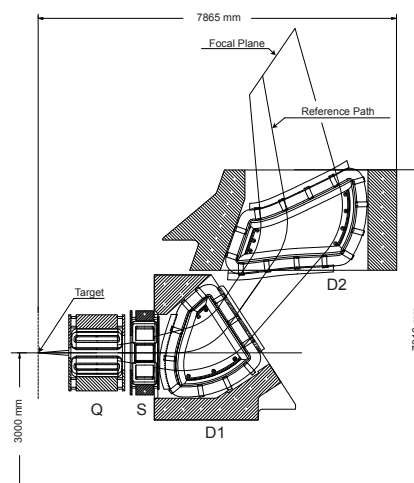
1.2.1.2 Detector package

All three spectrometers have similar detector packages consisting of four drift-chambers, scintillators and a Cerenkov detector. The drift-chambers are used for particle trajectory reconstruction and the scintillators for triggering and particle identification. As electrons (positrons) and pions cannot be distinguished by the scintillators, the Cerenkov detector is used to discriminate them. The detectors are schematically shown in the figure 1.5.

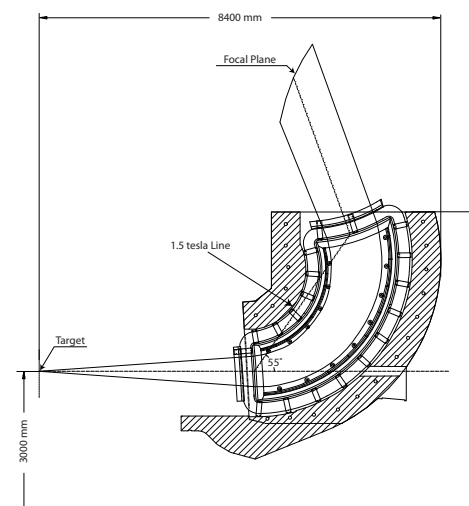
Vertical drift chambers. Two pairs of vertical drift chambers (VDC) are placed in the focal plane, which is inclined 45° with respect to the reference particle

Table 1.2: Main parameters and CAD scheme of the magnetic spectrometers A,C (up) and B (down). (Source [82]).

Spectrometer	A	C
Configuration	QSDD	QSDD
Max. momentum [MeV/c]	735	551
Cent. momentum [MeV/c]	665	490
Momentum acceptance [%]	20	25
Solid angle [msr]	28	28
Horiz. angl. accept. [mrad]	± 100	± 100
Vert. angl. accept. [mrad]	± 70	± 70
Scatt. angle range [°]	18-160	18-160
Momentum res.	$\leq 10^{-4}$	$\leq 10^{-4}$
Angular res. at target [mrad]	≤ 3	≤ 3
Position res. at target [mm]	3-5	3-5



Spectrometer	B
Configuration	D
Max. momentum [MeV/c]	870
Cent. momentum [MeV/c]	810
Momentum acceptance [%]	15
Solid angle [msr]	5.6
Horiz. angl. accept. [mrad]	± 20
Vert. angl. accept. [mrad]	± 70
Scatt. angle range [°]	7-62
Momentum res.	$\leq 10^{-4}$
Angular res. at target [mrad]	≤ 3
Position res. at target [mm]	1



trajectory. One chamber in each pair has wires in the non-dispersive direction, labeled as y_{fp} and the other has wires rotated 40° with respect to y_{fp} . The former is used to measure the track in the dispersive direction, while the later measures the projection of the track in the non-dispersive direction.

The VDCs consist of equally spaced signal and potential wires between cathode foils, placed in a gas mixture of argon and isobutane. The wires are grounded while the foils are set at negative potential of 5600-6500 V. When a particle traverses the chamber it produces ionization and the electrons drift towards the wires with a known velocity. Typically a particle induces signals in at least three and up to seven wires. The trigger is given by plastic scintillators placed behind the VDCs. The wires stop the time measurement started by the scintillators and the time information of each wire is translated into distance giving particle track. By using two pairs of chambers (instead of only one) the

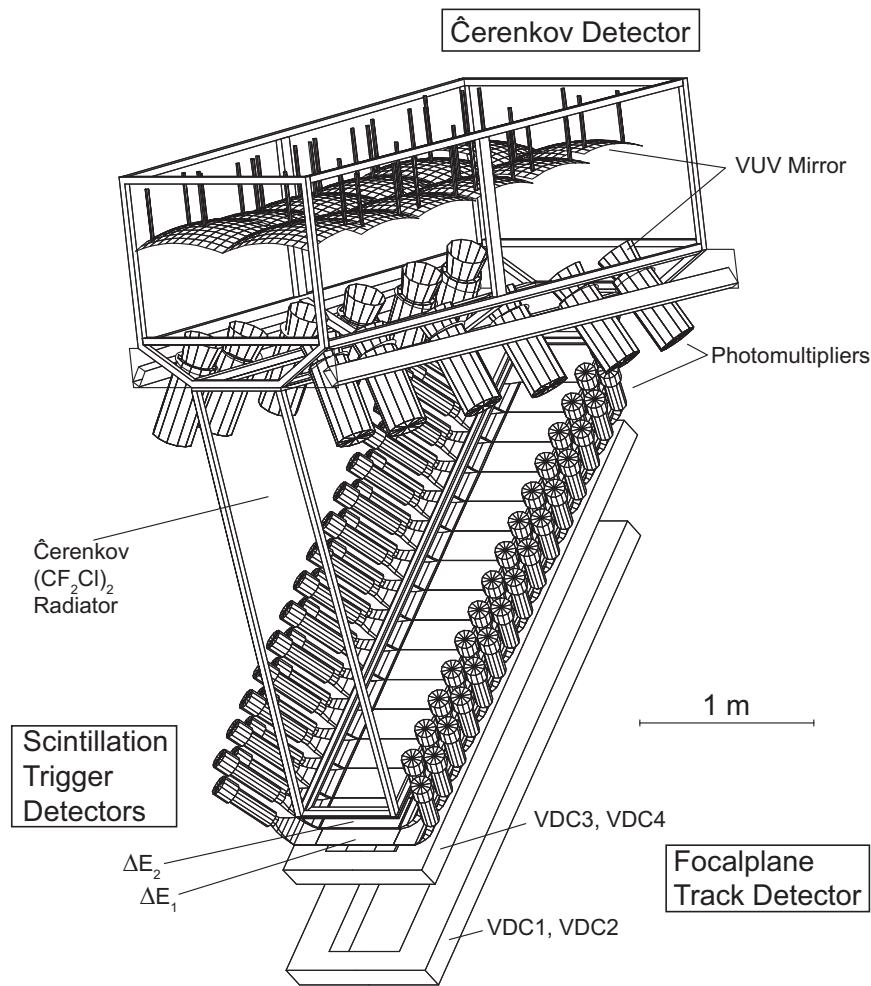


Figure 1.5: The drawing of spectrometer's detector package consisting of four VDCs, two layers of scintillators and a Cerenkov detector. Figure from A. Liesenfeld [82].

spatial resolution is increased by an order of magnitude and it is $\leq 200 \mu\text{m}$ in the dispersive and $\leq 400 \mu\text{m}$ in the non-dispersive direction. The focal plane coordinates measured by the VDCs are translated to the target coordinates by means of the magnetic field map [83, 84].

Scintillators. Two segmented planes of plastic scintillators are placed above the drift chambers. The detectors in the first plane (dE-plane) are 3 mm thick and those in the second plane (ToF-plane) are 1 cm thick. The segmentation (15 segments in spectrometers A and C, 14 segments in spectrometer B) enhances the time resolution and gives a rough position of the particle track.

The role of the scintillators is to provide the trigger for the time measurement in the VDCs, to provide time information for coincidence timing and to measure the energy deposition. Typically the second (thicker) layer gives the fast timing signal, but the first layer can also be used for low energy protons or

deuterons. The protons can be separated from minimum ionizing particles by their energy deposition in the two layers. The pions cannot be separated from electrons and positrons, therefore the Cerenkov detector has to be used [85].

Cerenkov detector. The Cerenkov detector contains gas $(CF_2Cl)_2$ in which electrons or positrons with energy > 10 MeV create Cerenkov light. The Cerenkov photons are transmitted through the gas, reflected by special mirrors and then collected by photomultipliers. The energy threshold lies at 2.7 GeV for pions, but pions with such energy are never produced by the 1.5 GeV beam. Consequently, only electrons or positrons can produce a signal in the Cerenkov detector and this fact is used to separate them from other particles.

1.2.2 The Kaon Spectrometer

The Kaon Spectrometer (KAOS) is a magnetic spectrometer developed at GSI, in Darmstadt and manufactured by DANFYSIK in Denmark in 1991. Due to the former experimental task at GSI, the optimal version of a compact size, large acceptance and double focussing magnetic spectrograph was found in a combination of a quadrupole and a dipole magnet. KAOS was designated to identify kaons in nuclear collisions with proton/pion/kaon ratio of $2 \times 10^6 / 2 \times 10^4 / 1$. The maximum dipole field is $B=1.95$ corresponding to a momentum of $p_{max}=1.6$ GeV/c for singly charged particles. It has a large momentum acceptance $p_{max}/p_{min} \approx 2$ and a solid angle $\Omega=35$ msr [72].

After a successful experimental program at GSI [73], KAOS was acquired by the IKPH in order to provide a complementary detection instrument for the three spectrometers facility due to upgrade of Mainzer Mikrotron (MAMI), extending the physics program to the strangeness flavor field.

1.2.2.1 KAOS in Mainz

Along May and June 2003 KAOS was dismantled from its location at GSI with its associated electronics and detectors and brought to Mainz.

Due to the characteristics of the three spectrometer hall, the existing supporting platform cannot be used. The new platform concept is designed with enough flexibility in such a way that it does not disturb the normal work of the other spectrometers. The concept design is based in a compact, mobile and adjustable platform with a support structure on hydraulic positioning cylinders. The platform with the magnet, the detectors and the front-end electronics, should move from a parking position, where the the spectrometers A, B and C can work in standard operation, to a measurement position through a hydraulic displacement system on segmented tracks (fig. ??).

At measurement position, the platform rests over three cylinders and they over positioning plates. This system allows a precise positioning and

alignment of the spectrometer. Also, it allows a precise vertical alignment of the magnet on the beam line level or up to 100 mm away from it. This displacement from the median plane is used to reduce the background rate in hypernuclear experiments (see sec. ?? and sec.4.2.1). Further the feet permit rotate the platform keeping the entrance side straight and perpendicular to the reference position pointing to the target (fig. 1.6).

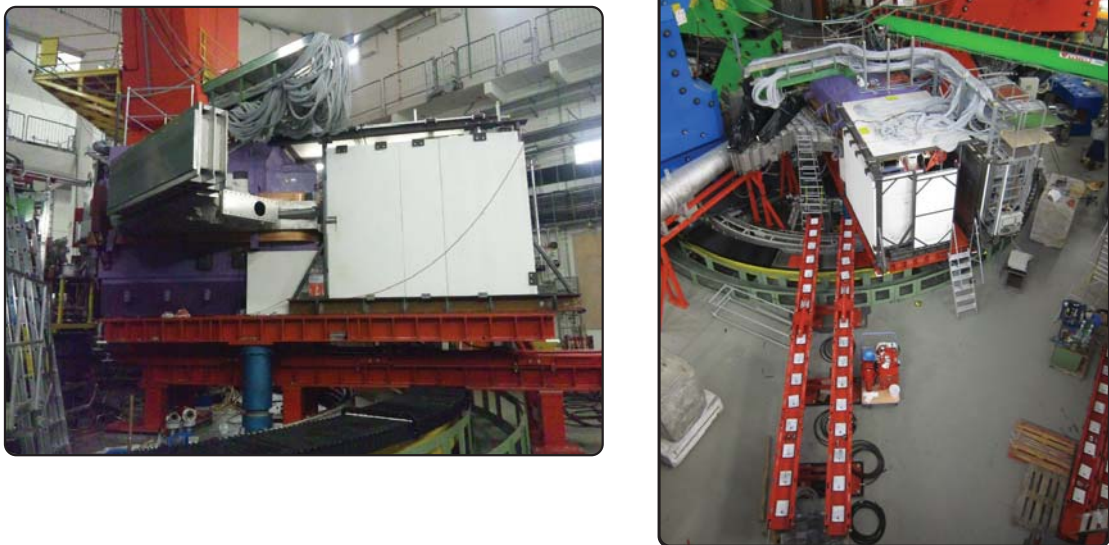


Figure 1.6: Right. Photography of KAOS in the platform at measurement position. Below the platform, in blue, can be seen one of the three supporting feet of the platform. Also below, is possible to see the end part of the position rails before retiring them. The white wall at right is a radiation protection for the detectors. Left. Photography of the platform rotated.

Unlike the former configuration at GSI, KAOS is used in Mainz without the quadrupole magnet at the entrance window. Instead, a collimator system (fig. 1.7 right) and later, a nose shape extension of the KAOS vacuum chamber to the scattering chamber was installed (fig. 1.7 left).

The hadron detector package is also located at the new platform. Due to the operational position of the spectrometer and its associated electronics, close to the target, makes mandatory the shielding of the system. A Monte-Carlo background study of the hall was performed in order to optimize the shielding needed [86]. The principal sources of background are electromagnetic and fast neutrons. For this a set of shield walls of lead alloy bricks (PbSb, $\rho=11.3 \text{ g/cm}^3$) covered by plates of borated polyethylene (BPE, $\rho=0.96 \text{ g/cm}^3$) in steel frame. The BPE walls help to shield against fast neutrons slowing down them with the high proportion of hydrogen in the compound and then captured, through (n, γ) reaction, in the boron. The resulting γ is absorbed in the lead bricks, originally used for radiation shielding from the target. Figures



Figure 1.7: Left. Photo of the target position in the three spectrometer hall oriented from beam direction to beam dump. At left can be seen the collimator system at the entrance window of KAOS. In the center is the standard target ladder with different kind of solid state targets and at right the quadropole entrance of Spectrometer C. Right. Photo of the extension of the vacuum chamber of KAOS to the scattering chamber.

1.6 and 2.56c shows different views of the shielding. The complete set of shield walls covers 20 m^2 .

Extra platforms were added later for locating the racks for the front-end electronics of hadron and electron arm.

1.2.2.2 Detector package of KAOS

As mentioned before, KAOS will be managed as a double arm spectrometer. For the electron arm, a new detector was developed which is the topic of this thesis. Following chapters will extend the development, description, test and characterization of the scintillator fiber detector. For the hadron side, the original MWPCs and Time of Flight (TOF) walls from the former configuration of KAOS at GSI were brought to Mainz. They were tested and upgraded in Mainz and incorporated to the data acquisition system of the A1 Collaboration. For a complementary detection and identification of the kaons at high momenta, a Cerenkov detector is being developed.

Multi Wire Proportional Chambers (MWPC) The tracking of particles through the hadron arm of KAOS is performed by two MWPCs [87]. The use of MWPC is an economical way of tracking charged particles covering large areas which do not require high spatial resolution [88]. The chambers were tested and set-up for their use with KAOS at the three spectrometer hall, *i.e.* the installation of the gas pipes from the detector lab to the chambers in the platform, the gas mixer, the power up of each chamber and their interconnection with the Data Acquisition (DAQ) system. The performance of the system was considerably improved achieving data rates over 1 kHz [89, 90].

The MWPC have an active area of $120 \times 35 \text{ cm}^2$ each and are operated with a gas mixture of argon with a mixture of CO_2 in a proportion between 10% and 19% of volume and C_4H_{10} in a proportion between 1% and 4% of volume [91]. Figure 1.11a shows a photography of one of the chambers in its measurement position in the platform.

The MWPC consist of a plane of wire anodes symmetrically sandwiched between two orthogonal wire planes of cathodes in X - and Y -direction and two meshes of woven fabrics of plastic coated with a nickel layer, forming two electrode planes, grid (G) and transfer (T) plane. These planes creates two spaces, pre-amplification and transfer gap. The wires of the anode plane are in diagonal respect to the cathodes grid, making an angle of 45° . The typical potential applied to this electrodes are: $U_G = -9.1 \text{ kV}$, $U_T = -2.0 \text{ kV}$, $U_A = +4.0 \text{ kV}$, with the cathodes connected to ground. The working principle is as follows: charged particles going through the active area produce primary electrons in the chamber gas, which is amplified in the high electric field of the pre-amplification gap for a gain of 10^2 . The avalanche then drifts to the transfer gap between T and the first cathode. Then the avalanche reaches the anode plane producing a second gas amplification of a factor 10^3 . Figure 1.8 schematizes the working principle. Particles from target cross the chamber with an angle of $50^\circ \pm 20^\circ$ respect to the normal.

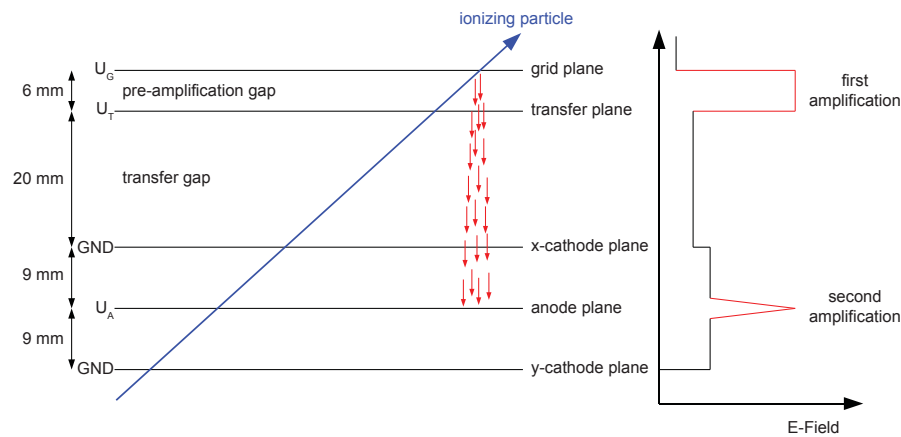


Figure 1.8: Schematic layout of the working principle of the MWPCs. Each chamber consists of a plane of wire anodes between two orthogonal wire cathodes, symmetrically spaced. Two conducting grids in front of the wire planes provide the amplification need for the drift of the electrons to the detection grid. This charge is amplified a second time at the anodes. At right is showed a typical distribution of the electric field. Figure from [92].

The pulse produced by the charged particle has a width $\sim 2 \mu\text{s}$. The signals are digitized by an ADC card addressed by a programmable transputer module placed in the frame of the chamber. The transputer network is connected to a multi-link card in a personal computer close to the detector and

managed by the slow control software of the A1 collaboration.

Scintillator walls Particle identification in the hadron side of KAOS is based principally on the time of flight and its specific energy loss measured by two scintillator walls [93, 94]. The walls are denominated F and G.

Wall F consisted in 30 scintillator paddles of $80 \times 3.7 \times 2 \text{ cm}^3$ size made of Pilot F material (equivalent to BICRON BC-408) and read out at both sides by fast PMTs HAMAMATSU R1828. The paddles are rotated 37° respect to the longitudinal axis in order to achieve a wider surface (37 mm) to the incident particles from target. The total length covered by the wall F is 189 cm. The wall was located close to the focal surface of the hadron arm and a momentum resolution of $\sim 4\%$ could be obtained with this segmentation.

Wall G, was used to discriminate valid tracks vs background events. It consists of 30 paddles of $47 \times 7.5 \times 2 \text{ cm}^3$ size made of BICRON BC-408 coupled, at both sides, through fishtail light guides to the PMTs HAMAMATSU R3478. Unlike wall F, the paddles present a flat geometry, and cover a length of 2.2 m. The signals from the walls are digitized with Fastbus Time to Digital Converter (TDC) and ADC modules. An intrinsic time of flight resolution of $\Delta t_{FWHM} \approx 420 \text{ ps}$ had been reached for pions crossing both walls.

The scintillator material has a 2.1 ns decay constant which make it suitable for time of flight measurements. The nominal attenuation length is of 3800 mm for BC-408 and of 3000 mm for Pilot F. Since the two walls had been in use since beginning of 1990's at the GSI a complete characterization was performed in Mainz [95]. Attenuation length for paddles from each wall were realized showing a decreasing of the attenuation length of a factor 2.3 for wall G paddles and a factor 6.6 for the wall F. As the time resolution depends of the light yield, the economic procedure was replacing the wall F keeping the wall G which shows less damage, putting it in wall F position (fig. 1.11b) and develop a new scintillator wall.

The new wall, labeled H (fig. 1.11c), was developed and tested by F. Schulz [96] based in a prototype tested during 2010 [97]. Wall H consists in 30 paddles of $58 \times 7 \times 2 \text{ cm}^3$ connected at both sides through fishtail lightguide to PMTs HAMAMATSU H1949. The wall covers a length of 2.13 m and is $\sim 1 \text{ m}$ far from the wall G. From the beam test realized in 2011, a time resolution of $\Delta t_{FWHM} \approx 300 \text{ ps}$ was measured.

Cerenkov detector The identification of kaons is the main task of KAOS for an efficient realization of experiments of electroproduction of strangeness in MAMI (sec. ??). For particle momenta of $p \sim 500 \text{ MeV}/c$, the separation between kaons and pions is possible by time of flight methods, so the scintillator walls are enough. But even well characterized scintillator walls, a separation of π/K becomes a hard issue with high momenta, since $\Delta t \sim 1/p^2$. So, for an

appropriate discrimination at momentum $p \geq 800 \text{ MeV}/c$, a Cerenkov detector is needed as a complement.

The develop and test of an Aerogel Cerenkov detector is being carried by L. Debenjak from the University of Ljubljana in Slovenia [98] in collaboration with the University of Tohoku in Japan.

The working principle of an aerogel Cerenkov counter is simple. Particles faster than speed of light in aerogel produce Cerenkov light that is collected by photon read out devices like PMTs. The condition to produce Cerenkov radiation is: $1/n < \beta_p < 1$, with n the refraction index of the medium, aerogel in this case, and β_p the speed of particle in c units. The minimum momentum for a particle of mass m to produce Cerenkov light is determined by the equation

$$p_{min} = \frac{mc}{\sqrt{n^2 - 1}} \quad (1.1)$$

Figure 1.9 shows the plot of equation 1.1 for kaons, $m = 493.68 \text{ MeV}$ and pions, $m = 139.57 \text{ MeV}$. The aerogel choose for the detector in Mainz has a refractive index of $n = 1.055$, so the threshold momentum for Cerenkov light production is $p_{K^+}^{th} \approx 1542 \text{ MeV}/c$ for kaons and $p_{\pi^+}^{th} \approx 436 \text{ MeV}/c$ for pions. Since kaons have a momentum of $1186 \text{ MeV}/c$ for a maximum MAMI beam energy of 1508 MeV , the refraction index for the choose aerogel makes this suitable for an optimal pion discrimination.

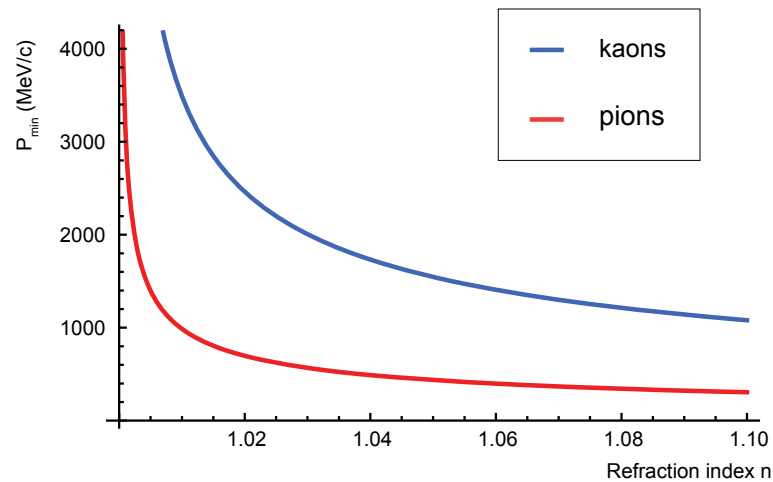


Figure 1.9: Plot of the minimum momentum for kaons and pions to produce Cerenkov light as a function of the refracting index of the medium. Figure from [98].

The Cerenkov counter consists in 6 cells which contains two layers of aerogel of 3 cm total thickness. The first layer of 2 cm thickness is formed of tiles of $5 \times 5 \text{ cm}^2$ from Budker Institute of Nuclear Physics, Novosibirsk, Russia and the second layer, of 1 cm thick, is formed by $12 \times 12 \text{ cm}^2$ tiles from Matsushita Electronics, Japan. Both, as mentioned before, with a refractive index

of $n = 1.055$. The tiles are fixed to the box by thin wires. Each cell is covered inside with high reflective coating and has a 90° mirror in front of the aerogel with its faces towards the PMTs, to increase the light collection efficiency. Each cell is inclined 55° respect to the plane formed by the aerogel tiles. Figure 1.10 shows an scheme of the diffusion box of the cell.

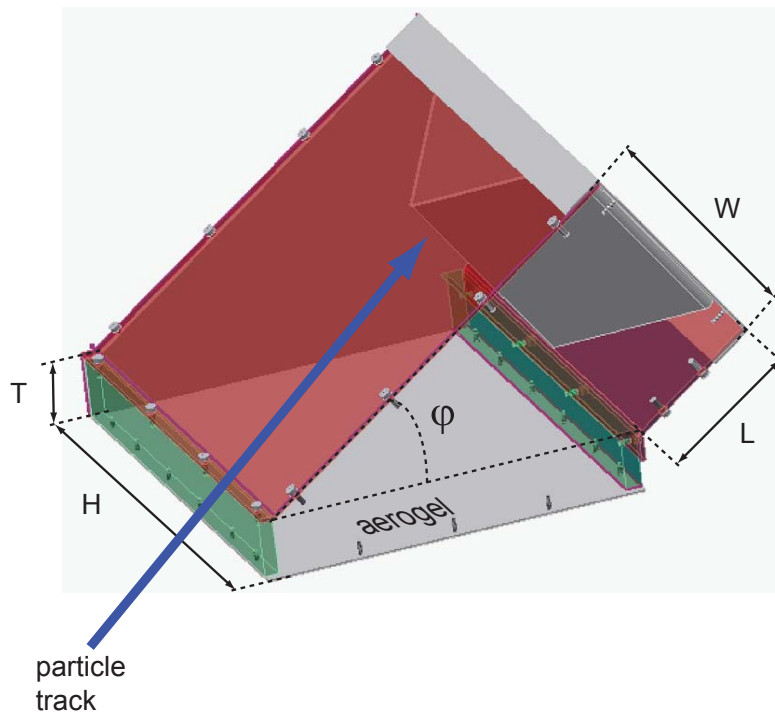
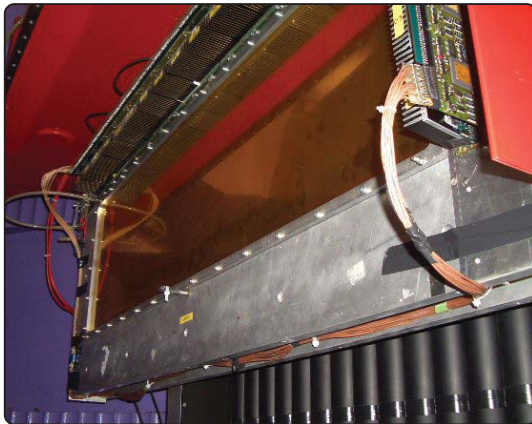
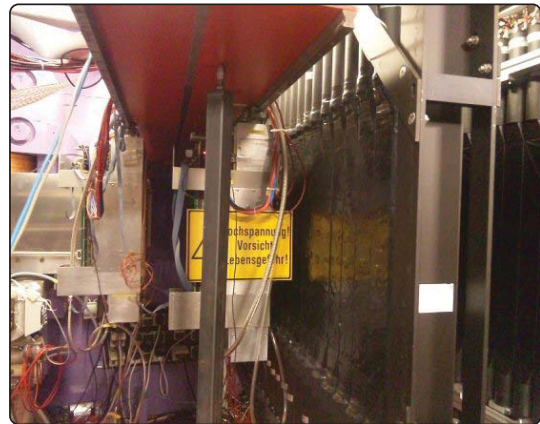


Figure 1.10: Drawing of the diffusion box of the Cerenkov detector. The dimensions are $T=3$ cm, $W=15$ cm, $H=35$ cm, $L=10$ cm and $\varphi=55^\circ$. Figure courtesy of L. Debenjak.

The read out of the produced light is made through PMTs although not yet has been decided which model to be used. The Cerenkov light yield is very low due to the absorption and scattering losses in the aerogel and different reflections into the diffusion box, so, photodetection devices should be choose in a way that help to maximize the photon yield. Some test were done with 5 inch HAMAMATSU R877-100 with super bialcali photocathode that provides a quantum detection efficiency up to 35%, making it a superb device for this detector but its high sensitive to high rate making the ADC pedestal very wide. Also, the 5 inch HAMAMATSU R1250, provided from the University of Tohoku, had been tested even its maximum quantum efficiency is just over 20%, but the 1 photoelectron peak is seen clearly making it easier to calibrate even at higher rates.



(a) Photography of one of the MWPC in its measurement position.



(b) Photography of the wall G showing that its position is as close as possible to the MWPC



(c) Photography of the wall H in the platform.



(d) Photography of the Cerenkov detector between wall G, at left and wall H at right.

Figure 1.11: Photographs of the hadron arm instrumentation of KAOS.

1.2.2.3 Modifications to the beam line

Electroproduction of strangeness requires very forward angles of detection respect to the electron beam direction (sec. ??). Due to the physical characteristics of KAOS, placing it in a detection angle close to 0° introduces many issues in the normal working of the three spectrometer hall in Mainz like a more complicated positioning system or a magnet behind KAOS to rectify the bending after the target to the beam dump, with the consequent large background radiation created in such configurations. An elegant and economic solution to achieve forward angles is a pre-target chicane.

The chicane comprises two dipole 30° sector magnets placed consecutively bending the electron beam in opposite direction. The incident angle to the target, and therefore the strength and position of the chicane magnets, depends of the strength field of KAOS in order to keep the beam into the beam dump. For a field of 1 T in KAOS, the chicane has to deflect the beam 13.5° in the first stage and approximately the double in the second stage for a resulting inclination of 16° . With this, KAOS bend the beam into the beam dump with an angle of 1.47° relative to the axis formed by the original beam direction [35].

The chicane had been commissioned and tested in 2010 and used in the decay pion experiment on a ^9Be target in 2011 [99]. In addition to the upstream chicane and because the beam deflection, a bremsstrahlung photon dump was installed. A scheme and a photography of the chicane in the three spectrometer hall is shown in fig. 1.12 and fig. 1.13.

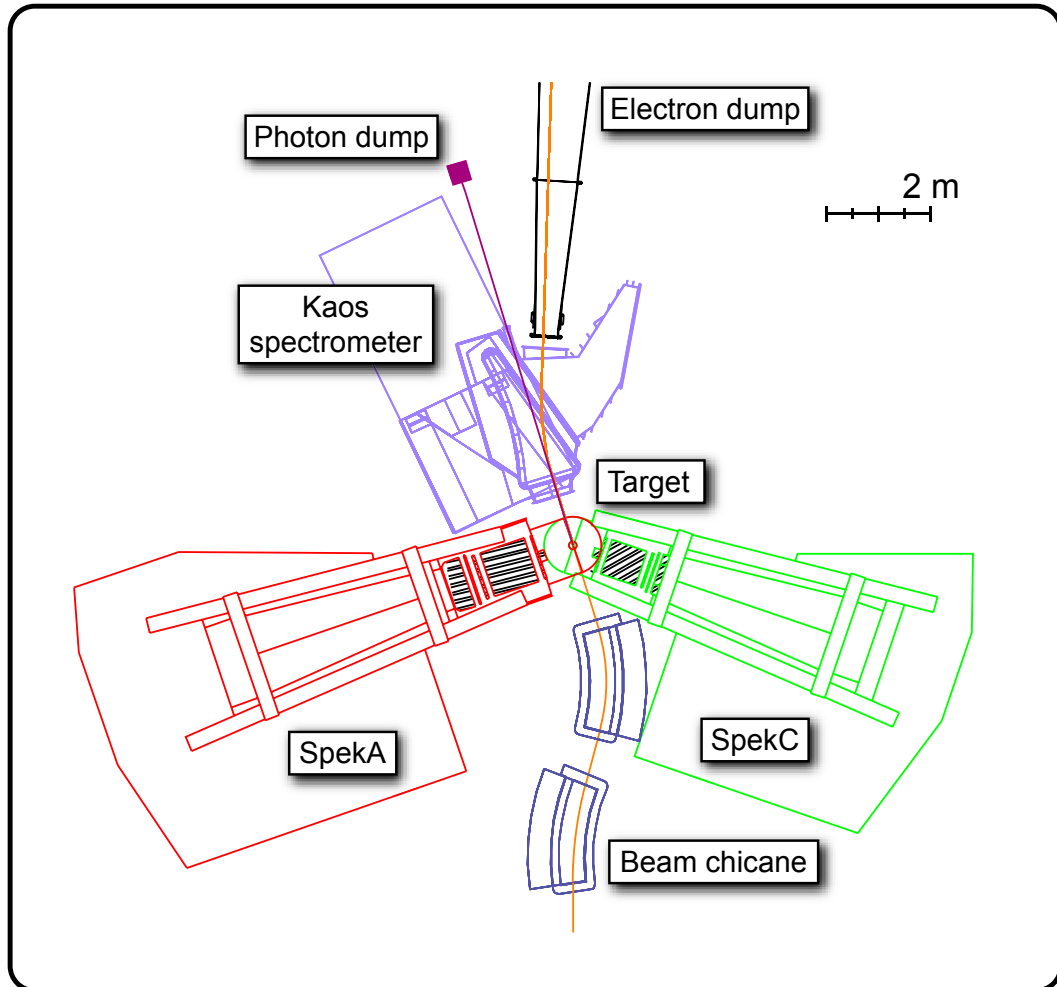


Figure 1.12: Drawing of the chicane and its position in the experimental hall. The beam, coming from the bottom, is deviated by the two magnets of the chicane in order to set the beam at 0° respect to KAOS entrance window. The strength of the fields of the two chicane magnets and KAOS are adjusted in such a way that the electron beam is deflected into the electron dump. Spectrometer B is not shown in the scheme.

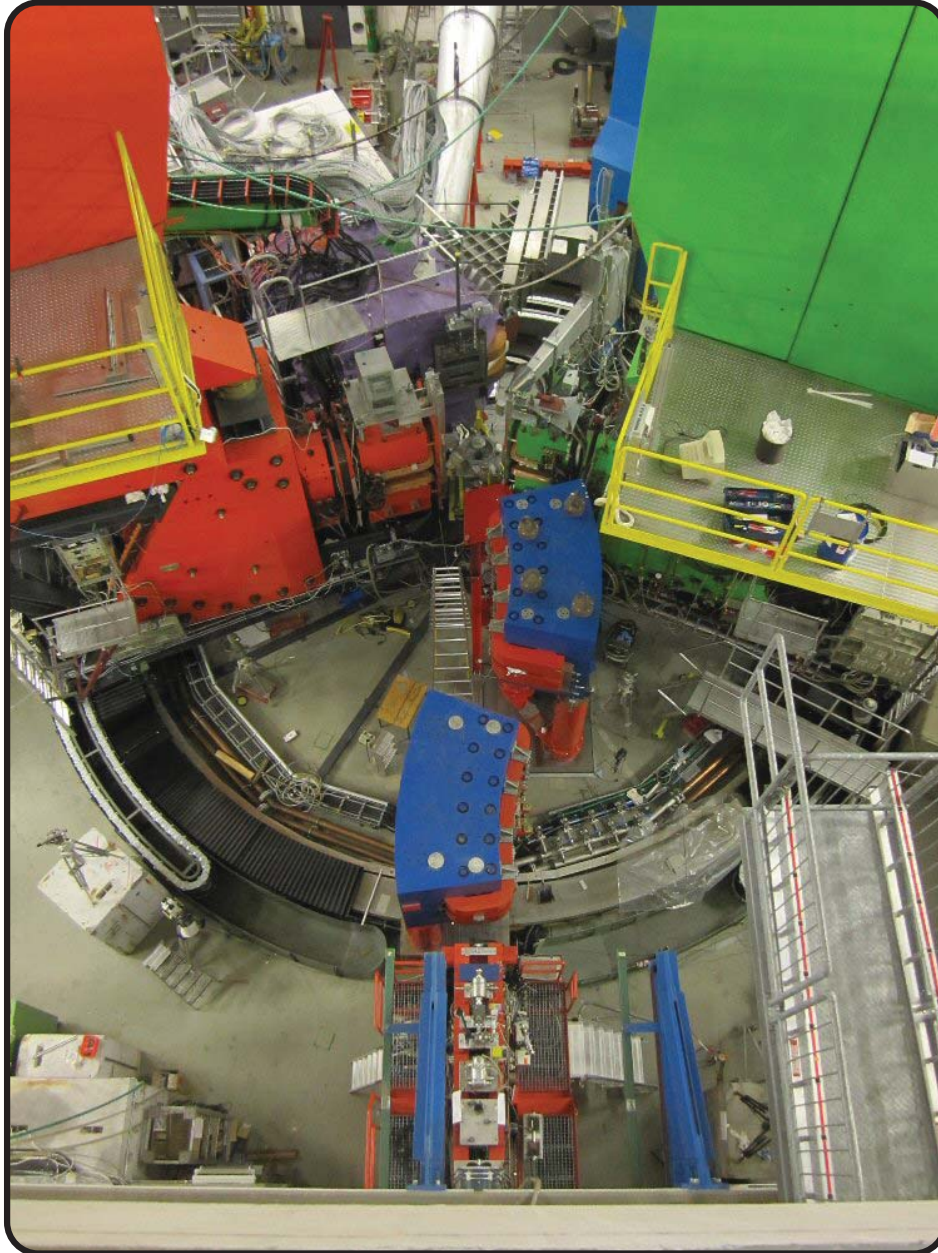


Figure 1.13: Photography of the chicane, the two blue magnets, installed in the three spectrometer hall, with Spectrometer A at left (red), and Spectrometer C at left (green). At top of the photography can be seen how the entrance of the beam dump is deviated respect to the original electron beam direction, attached to KAOS

The Scintillator Fiber Hodoscope

In any electron scattering experiment, the measurement of the scattered electron is mandatory. In electroproduction of hypernuclei, $(e, e'K)$, its momentum measurement becomes more critical, since the formation of the hypernuclei is principally determined by knowing the recoil momentum of the nucleus from the measurement of the momentum of the formed kaon and the scattered electron. Measuring the momentum could be done with tracking detectors. Due to the conditions for optimal hypernuclei production, this detector should be located close to 0° with respect to the beam direction, it must have a high count rate capability and a high granularity in order to obtain the best momentum resolution.

A 4608 channels plastic scintillator fiber arrange with multianode photomultipliers fulfill this requirements. Two planes, each covering ~ 2 m, made of 144 modules of 32 read-out channels each comprising 128 fibres/module, were built, assembled, tested and characterized. The use of scintillator fibers, in a close packed array, allow a high granularity giving a high spatial resolution and therefore obtain high momentum resolution. The long detector planes warrants that electron side of KAOS acceptance is totally covered.

Calibration of the fiber hodoscope presents a challenge due to the high number of channels, making such process manually unpracticable in a reasonable time (~ 20 days of continuous). Fully automatized set-up of the whole calibraton process had been implemented reducing the process time to 4 – 5 days of continuous running.

State-of-the-art signal processor modules and DAQ electronics complements the requirements for a fast and reliable detector [100].

2.1 Scintillator Fibers

The use of scintillator fibers as detectors had been widely used since end of the 80's. They combine the efficiency and speed of a scintillator de-

tor with the flexibility and hermiticity of fiber technology. They can be arranged in different configurations to accommodate the required geometry. Initially, fibers were based in glass fiber materials doped with Cerium (Ce^{3+} oxide), but this introduces some difficulties such as low quantum efficiency, a slow component to the scintillation emission and a significant optical self-absorption. Organic plastic scintillators solve these difficulties. Typical organic plastic scintillators are formed by a base of a polymeric material as polystyrene or polyviniltoluene, doped with an organic fluorescent dye, covered with one or two transparent cladding materials with smaller refraction index. The core polymer absorbs energy from ionizing radiation but the relaxation times are slow and they are not good light emitters. The dopation allows a rapid transfer of energy from the polymer to the dye, keeping the excitation, and relaxing the polymer molecule quickly to the ground state ($< 1 ns$). The dye is chosen to have high quantum efficiency, rapid fluorescence decay (in the order of few nanoseconds) in a specifically wavelength range, where the light emitted is practically transparent to the polymer and the dye, and matches more efficiently the photosensors existing nowadays. Concentration of the dye respect to the polymer base is around 1% by weight, even this could vary depending on the needs of the experiments. An increase of the concentration increases the light yield but reduces the attenuation length of the fiber [101, 102].

These dyes are usually aromatic hydrocarbon compounds. The scintillation light in these material arises from the transition made by the free valence electrons of the molecules, which are known as the π -molecular orbital. In an energy level diagram we can distinguish spin singlet and spin triplet orbital (Fig.2.1). The ground state is a singlet state, which we denote as S_0 , above this level we have the excited singlet states (S_1, S_2, \dots) and the lowest triplet state T_0 and its excited levels. Also there is a fine structure which corresponds to excited vibrational modes of the molecule. But whereas the separation between electron levels is in the order of eV, the vibrational levels are in the order of a few tenths of eV.

Penetrating radiation excites the electron and vibrational levels. The singlet excitations decay immediately to the S_1 state without the emission of radiation (internal degradation). From S_1 , there is a high probability of making a radiative decay to one of the vibrational states of S_0 within a few nanoseconds time. This is the normal process of fluorescence. The fact that S_1 decay to excited vibrational states of S_0 , with emission of radiation energy less then that required for the transition $S_0 \rightarrow S_1$, explains the transparency of the scintillators to their own radiation.

A similar process occurs for the triplet excited states, but the decay T_0 to S_0 are highly suppressed by multipole selection rules. Interacting with another excited T_0 molecule, the process, $T_0 + T_0 \rightarrow S_1 + S_0 + \textit{phonons}$ could happen and the decay from S_1 is produced in the same way as explained before. The light from this process is the slow component of scintillator light. The contri-

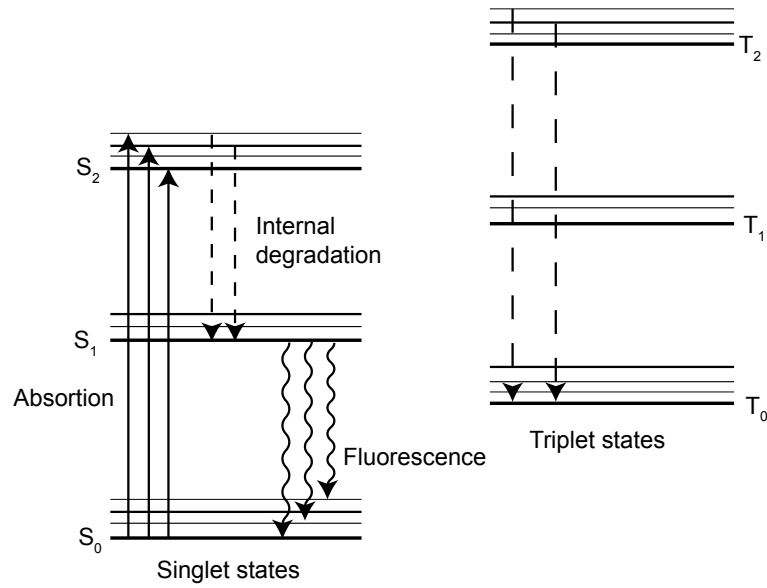


Figure 2.1: Energy diagram of the process of scintillation with the singlet and triplet states separated for clarity (Source [103])

bution of this component is only significant in certain organic materials [103].

The light produced in the fiber has a low probability of being detected due to the small detection area/total surface area. The light detected depends almost entirely on the total reflected light in the fiber. But also the absorption depending on the number of reflections and path length reduces the probability of the photon to be detected. Thus, light yield depends on the position where the light is produced along the fiber, but it also depends if it is produced off axis [102].

For scintillation at a point on the axis of the fiber, the generated light travels radially in the plane perpendicular to the fiber axis, so the angle of incidence at the reflection surface is determined by just the polar angle θ , *i.e.* the emission angle with respect to the axis.

The fraction of a solid angle of light that is totally reflected is calculated using Snell's law, $n_i \sin \phi_i = n_r \sin \phi_r$, in the case of total reflection, $\sin \phi_r = 1$. With the use of simple trigonometry, in our case, $\sin \phi_i = \cos \theta$, and thus

$$\sin \phi_c = \frac{n_2}{n_1} = \cos \theta_c \quad (2.1)$$

where ϕ_c is the critical angle of incidence and θ_c is the corresponding emission (polar) critical angle (fig 2.2 (Top)).

The fraction of the solid angle is calculated by

$$F = \frac{\Omega}{4\pi} = \frac{1}{4\pi} \int_{\theta_0=0}^{\theta_c} d\Omega = \frac{1}{4\pi} \int_0^{\theta_c} 2\pi \sin \theta d\theta = \frac{1}{2}(1 - \cos \theta_c) \quad (2.2)$$

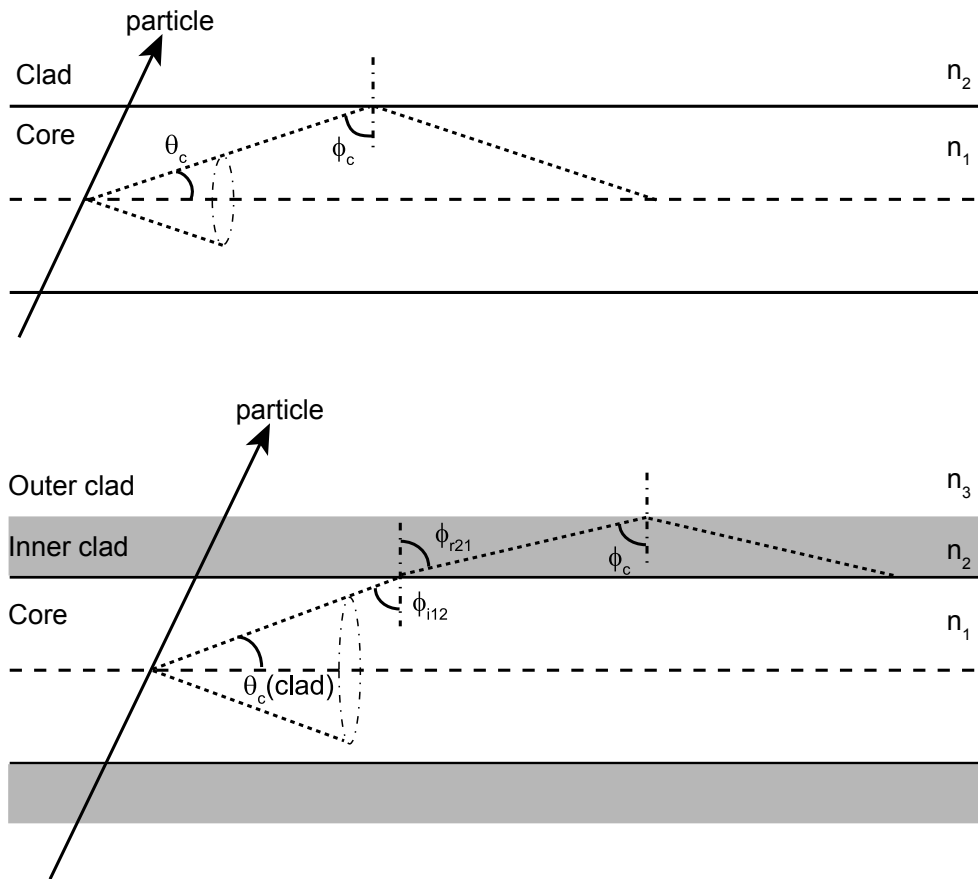


Figure 2.2: Scheme of the total reflection by light emitted on axis. Top. Single cladding, θ_c is the emission (polar) critical angle and ϕ_c is the critical angle of incidence. Bottom. Multicladding, θ_c is the emission (polar) critical angle, ϕ_i is the incidence angle at core-inner clad interface, ϕ_r is the corresponding refracted angle and ϕ_c is the critical angle of incidence.

Replacing with 2.1, the fraction of the solid angle subtended by the light emitted on the axis and which is confined in the fiber is¹:

$$F_{core} = \frac{1}{2} \left(1 - \frac{n_2}{n_1} \right) \quad (2.3)$$

A significant advance in fiber waveguide manufacture has been the development of multicladding scintillating fibers by KURARAY CORP. [101]. In this case, surrounding the polymer core are two claddings: an inner clad of Polymethylmethacrylate (PMMA) and an outer clad of fluoro-acrylic polymer, with decreasing refractive index from core to outer clad. The PMMA inner clad also serves as a mechanical interface between the mechanically incompatible core and the outer clad.

¹As it seems from the integration limits, this is the light trapped in one direction of the fiber

The outer cladding opens the solid angle of the collected light. The extra fraction of light collected is calculated considering only the light which is not confined between the core and the inner clad, *i.e.* angles of emission greater than the critical angle. The only solid angle fraction to calculate is between the emission critical angle for the core-inner interface, $\theta_c(\text{core})$, as calculated before, and the emission critical angle for the inner-outer interface, $\theta_c(\text{clad})$. (Fig.2.2)

$$F_{\text{clad}} = \frac{1}{4\pi} \int_{\theta_c(\text{core})}^{\theta_c(\text{clad})} d\Omega = \frac{1}{2} (\cos \theta_c(\text{core}) - \cos \theta_c(\text{clad})) \quad (2.4)$$

From fig. 2.2:

$$\sin \phi_c = \frac{n_3}{n_2} = \sin \phi_{r21} \quad (2.5)$$

where ϕ_{r21} is the refracted core-inner clad angle. Using Snell's law:

$$\sin \phi_{i12} = \frac{n_2}{n_1} \sin \phi_{r21} = \frac{n_3}{n_1} \quad (2.6)$$

again, from simple trigonometry:

$$\sin \phi_{i12} = \frac{n_3}{n_1} = \cos \theta_c(\text{clad}) \quad (2.7)$$

and replacing in 2.4:

$$F_{\text{clad}} = \frac{1}{2} \left(\frac{n_2 - n_3}{n_1} \right) \quad (2.8)$$

The total fraction of light collected in multicladding fibers is:

$$F_{\text{core}} + F_{\text{clad}} = \frac{1}{2} \left[\left(\frac{n_1 - n_2}{n_1} \right) + \left(\frac{n_2 - n_3}{n_1} \right) \right] = \frac{1}{2} \left(\frac{n_1 - n_3}{n_1} \right) \quad (2.9)$$

In general, the light collected by the outer clad-air interface is not considered because due to surface imperfections, it is expected to have a short attenuation length, neither is considered the scintillation light emitted away from the axis of the fiber because these rays "spiral" along the fiber with a large number of reflections, having a longer path length and thus a shorter attenuation length [104].

2.1.1 The Kuraray SCSF-78M fiber

The fiber chosen for the electron detector for the KAOS spectrometer in Mainz is the Kuraray SCSF-78M multicladding fibers from KURARAY CORP. This fiber has a 0.83 mm diameter and consists of a polystyrene core of nearly 0.73 mm and two concentric claddings. A PMMA inner clad of 0.25 mm thickness and a fluorinated polymer outer clad of 0.25 mm thickness.. The scintillating light has the emission peak at 450 nm as seen in the emission spectra

shown in fig.2.3. This plot shows the different emission spectra when the fiber is exposed to a UV source of 350 nm wavelength, with a spot size of 5 mm and different position of the source along the fiber (from top to bottom, at 10, 30, 100, 300 cm). The different curves show that blue light (450 – 475 nm) is attenuated stronger. Attenuation length is a function of the wavelength.

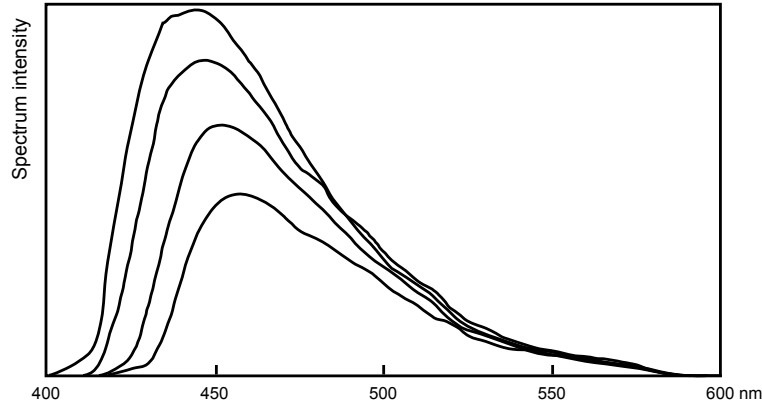


Figure 2.3: Emission spectrum of SCSF-78M fiber in arbitrary units. This plot shows the different emission spectra when the fiber is exposed to a UV source (350 nm wavelength), with a spot size of 5 mm and different position of the source along the fiber (from top to bottom, at 10, 30, 100, 300 cm) (source: KURARAY CORP.)

A resume of the SCSF-78M characteristics are shown in table 2.1. The diameter of the fiber, the fast decay, 2.8 ns, and long attenuation length, more than 4 m, fulfill the requirements for an effective detection of the scattered electron under the conditions of the KAOs spectrometer.

The fraction of solid angle for this kind of fibers (section 2.1) from eq. 2.9 is $F_{mc} = 5,3\%$. It means that a multicladding fiber gives 70% more light than a single cladding ($F_{core} = 3,1\%$). But it is known that in practice, the increase is only 50% or less. Nevertheless, more than 90% of the produced light is lost. As mentioned before, this is the total light trapped in one direction of the fiber, considering an homogeneous distribution of the light produced, we lose the same quantity in the other side if no photosensor is placed. Some of this light can be recovered with some reflector material at the end.

2.2 Readout electronics

Scintillation detection depends in great part on the electronics used to detect the light produced. It could be semiconductor devices such as CCD [105], silicon photomultipliers [106, 107] or the most commonly used to this purpose, photomultiplier tubes (PMT). Devices as visible-light photon counters (VLPC), which have a good behavior in photon detection, have the in-

Table 2.1: SCSF-78M characteristics. (Source: KURARAY CORP.)

General	
Color	blue
Emission Peak (nm)	450
Decay time (ns)	2.8
Att. Length (m)	> 4.0
Diameter (mm)	0.83
Core	
Material	Polystyrene (PS)
Refractive Index	1.59
Density (g/cm ²)	1.05
Inner Clad	
Material	Polymethylmethacrylate (PMMA)
Thickness (μm)	25
Refractive Index	1.49
Density (g/cm ²)	1.19
Outer Clad	
Material	Fluorinated polymer (FP)
Thickness (μm)	25
Refractive Index	1.42
Density (g/cm ²)	1.43

convenient of being operated in a cold environment (6-14 K), or the use of avalanche photodiodes, that even if they are cheaper, are not optimal for fast single-photon applications [101].

PMT are devices that convert the light into a measurable electric current by photoelectric effect. A PMT can be described as a vacuum tube consisting of an input window, a photocathode, focusing electrodes, an electron multiplier and an anode, sealed into an evacuated glass tube [108]. Among the great quantity of different phototubes in the market, a family of compact multi-anode PTM (MaPMT) has been developed in different layouts (linear, square) and different number of anodes (fig. 2.4). This kind of PMT allows a suitable compact detector for the electroproduction of hypernucleus experiments in Mainz.

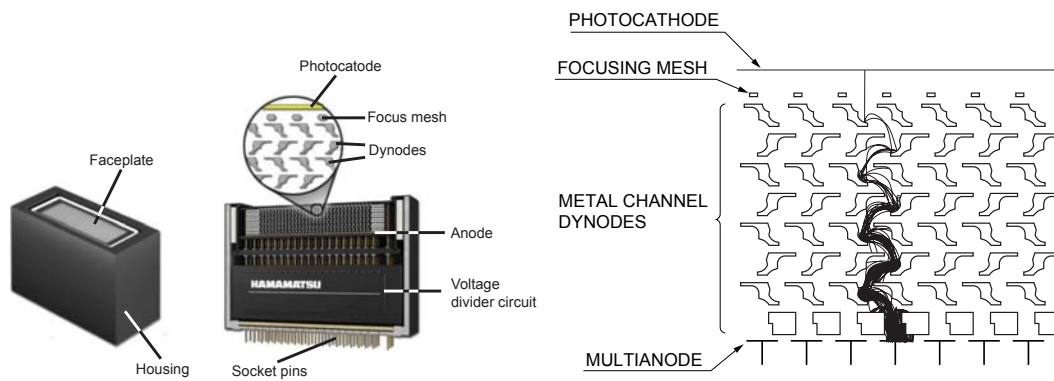


Figure 2.4: Left. Linear multianode photomultiplier tube showing the most relevant parts. Right. Electrode structure and electron trajectories of the MaPMT. (Source: HAMAMATSU PHOTONICS K.K.)

2.2.1 The Hamamatsu H7259K photomultiplier

The H7259K from HAMAMATSU² of 32 channels in linear array (fig. 2.5) is the chosen PMT for the fiber detector. It is fundamentally the H7260K without the voltage divider provided by HAMAMATSU. The H7259K is the MaPMT which gives the maximum value of the convolution (eq. 2.10) of the emission spectra of the fiber SCSF-78M, $P(\lambda)$ (fig. 2.3) with the quantum efficiency of the PMT, $Q(\lambda)$, (fig. 2.6), but since there is no way to make it in an analytical way, a discreteness of the graphs should be employed:

$$\int_0^{\infty} P(\lambda)Q(\lambda)d\lambda \xrightarrow{\text{discrete}} \sum_{\lambda_i} P(\lambda_i)Q(\lambda_i)\Delta\lambda_i \quad (2.10)$$

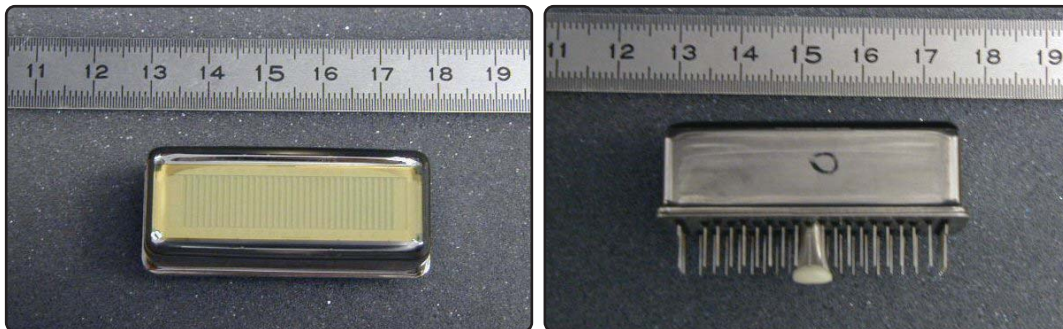


Figure 2.5: Left. Up view of H7259K. The 32 strips of the photocathode are visible through the borosilicate window. Right. Side view of H7259K showing the pins of signal, bias and ground. The ruler indicates centimeters.

The H7259K has a borosilicate glass window of 1.5 mm thickness and the photocathode is made of bialkali material. The 32 anodes, of $0.8 \times 1 \text{ mm}^2$ size, are arranged linearly, separated by 0.2 mm. The multiplication process

²HAMAMATSU PHOTONICS K.K.

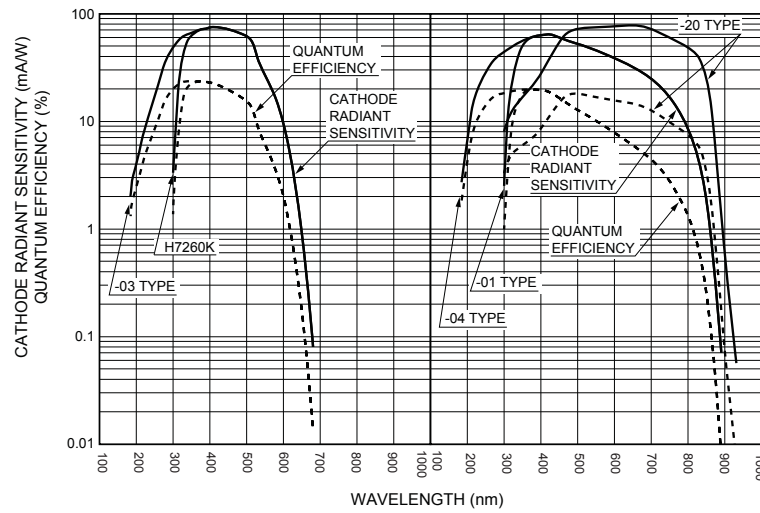


Figure 2.6: Quantum efficiency and cathode radiant sensitivity of linear MaPMT of the H7260 family with different photocatode and window material. (Source: HAMAMATSU PHOTONICS K.K.)

is provided of 10 stages of metal channel dynodes. Each pixel can be measured independently by its respective anode. The PMT operates at negative high-voltages with a gain of near 2×10^6 when it is biased at -800 V. The gain variation between different pixels could be up to 30% (fig. 2.7), with lower gains at the edges of the phototube on average. A resume of the characteristics of the H7259K is shown in Table 2.2.

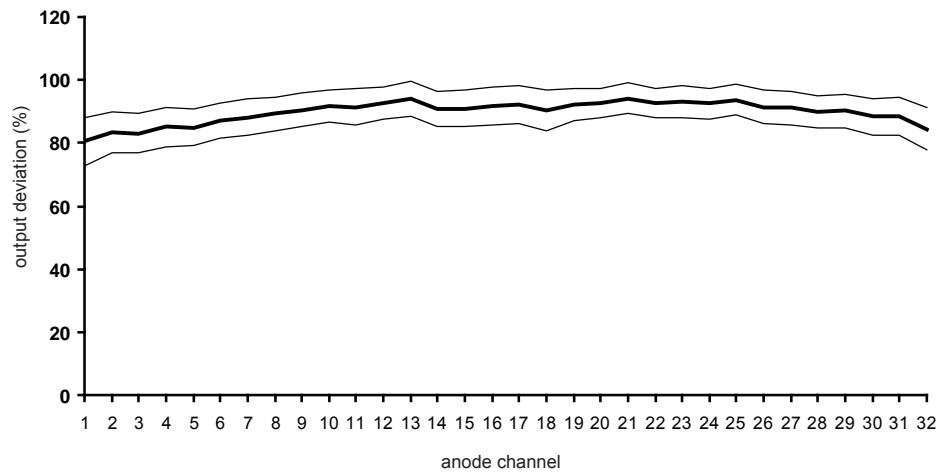


Figure 2.7: Mean value of the output deviation of the anode signal from the phototubes purchased in Mainz. The thicker lines show the standard deviation from the mean value. It shows that in average, the edges of the phototubes have lower gain that the central ones.

Table 2.2: H7260K characteristics. Typical values are from Hamamatsu catalog, mean values is the mean value of the H7259K values from individual data sheet from the phototubes purchased. (Source: HAMMAMATSU PHOTONICS K.K.)

General	
Spectral response (nm)	300 to 650
Maximum response (nm)	420
Window material	Borosilicate Glass
Maximum Supply Voltage (Vdc)	-900
Cross Talk	3%
Uniformity Between each Anode	1:1.5 (typical)/1:1.17 (mean)
Photocatode	
Material	Bialkali
Effective area per channel (mm)	0.8×7
Channel Pitch (mm ²)	1
Luminous ($\mu\text{A}/\text{lm}$)	70 (typical)/80.13 (mean)
Blue sensitivity Index	8.5 (typical)/7.61 (mean)
Anode	
Luminous (A/lm)	140 (typical)/362.03 (mean)
Gain (at -800 V)	$2 \cdot 10^6$ (typical)/ $4.42 \cdot 10^6$ (mean)
Dark Current (nA)	0.2 (typical)/7.96 (mean)
Anode Pulse Rise Time (ns)	0.6
Dynode	
Structure	Metal channel dynode
Number of stages	10

2.2.1.1 The HVSys voltage multiplier cell.

As mentioned before, the H7259K is essentially the H7260K offered by Hamamatsu but without the voltage divider to power it and the interface to obtain the signal. Instead, a new base has been developed and manufactured by HVSys, Dubna[109]. Unlike the standard way to power the PMT (high voltages of the order ~ 1000 V), the base is powered with 140 V dc. The high voltages necessary for the operation of the PMT are generated in the base by a Cockroft-Walton circuit³ (C-W). The C-W output is regulated with a 10-bit Digital Analog Converter (DAC), placed in the base too, and controlled via I²C bus which allows to control up to 127 MaPMT per line. All the bases are served

³A Cockroft-Walton voltage multiplier circuit is a electric circuit formed of capacitors and diodes which generates high DC voltage from low voltage input

by a system module through a 10 pin flat cable and then through a front-end board, where three consecutive bases are placed (see 2.2.2). The 10 pin flat cable, alongside the I²C signal, provides +5 V supply for the cell electronics and +(100-200) V for the C-W driver. It suppresses the use of expensive connectors (as SHV connectors) and stiff cables, helping with the size reduction of the detector. The cell has a maximum anode current less than 2 mA and a voltage stability in the order of 0.05%.

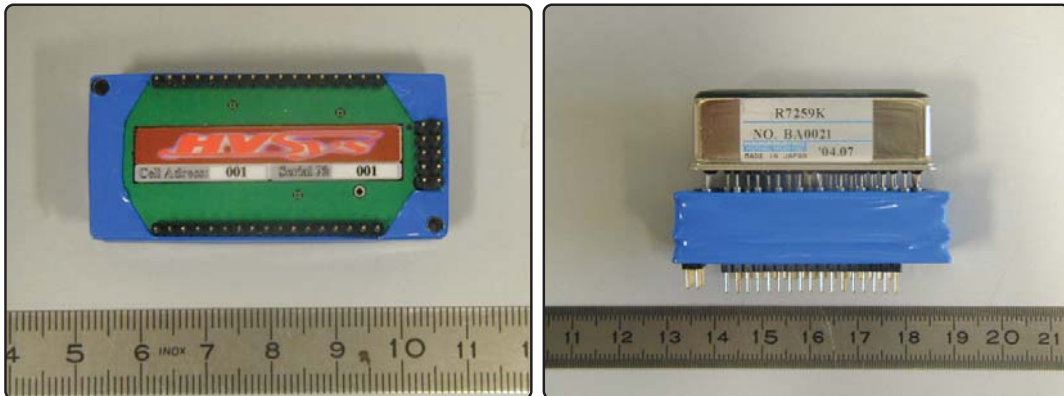


Figure 2.8: Left. Bottom view of HV Sys voltage multiplier cell for the H7259K, the 32 pins for the output signal are located up and down of the picture and the 10 pins connections for signal control and power supply at a side. Right. Side view of HV Sys voltage multiplier cell with the H7259K. The ruler indicates centimeters.

The system module HV Sys512 is controlled remotely by RS-232 or CAN bus and can supply to 4 branches allowing 508 bases to be handled. It is designed as a standard 6U unit (40 mm width) (fig. 2.9).

2.2.2 Front-end board

The design concept of the hodoscope makes the power supply and the readout of the signals, from several PMT with a compact arrangement, a technical challenge. The front-end board, designed in the electronic workshop of the Institut für Kernphysik of Mainz, solves the power up, control and readout of the signals from the HV Sys bases in an efficient way [100]. The layout of the board follows the shape of the fiber bundle (sec. 2.4.1.1). In this way, three bases from consecutive fiber bundles can be directly attached to the board. The signal lines from the MaPMT to the output socket are arranged in such way that the time jitter at the output is minimized. The output sockets seats eight RJ-45 connectors with 4 analog signal each, making a total of 96 channels per board.

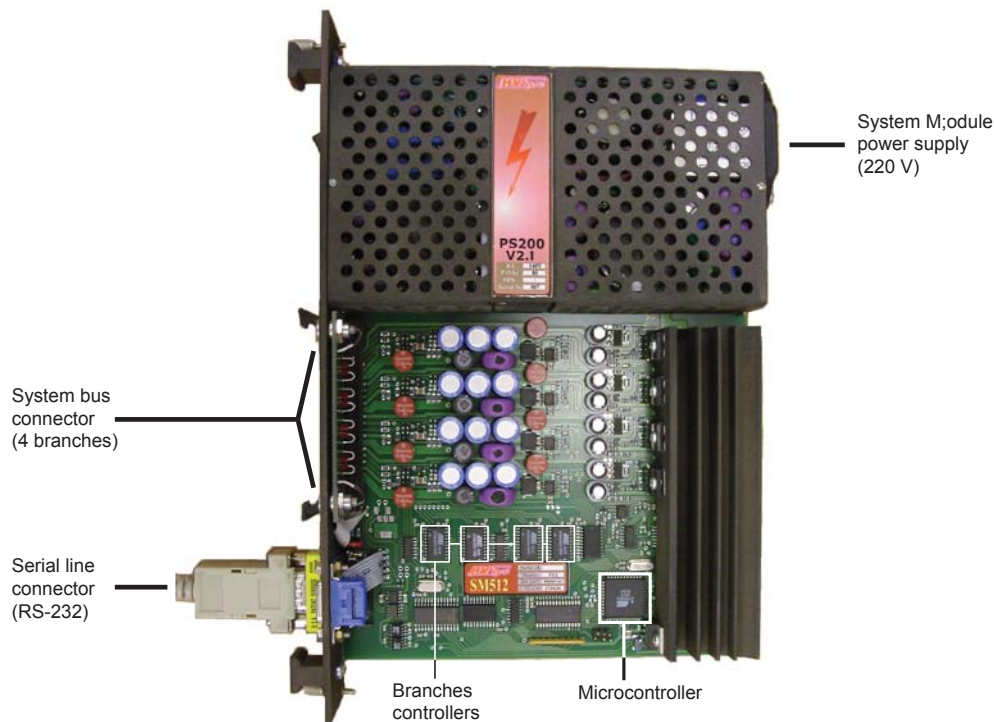


Figure 2.9: Side view of the HVSys512 module. The system bus connector is unique for the 4 branches, although each branch is independent of each other. The power supply of the module is a normal 220 V input.

2.3 Data Acquisition

The accuracy in the measurements depends greatly in the signal processing and analysis. For the KAOS fiber hodoscope, the signals from the MaPMT are processed in a double threshold discriminator, developed in the electronic workshop of the IKPH, which distributes its output to a VME time digital converter, developed for the Common Muon Proton Apparatus for Structure and Spectroscopy (COMPASS) experiment at the European Organization for Nuclear Research (CERN), and a VME logic module for trigger purposes called VUPROM, developed at GSI.

2.3.1 Double threshold discriminator

Since the accuracy in timing is fundamental in the experiments to be done at MAMI, the discriminators should provide an output with low time-walk. Due to the wide range of signal amplitudes, the use of the leading edge makes them inadequate since they are sensible to signal amplitude introducing notable time-walk. Constant fraction discriminators have good timing properties, but they are expensive. The use of the Double Threshold Discriminator (DTD) is an intermediate solution. Its principle is explained next. The module (fig.

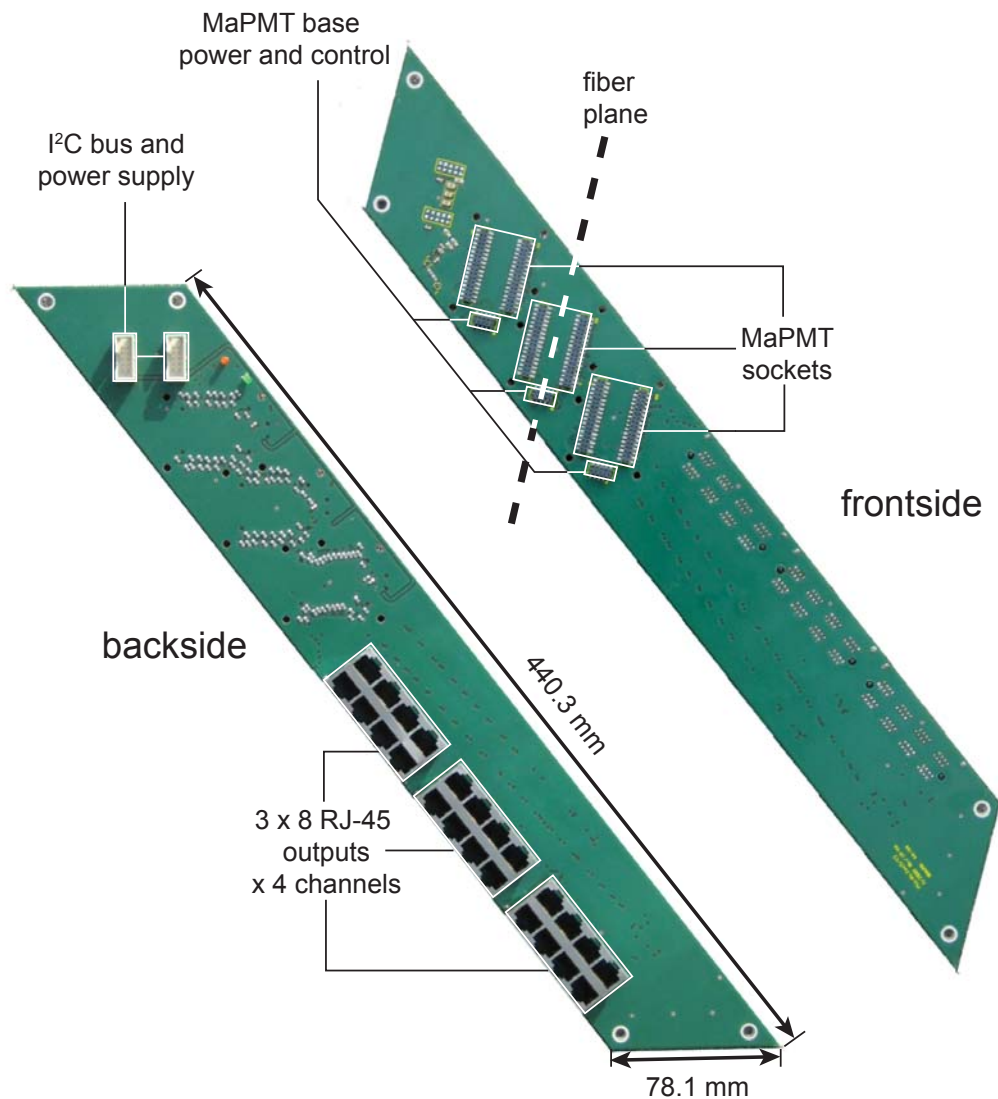


Figure 2.10: Photograph of front-end board used in the fiber detector hodoscope for the KAOS spectrometer showing the path where the fiber plane is located. (Frontside) The sockets for the power, control and readout for three MaPMT are shown. (Backside) At top are the connectors for the 10 pin flat cable of the I²C bus and power supply, one works as input for the board and the other connects to the next board. At bottom are the output signal sockets. Each socket comprises eight RJ-45 connectors, each cable handle four MaPMT channels. Each board handles 96 channels. The board width was determined from the width of three consecutive fiber bundles.

2.11), developed in the electronic workshop of the IKPH, is able to handle the signals from a single MaPMT, *i.e.* 32 channels per board. The signals are transported from the front-end board over 15 m through Cat-7 patch cables, that are well shielded and show small losses, to the discriminator board. Every 4 channels are processed by a DTD chip, called GSI-chip3 [110]. The output signal is made of a standard Low Voltage Differential Signal (LVDS) type of ~ 12 ns long. The board provides two outputs of the same kind, on the front side with a 68-pin Robinson-Nugent connector to the readout modules, and on the backside with a Very High Density Cable Interconnect (VHDCI) connector for trigger purposes. Also, four analogue coaxial 50Ω connectors are available, two multiplexed for debugging and trigger purposes and one OR and one $\overline{\text{OR}}$ dedicated outputs. For a complete analysis of the behavior of the fiber bundle, a 32-channel analogue output board can be attached to the DTD board. The board was designed to fit a VME 6U crate, which provides power supply to the boards also, but instead of a standard VME CPU, a controller board is used which is addressed from a PC via parallel port. The controller (fig. 2.12), designed also in Mainz, communicates with the DTD boards through the VME bus across bridges implemented in Complex Programmable Logic Devices (CPLD) by LATTICE⁴.

2.3.1.1 Double Threshold Discriminator operation principle

When an input signal exceeds the requested thresholds at the discriminator, two voltage ramps with different slopes are triggered by comparators at the moment that the signal crosses each threshold. Where the difference between both ramps vanishes, a third comparator produces the output signal (fig. 2.13). This allows an output signal with a constant delay if a constant slope of the input signal is considered. Analytically, from the relation of the voltage difference at the output comparator

$$\Delta V(t) = (V_1 + (t - t_1)a_1) - (V_2 + (t - t_2)a_2) \quad (2.11)$$

where, t_1 and t_2 are the times when the input signal crosses the lower level threshold V_{thr}^L , and upper level threshold V_{thr}^U , respectively and V_1 and V_2 the initial values of the voltage ramps. With this, the output signal time of the DTD t_0 , occurs when $\Delta V(t_0) = 0$, thus from eq. 2.11

$$t_0 = \frac{\Delta V_0 + t_1 a_1 - t_2 a_2}{a_1 - a_2} \quad (2.12)$$

If as said before, if the rise time of the input signal is parameterized by a constant slope a , the output time t_0 is independent from the signal if the ratio V_{thr}^L/V_{thr}^U , which is set externally, is equal to the internal parameter a_2/a_1 . This

⁴Lattice Semiconductor Corporation

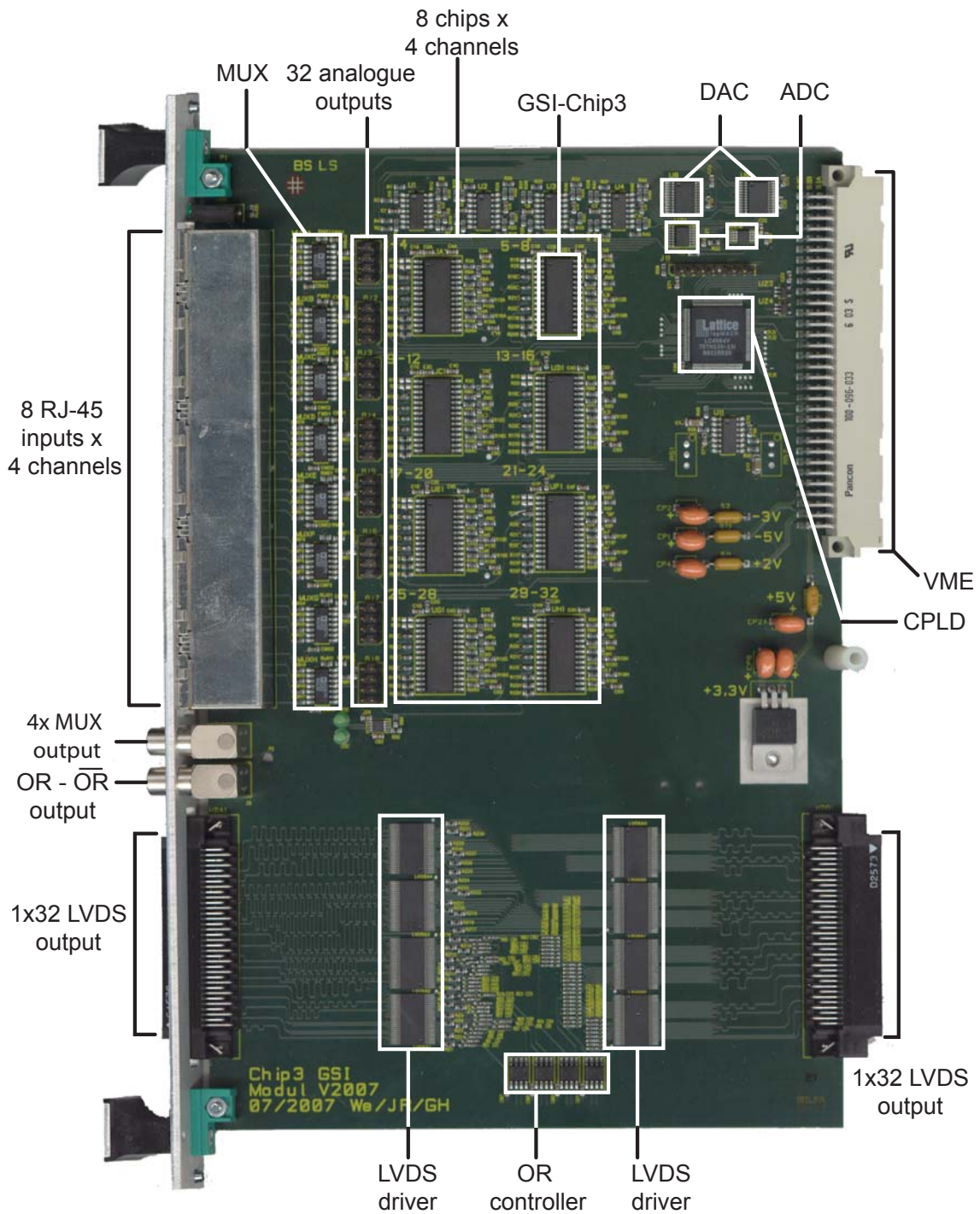


Figure 2.11: Photograph of the double-threshold discriminator board designed in the IKPH for the fiber detector. The two high-density connectors and the drivers for the differential LVDS outputs are visible in the lower part, the right one is replaced by a VHDCI connector. The 8 RJ-45 connectors for analogue inputs are located at the top left and the four coaxial 50Ω outputs for multiplexed analogue signals as well as OR and OR trigger signals at centre left. The module hosts 8 GSI-CHIP3 DTD and is controlled from a CPLD device by LATTICE.

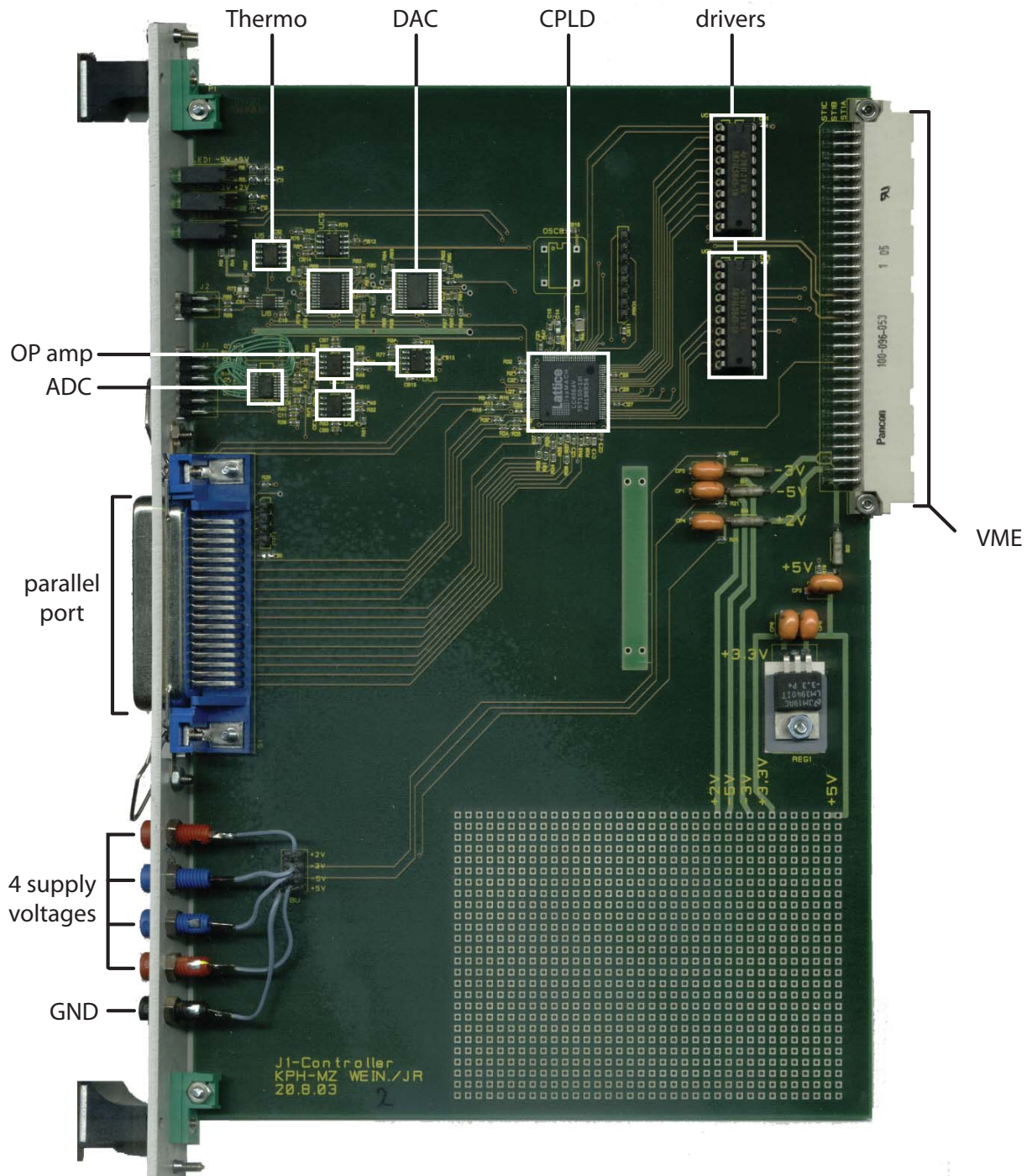


Figure 2.12: Photograph of the controller board for double-threshold discriminators designed in the IKPH for the fiber detector. The CPLD device by LATTICE addresses up to 20 DTD boards in a crate via VME bus and connects to a PC via parallel port. The threshold voltages are generated from common voltage references; temperature and reference voltages are read back for diagnostics.

condition holds because

$$t_1 a_1 - t_2 a_2 = V_{thr}^L a_1 / a - V_{thr}^U a_2 / a \equiv 0 \quad (2.13)$$

which leads the eq. 2.12 to $t_0 = \Delta V_0 / (a_1 - a_2)$, which is independent of the times when the ramps are triggered. In practice, comparators are not ideal, and a time-walk of 15 ps peak-to-peak for an amplitude range between 70-250 mV was observed at a rise time of the input signal of 600 ps [110].

In the DTD board, the ratio $a_2/a_1 = 2$ is fixed and the threshold ratio is set externally. The voltage thresholds are set by two 8-channel 8-bit DAC relative to one tenth of a common voltage reference and are read back by a 12-bit ADC. The voltage references are set on the controller board by two 8-channel 8 bit-ADC with 87 mV full scale per channel for the lower threshold and 157 mV full scale for the upper threshold. Values of the ratio a_2/a_1 above 2 can be used to compensate to some extent the comparator skewing [35].

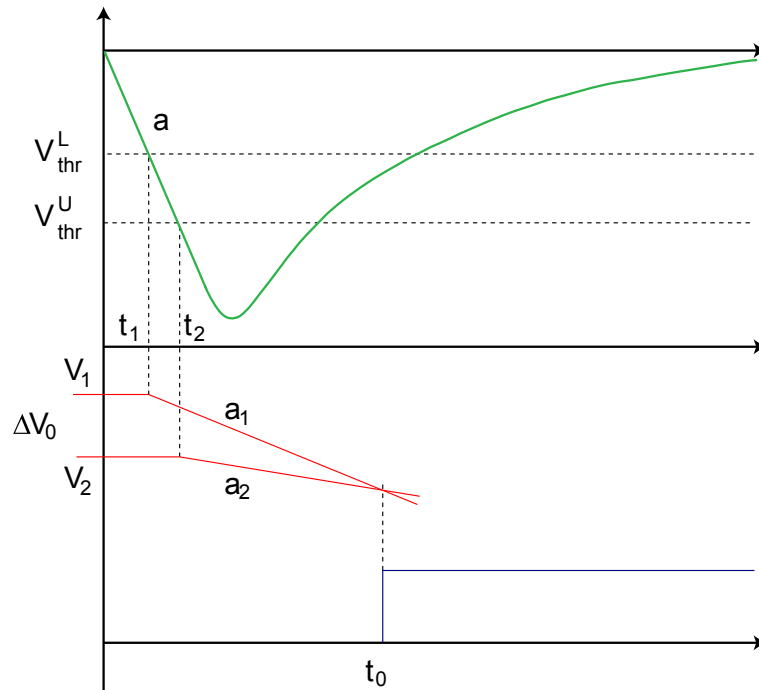


Figure 2.13: The principle of time-walk compensation in double-threshold signal discrimination. The top signal presents the time development of the input to the DTD, the bottom part shows two internal ramps with slopes a_1 and a_2 generated at times t_1 and t_2 when the input signal exceeds the thresholds V_{thr}^L and V_{thr}^U , respectively. When the voltage difference between the two ramped voltages is zero, the output signal from the DTD is generated at time t_0 .

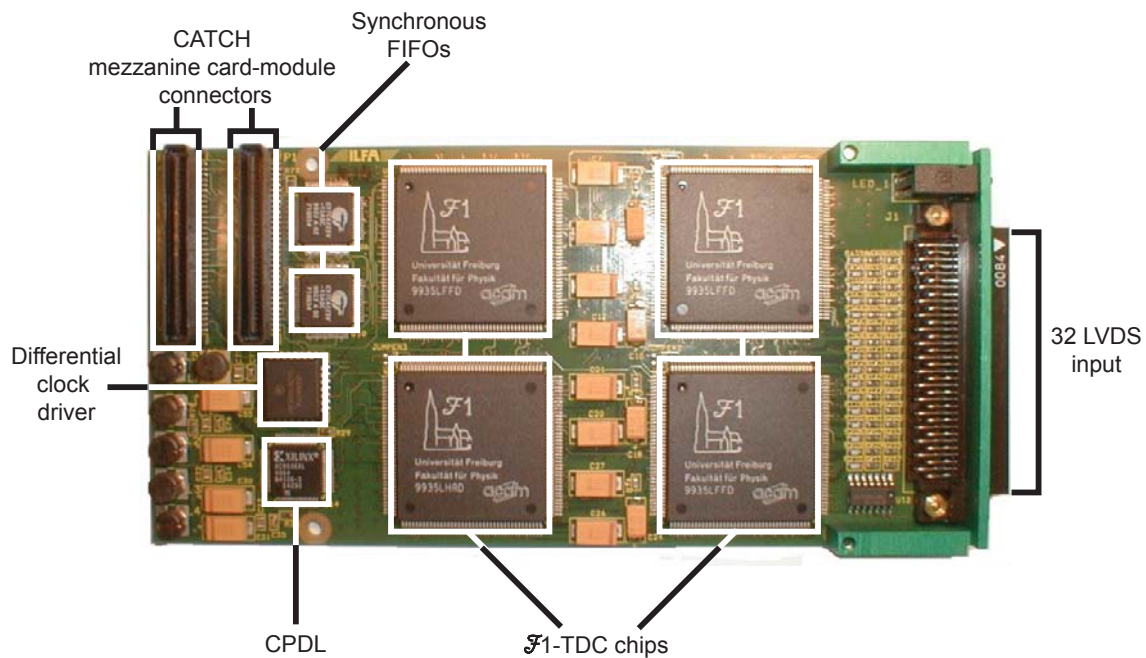


Figure 2.14: Photograph of the TDC-CMC showing the four $\mathcal{F}1$ TDC-Chips. At right is the input connector from the DTD. At left the interface connector to the the CATCH module. The FIFO controllers, the CPLD controller and the differential clock driver are labeled as complementary information.

2.3.2 CATCH Time Digital Converter

The DAQ system and synchronization of the readout modules used for the fiber hodoscope are based in the DAQ of the COMPASS experiment at CERN [111]. The 32 signal produced by the DTD are sent to a TDC-CATCH Mezzanine Card (TDC-CMC) (fig. 2.14) plugged with three more in a common readout driver module called COMPASS Accumulate Transfer and Control Hardware (CATCH).

The CATCH modules are multipurpose frontend-electronic driver and readout modules, developed for the COMPASS experiment. It is designed to house in 9U VME-crates, which provide power, interface and configuration to the CATCH modules via Linux VME CPUs through a VME interface. The events processed by the mezzanine card are transmitted via optical S-LINK, placed on the back of the VME J3 connector, to the readout buffer PC. The use of S-LINK multiplexer modules helps to reduce the number of optical links [111, 35]. A working scheme of the CATCH module is shown in fig. 2.15

The TDC-CMC hosts 4 $\mathcal{F}1$ TDC-Chips, developed by the Fakultät für Physik of the Universität Freiburg [112]. The digitization and readout, made asynchronously, is done without any dead time. The core of the chip is an asymmetric ring oscillator, made of a chain of 19 identical voltage controlled delay elements, which digitizes the actual time in a bit value. To maintain

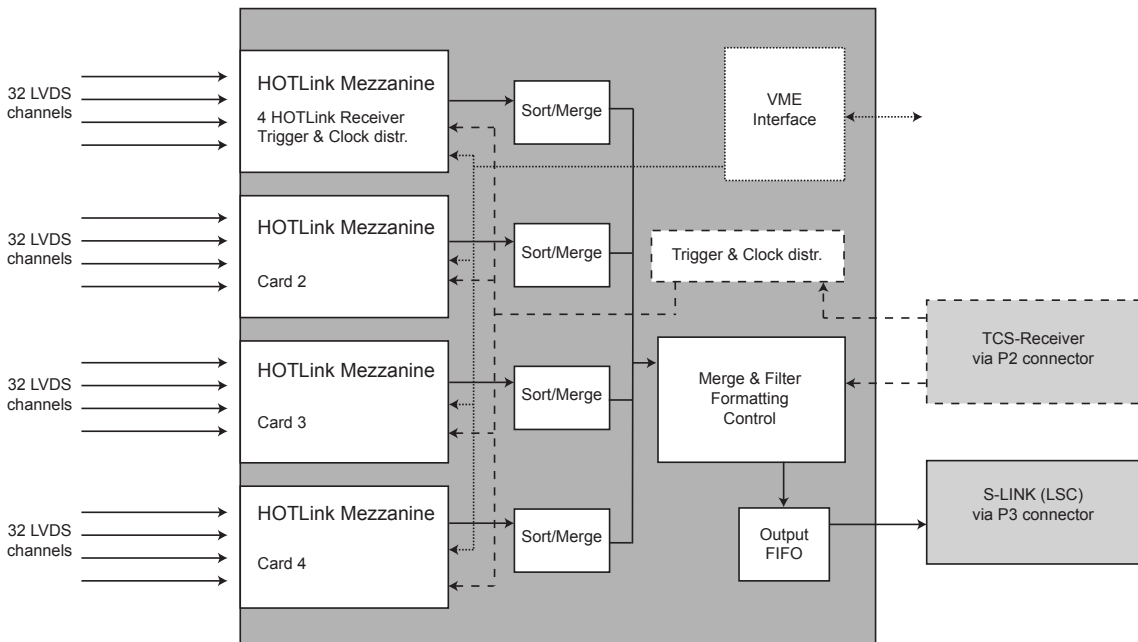


Figure 2.15: Scheme of of the CATCH readout-driver with the mezzanine cards. The lines shown the path of the data, dashed lines the synchronization signal and the dotted lines the initialization. On left, 4 flat cables of 32 LVDS signals come from the DTD. Figure from [111].

the stabilization of the delay elements over extended periods, against ambient temperature or supply voltage oscillations, a phase locked loop is used to control the ring oscillator frequency, synchronized to the 38.88 MHz reference clock of the trigger control system. The chips accept falling, rising or both edges of the input signals, and store them with the time-stamps in an internal buffer. The frequency of the ring oscillator and the time resolution of the $\mathcal{F}1$ respectively is selected with two pre-scalers, for the reference clock N and the ring oscillator M . The measuring unit has a dynamic range, internally determined in the $\mathcal{F}1$ TDC-Chips, of 62 054 steps. The length of an individual step is determined as $\Delta t = N/(fiM)$ with f the reference clock frequency and i the number of delay units. For this configuration $\Delta t = 118ps$, and a dynamic range of $62054 \times 118ps = 7.3\mu s$ making it suitable for trigger signal generation.

Detector beam-test (sec. 3.1) have shown that events registered in the TDC can be assigned to the corresponding particle track by a correlation in time and channels. This correlation is used to link a particle track to the trigger.

2.3.3 VUPROM Logic Module

The VUPROM logic module was developed at the Experiment Electronics Department of GSI for tracking trigger applications [113]. It was designed as a 6U VME board. It is equipped with a XILINX Virtex4 Field Programmable Gate Array (FPGA) chip containing over 40 K logic cells, able to operate at a

clock frequency of up to 400 MHz, and connected to a Digital Signal Processor (DSP) with 128 Mbytes SDRAM. The DSP is intended for complex trigger calculations. The FPGA can be accessed via Joint Test Action Group (JTAG) connector. A CPLD can be accessed via VME bus to program the FPGA, the DSP and provide support to a 256 Mbit flash memory. The flash memory can store up to four configurations, the first one is used for default configuration at start-up of the board and the other three can be activated over VME command. A display on the front panel is accessible from the DSP and can be used to show the status information of the module. Four VHDCI connectors, with 32 channels each, on the VUPROM main board are hard wired as three inputs and one output. Four piggyback options allow additional in/output options, making a total of 256 channels per board. Additionally, two LEMO connectors, input and output (TTL or NIM level), are placed in the front plate of the board [35] [113]

2.4 Design and Construction of the fiber detector

The fiber detector request implies a compact design of the fiber bundle, an interface between the bundle and the PMT and, from simulations, an estimation of the length of the plane in order to cover the estimated focal plane. Also, during the mass production phase, it is important to implement a systematic construction process and to avoid mistakes on the modules that can lead to erroneous measurements.

2.4.1 Design of the fiber bundle

As said before, the tracking detector has to fulfill the requirements of high counting rate, high granularity, compact geometry and small thickness. The high granularity, compact geometry and small thickness is obtained by the use of scintillators fibers (sec. 2.1) in a compact array, as explained below. The high counting rate through the MAPMT and the TDC-CMC/CATCH modules, explained in the previous section.

The construction principle of a tracking fiber bundle is to build it in a way that the particle trajectory is parallel to the fibers grouped together to one common pixel of the readout device, minimizing the multiplicity of the event which compromises the tracking capabilities of such detector. The most simple arrangement is when the columns are perpendicular to the construction base. It allows to add any number of layers if the light yield per crossing particle that is too small to be detected with efficiency (see section 2.1), until a physical limit or when some restriction about small angle scattering is reached. This configuration applies to many applications since the angular acceptance for fiber hodoscopes is generally small, typically up to $\theta \sim 3^\circ$ w.r.t the normal of layers.

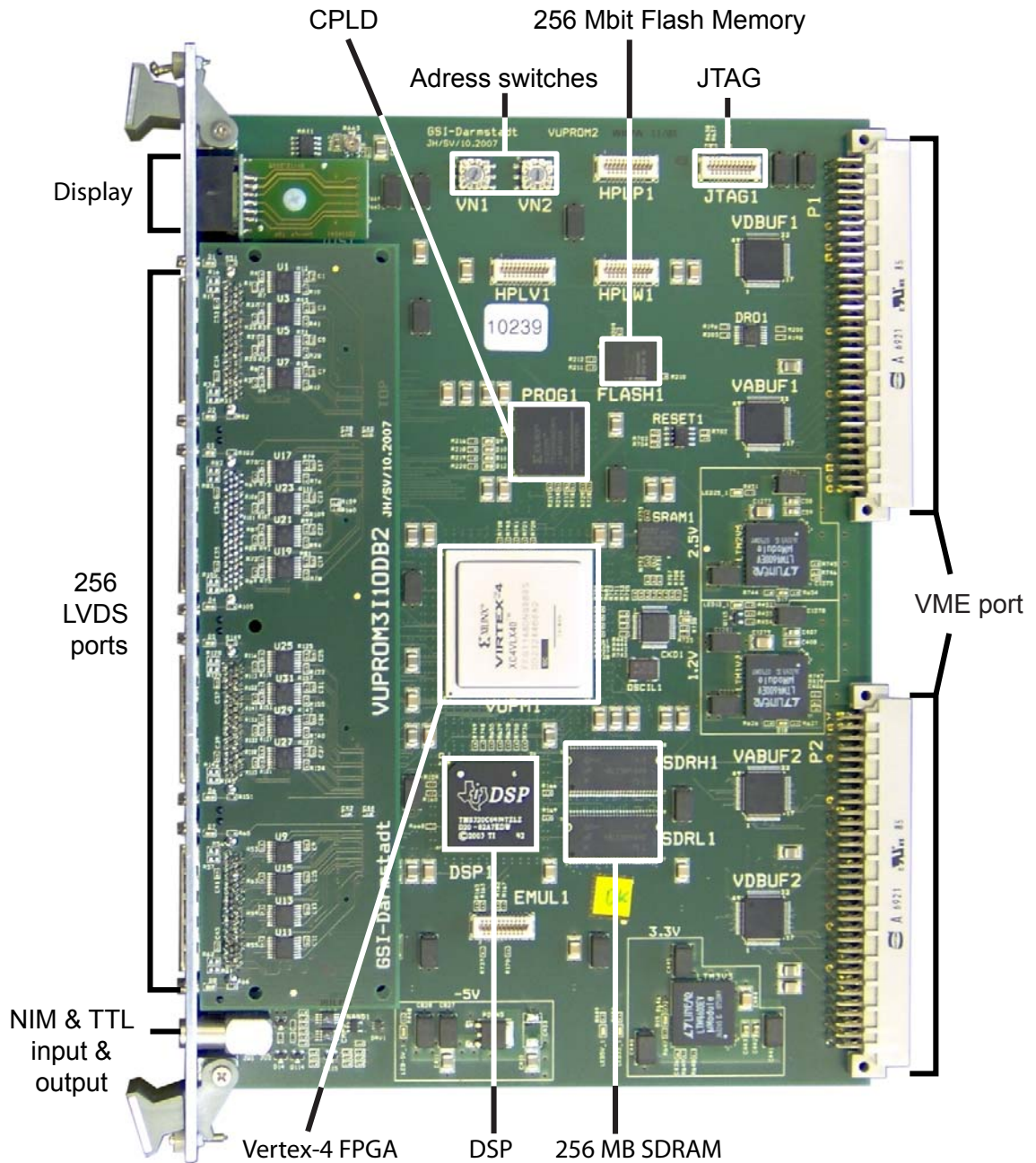


Figure 2.16: Photograph of the logic module VUPROM used in the trigger system of the fiber detector. The LVDS ports, at left, are divided in 8 individual ports handling 32 channels each, making a total of 256.

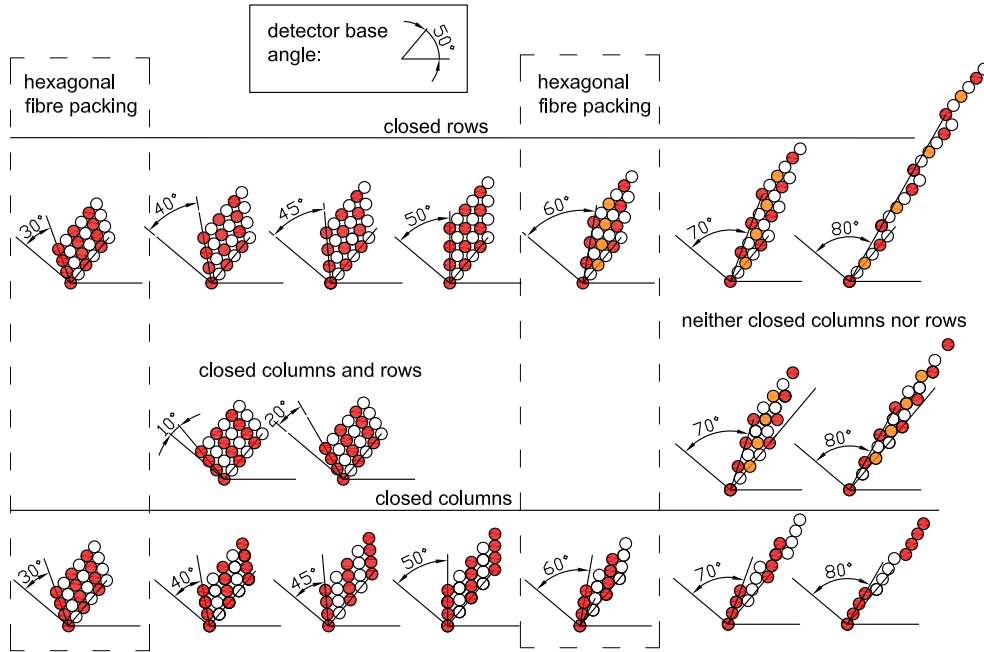


Figure 2.17: Different fiber arrangements geometries with inclined columns. With a ϕ range from 10° to 80° and a rotated detector base of 50° . The upper row shows the geometries with closes row configurations, the lower row, with closed columns. For columns angles of 10° and 20° the configuration is of closed row and columns. Columns angles of 30° and 60° the fiber centers form an hexagonal lattice. For a column angle of 45° the fiber centers are forming a square lattice. Figure from [114].

Nevertheless, in some applications, the incident particle will cross the detection plane with larger angles and would traverse several neighboring columns and compromise the tracking capabilities of such a detector, *e.g.* in the KAOS spectrometer, the average incident angle, w.r.t. a plane following the estimated focal plane at the electron arm, is $\theta = 65^\circ$. The solution is an arrangement with inclined columns w.r.t the detector base. There are many ways to arrange the fiber with inclined columns, however, it has to be able to be built and meet the requirements of the experiments.

Figure 2.17 shows different geometries with different column angles ϕ and four fibers per column. Each geometry corresponds to different arrays with inclined columns. Configurations of closed rows allows larger overlap between neighboring columns, greater spatial resolution and bigger detection efficiency. With columns angles of 30° and 60° , the fibers centers form a hexagonal lattice which provides the highest packing density $\eta_h = \pi/\sqrt{12} \simeq 0.90$, and therefore the most stable structure.

Figure 2.18 (left) shows the ratio of the column pitch to the fiber radius p/ρ , *i.e.* the distance between two neighboring fiber centers, measured perpendicular to the direction of the readout columns. The continuous curve,

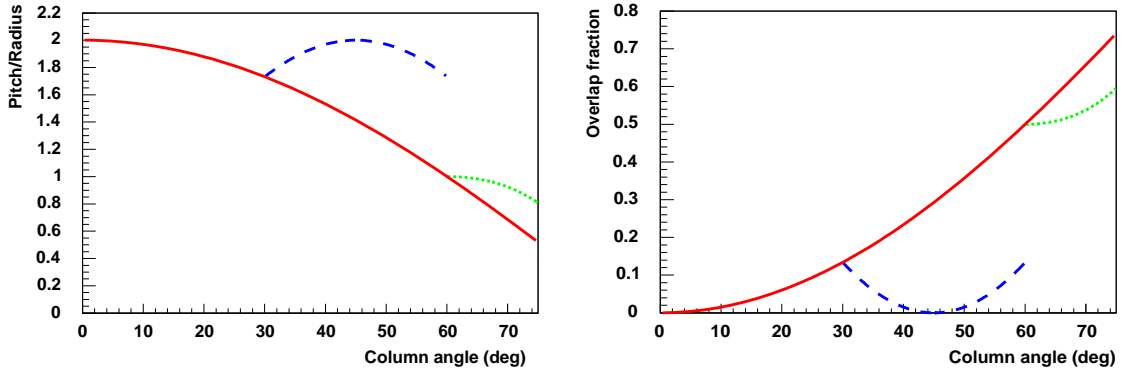


Figure 2.18: The left plot shows the ratio of the column pitch to the fiber radius as a function of the column angle ϕ . The right plot shows the overlap of two neighboring fiber columns in units of the fiber radius. The continuous curve corresponds to a geometry with closed rows, the two branches that are splitting off to geometries with closed columns. Figure from [114].

corresponds to a geometry with closed rows and columns, for which $p/\rho = 2 \cos \phi$. The dashed curve to a geometry with closed columns, where $p/\rho = 4 \sin \phi \cos \phi$ and the dotted curve corresponds a configuration of closed columns with $p/\rho = 4 \sin \phi / \sqrt{9 + \tan^2 \phi}$. In the fiber array for tracking purposes, it is important to avoid gaps between fibers columns losing detection efficiency. Figure 2.18 (right) shows the overlap fraction of two neighboring fiber columns in units of fiber radius o/ρ . It is related directly to the pitch to radius ratio by $o/\rho = (2 - p/\rho)$. Fiber diameter, \varnothing , and overlap fraction are related to the theoretical spatial resolution of the fiber array expected from the geometry. Events in which only one column was hit, the spatial resolution is $\sigma = (\varnothing - 2o)/\sqrt{12}$ and for events in which the particle covered exclusively the inter-column region $\sigma = o/\sqrt{12}$. Averaging both events, $\sigma = \{(\varnothing - 2o)^2 + o^2\}/\sqrt{12}$. For hexagonal packing fiber arrays, the total overlap is $o = \varnothing(1 - 1/\sqrt{2})$ with a pitch of $p = \varnothing/\sqrt{2}$, therefore, the theoretical spatial resolution for such an array is $\sigma = (9/\sqrt{2} - 6)\varnothing/\sqrt{12} \approx 0.1\varnothing$

The energy deposition in a fiber detector is proportional to the detector thickness variation. Figure 2.19 shows the different mass thickness for $\phi = 0^\circ, 45^\circ, 60^\circ$ and 70° . In the hexagonal packing at $\phi = 60^\circ$ the variation is $\delta t \sim 70\% \varnothing$ from minimum to maximum. Although for all other column angles configuration, depending on the geometry, the variation can become smaller, but the difficulty in constructing such geometries make them not viable.

So far in the discussion, only particles crossing the fiber array with the same incident angle as the column angle had been considered. From simulations, the behavior of different arrays for particles crossing the array with different incident angles can be studied. With the use of the Geant4 framework [115], 45° and 60° fiber columns arrangements were simulated with different

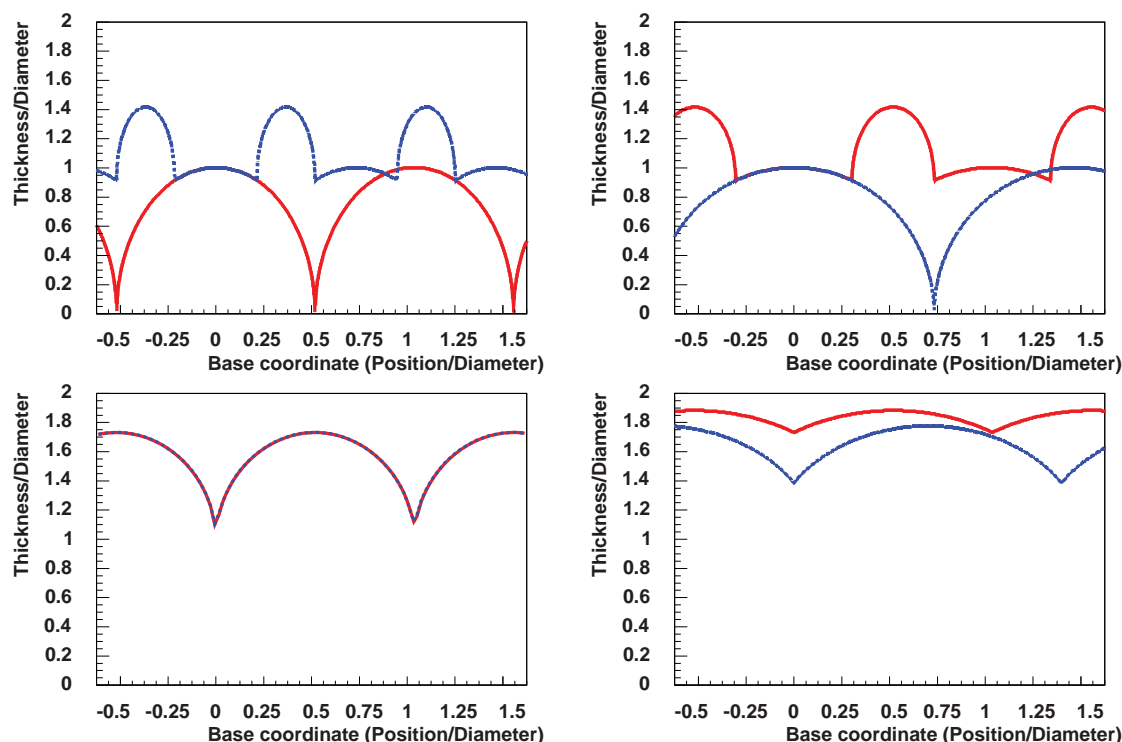


Figure 2.19: Thickness variation as a function of the base coordinate for different fiber array geometries: column angle $\phi = 0^\circ$ (top left), $\phi = 45^\circ$ (top right), $\phi = 60^\circ$ (bottom left), $\phi = 70^\circ$ (bottom right). The two curves correspond to geometries with closed columns (full curve) and closed rows (dotted curve). Figure from [114].

electron incident angles θ with respect to the normal of the detector base. The simulation gave information on the energy deposition in individual fibers and on interactions of the particles with the material as small angle scattering, ionization and bremsstrahlung. The total energy deposited in the active cores of the four corresponding fibers of each column was calculated and signals above a given threshold were assigned to the corresponding read-out channel.

The results from the simulations are presented in fig. 2.20. Multiplicity plots as function of the incident angle show a natural minimum when $\phi = \theta$ and that the multiplicity increases smoothly to a smaller incident angles and steeper to higher angles. It is obvious, from this results, that the columns must be aligned with the direction of the incident's particle and the particle's divergence must be small in order to achieve minimal multiplicity and providing a better spatial resolution.

Simulations can also provide information in order to help to define an optimum threshold where the detector becomes insensitive to particles with larger incident angles θ (fig. 2.20 lower row). The relative thresholds of 100% corresponds to the mean signal of a detector channel for events with incident particles with nominal angle. For incident angles much smaller than the nomi-

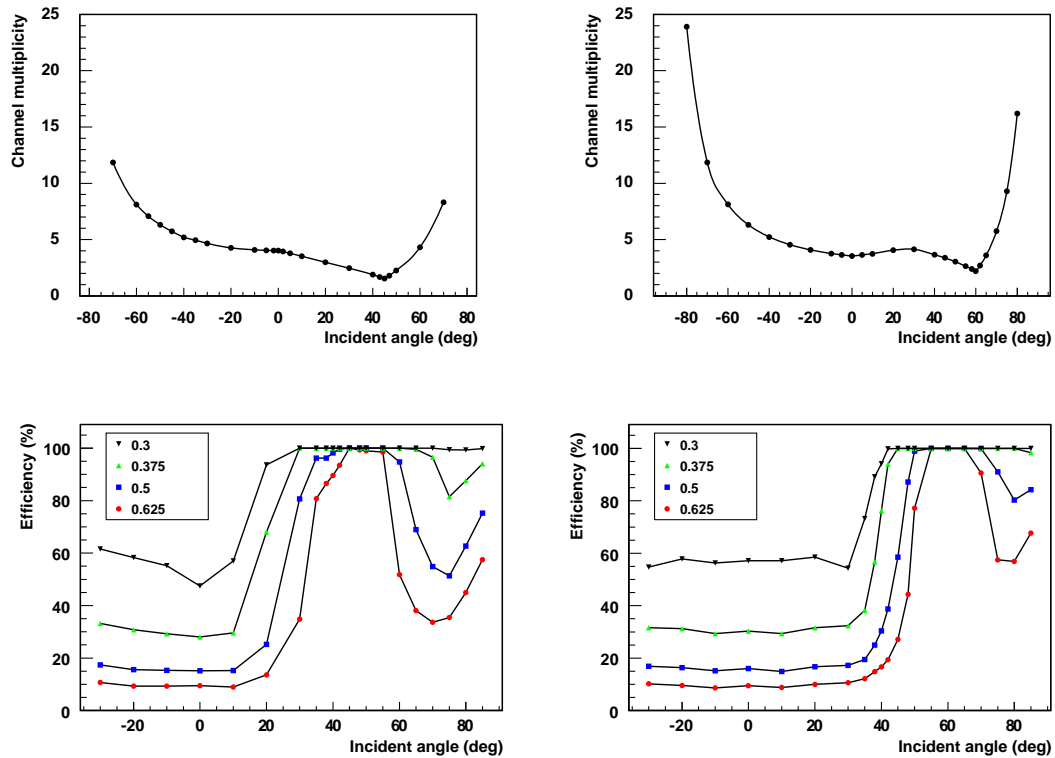


Figure 2.20: (Upper row) Simulated variation of the channel multiplicity as a function of the incident angle θ for fiber array with closed row and columns angles of 45° (left) and 60° . (Lower row) Simulated variation of the efficiency as a function of the incident angle θ for fiber array with closed row and columns angles of 45° (left) and 60° . Figure from [114].

nal angle, only one fiber of each column is hit, but due to the higher multiplicity, many neighboring channels are hit. Therefore, the probability for having a signal in at least one pixel above threshold is strongly dependent on the distribution of energy deposition and the value of the threshold, but independent on geometry and incident angle. [114]

2.4.1.1 Fibers bundles designed in Mainz

The fiber detector concept used in Mainz is based on the fiber hodoscope station in COMPASS [116] therefore the firsts prototypes were based on this design [117]. It consists in 4 double layers with 0.6 mm pitch between two adjacent fibers in the same layer. With this arrangement, the minimum multiplicity is obtained with particles arriving with $\theta = 0^\circ$ w.r.t the normal of the plane generated by the bundle (fig. 2.21). It shows a very stable structure and demonstrates the feasibility of the construction of long fibers arrangements.

Although this design was not suitable for the tracking detector for KAOS spectrometer, it allows an easy way to study the response of the fibers along-

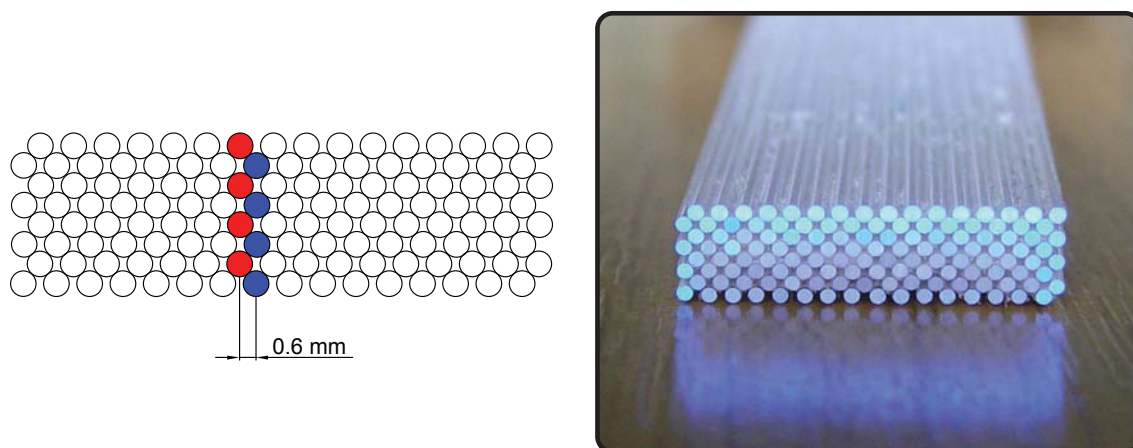


Figure 2.21: Left. Scheme of the fiber arrangement of 0° . Columns of the same color represent a single readout channel. The pitch between each column is of 0.6 mm. Right. Photograph of the bundle arrangement.

side the MaPMT (sec. 3.1).

From this arrangement, a natural slanted columns arrangement can be made with simple translation of the columns. But for symmetry reasons it was adjusted to achieve an inclination of $\phi = 45^\circ$ as shown in fig. 2.22 (left). It has the same pitch between columns of 0.6 mm as the $\phi = 0^\circ$ design. Despite the fact that the design derives from a very stable array, the geometry is intrinsically different and also the construction. Its building process makes it very difficult to obtain a stable array during the gluing phase and many misalignments appear in the final bundle as shown in fig. 2.22 (right). Even some tests were done to study the performance of such an inclined array under beam conditions [118].

As mentioned before, the mean incident angle, estimated from the first simulations, is $\theta \approx 65^\circ$. From the study of the different geometries discussed before, the arrangement closest to the requirements with enough stability is with $\phi = 60^\circ$ with closed row configuration. The pitch between neighboring columns is of 0.42 mm. It has shown a very stable process of construction, giving no deviations of the fiber positions by no more than $0.25\varnothing$. This layout fiber detector was tested in GSI before the serial production of the bundles (sec. 3.2).

2.4.2 Increasing the Light yield

As calculated in sec. 2.1, the light fraction collected in the SCSF-78M multicladding fiber in one side is only of 5.3%. The light directed to the other side is lost if no detector or reflection material is placed. In the KAOS spectrometer, the option of detectors at both sides of the fibers is not possible. Instead, gluing a reflective material, that will decrease the amount of light reflected due to

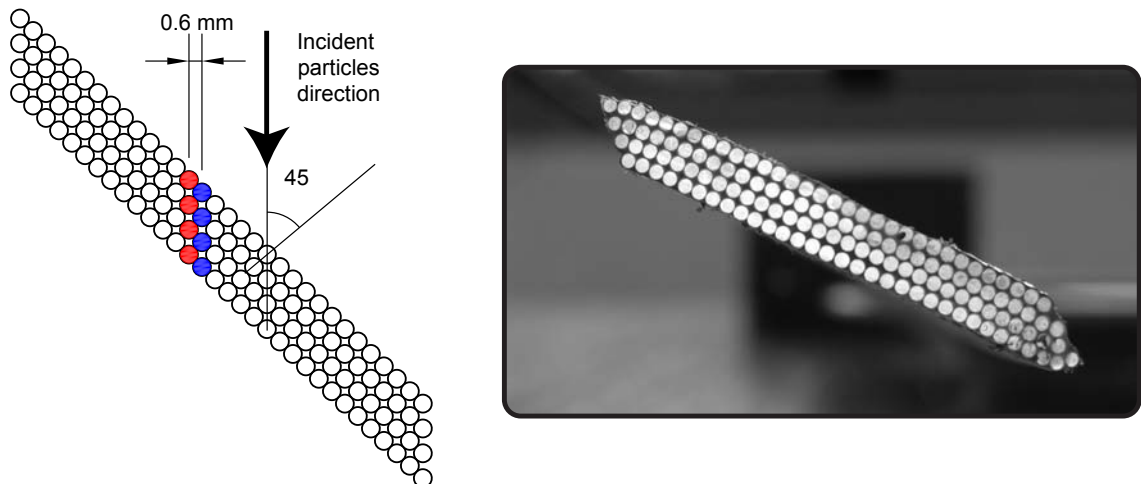


Figure 2.22: Left. Scheme of the fiber arrangement of $\phi = 45^\circ$. Columns of the same color represent a single readout channel. Right. Photograph of the bundle arrangement. The misalignment is visible on the fibers, making it not suitable for tracking purposes.

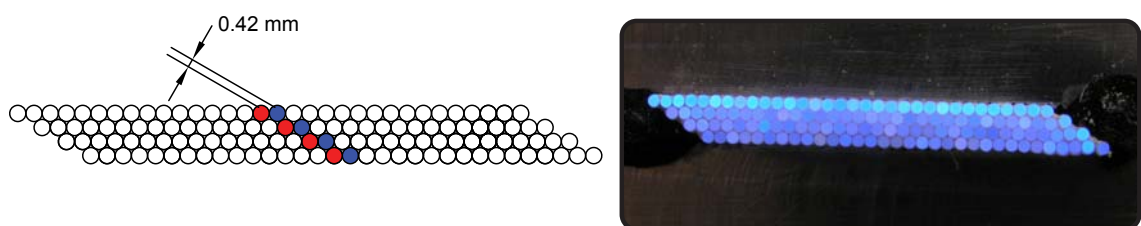


Figure 2.23: Left. Scheme of the fiber arrangement of $\phi = 60^\circ$. Columns of the same color represent a single readout channel. Right. Photograph of the bundle arrangement.

imperfections in the interface fiber-glue-material, some reflective material was vaporized.

It was done through a vacuum chamber with a high current electrode with a tungsten boat where the material pellet to be vaporized is placed. Regular materials for reflection purposes are aluminium or silver. From fig. 2.24 the reflectance at 450 nm, which is the maximum emission of the SCSF-78M (fig. 2.3), is lightly higher for aluminium, $\approx 91\%$ and $\approx 89\%$ for silver. This makes the aluminium an optimum and inexpensive solution.

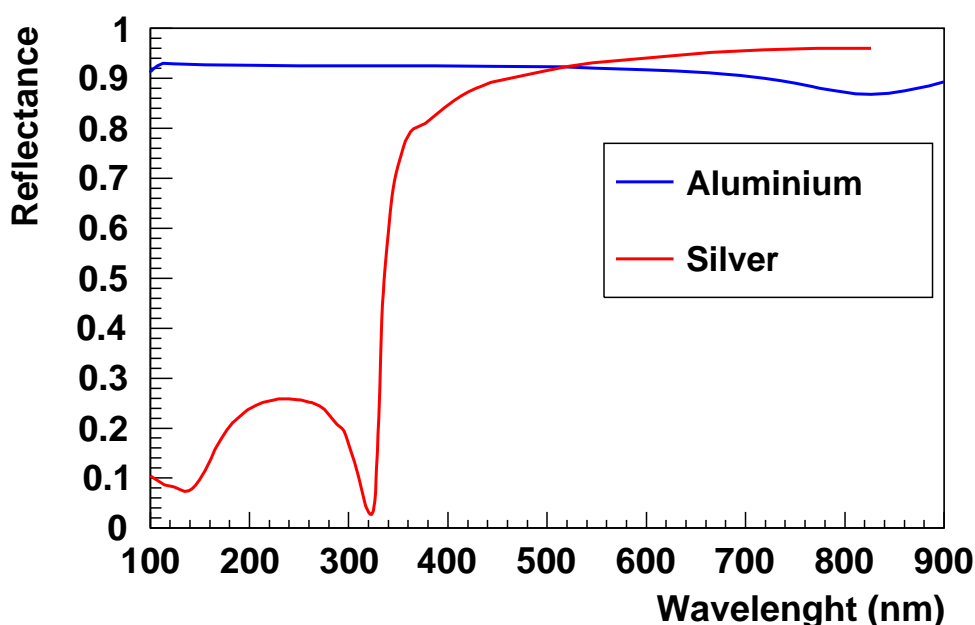


Figure 2.24: Reflectance spectra of aluminium and silver at normal incidence in function of wavelength. Data extracted from [119]

The vacuum chamber (fig. 2.25) consists in a Duran glass cylinder from SCHOTT AG, of 505 mm tall and 335 mm diameter, in a table with a vacuum system and a electrical oven system attached. The vacuum system consists in an air pump compressor, for pre-vacuum, and a jet pump, for high vacuum. On the top of the glass cylinder is an aluminium cap which has a manometer and a pirani for pressure control and also where the fiber bundles are fastened through an extension due to the length of the fibers. The electrical oven is a pair of titanium electrodes holding a tungsten boat with both electrodes connected to a high current supply and covered with a shutter. The system is able to vaporize three bundles at time.

A test with the prototypes of $\phi = 0^\circ$ were done, measuring the ADC of one channel before and after the vaporization. The test with the prototypes

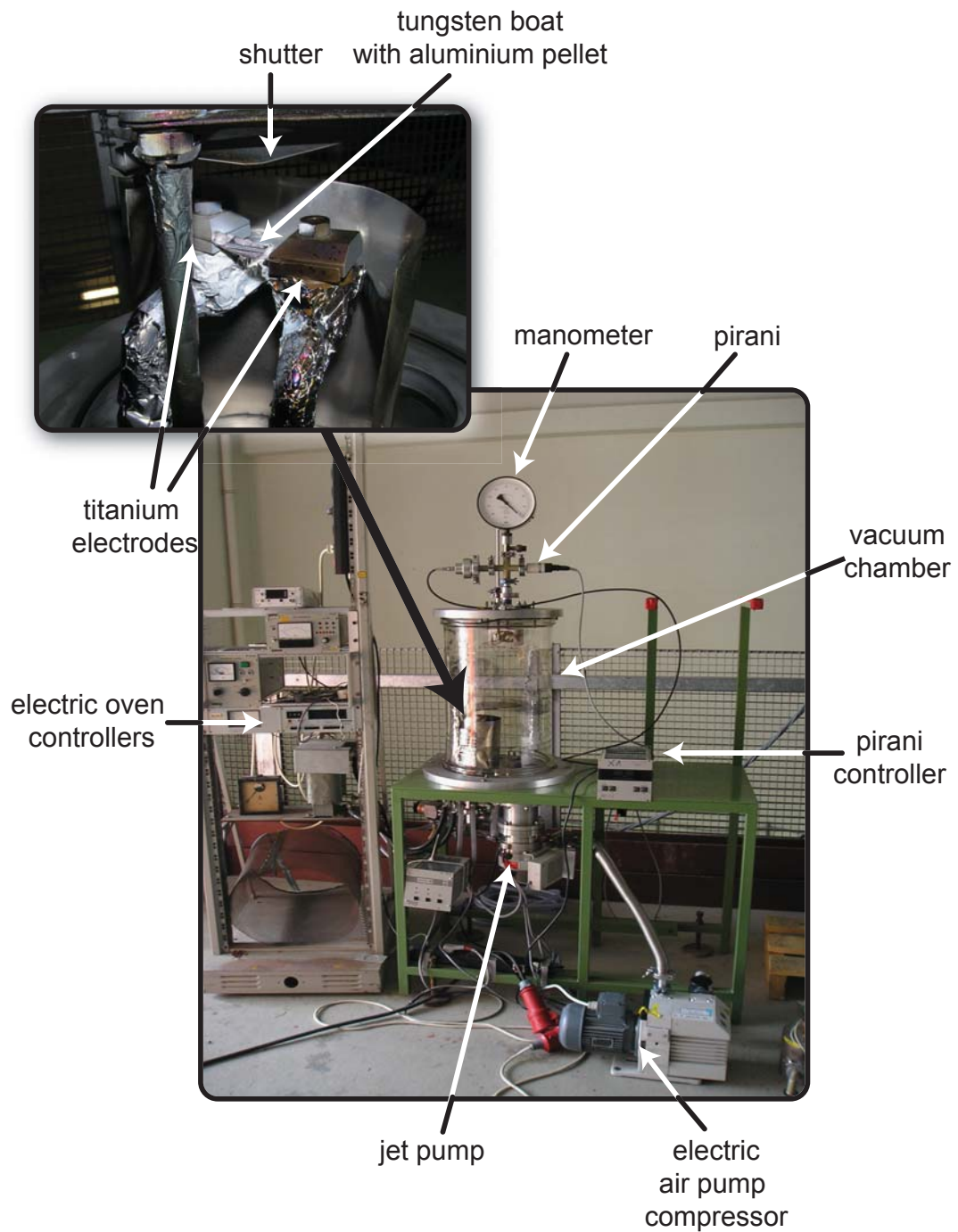


Figure 2.25: Photograph of the vacuum system for vaporization showing the relevant parts of the system. Top left. Detail of the titanium electrodes with an aluminium pellet in the tungsten boat

shows an improvement of the light yield of 14% on the vaporized fiber bundle w.r.t the detector without reflecting aluminium (fig. 2.26 (down)). Noteworthy that the aluminium is not glued to the fiber, only deposited. Handling the bundle at this moment should be done with extreme care, without touching the aluminized surface (fig. 2.26 (up))

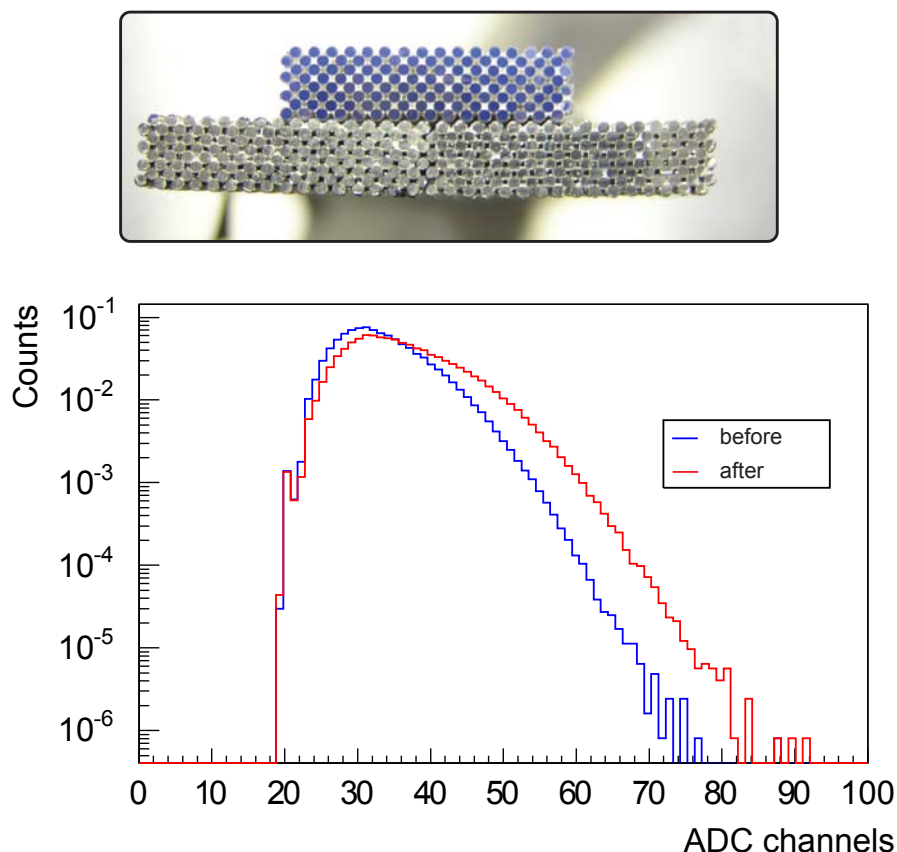


Figure 2.26: Top. Photograph of three prototypes fiber bundles. The two lower bundles are aluminized, meanwhile the upper bundle was keep it clean for comparative purposes. The left bundle shows some lose of the aluminium cover, probably due to bad handling of the fiber bundle. Bottom. Logarithmic plot of the normalized ADC signal from the fiber bundle, the blue line indicates before aluminization and red after the aluminization. An increase of light yield of 14% was achieved.

2.4.3 Design concept of the fiber hodoscope

The fiber detector for the KAOS spectrometer should be able to cover most of the electron side focal plane and reconstruct tracks of the particles and therefore the momentum. The minimum need is at least two planes for position and angle coordinates determination in the dispersive plane. The

layout of the fiber bundles was discussed before (sec. 2.4.1.1). The length of the fiber detector was determined through the acceptance of the kaon and the hypernuclear production since there is a strong correlation between the kaon produced, and the scattered electron of a hypernuclei electroproduction reaction (fig. ??).

From a first calculus of the dispersion of $4 \text{ cm}/\%$ [86] with a central momentum at the electron side of the KAOS spectrometer of 390 MeV, the length of the detector at the focal plane should be slightly smaller than 1840 mm. Thus, the second plane necessary for angular determination should be longer, since it is expected that the particles disperse after the focal plane. In practice, the detectors are placed in a way that the focal plane is situated in between, increasing the size of the first plane and reducing the second. Also it is mandatory a compromise to accommodate the planes into a new vacuum chamber (app. A.4) and that the whole set can be allocated at the side of the magnet. The length also has to be a multiple of the length of three bundles, since the front-end board accommodates three modules. Since each bundle is $0.83 \text{ mm} \times 32$ fibers long = 26.56 mm, the length should be a multiple of $26.56 \text{ mm} \times 3 = 79.68 \text{ mm}$.

With the use of CAD drawings of the spectrometer and the first versions of the simulations in order to situate the focal plane, the length of the first plane was decided to be of 1912.32 mm which corresponds to 24 front-end board \times 3 modules/board \times 32 fibers long \times 0.83 mm. The second plane length, besides fulfilling the previous requirements, should be able to detect all particles from the reaction detected by the first plane. Again with the help of the simulations and the CAD drawings, the optimum size was determined. In order to avoid an excessive increase of the length due to the divergence of the particles after the focal plane, the detector is placed at a distance similar at the first plane w.r.t the focal plane. With this consideration, the second plane has the same length of the first plane. Nevertheless, the final position will vary greatly with the design of the vacuum chamber in conjunction with the support plate of the fiber detector in order to accommodate both planes closer to the desired position from simulations, even with the loss of some acceptance (fig. 2.27).

The fibers forming the bundle are glued directly to an interface or “cookie” (app. A.1), which directs the four fibers of a channel to the corresponding pixel of the MaPMT. Also, the cookie works as a fixation of the MaPMT. Unlike many other fibers detectors, the fiber detector in Mainz does not use optic fiber between the scintillator fibers and the PMT [116]. It implies that two of three fiber bundles should be bent close to the cookie in order to conform a plane and be able to connect to the PMT as they are placed in the front-end board (sec. 2.2.2). The position of the PMTs in the front-end board were determined from the width of three consecutive fiber bundles and from this, the bend of the fiber bundles were determined by the minimum separation of the three PMT. For stabilization and reduced stress from the bend, the fibers were bent in an oven at 70°C for one hour. Previous tests show that the process do not

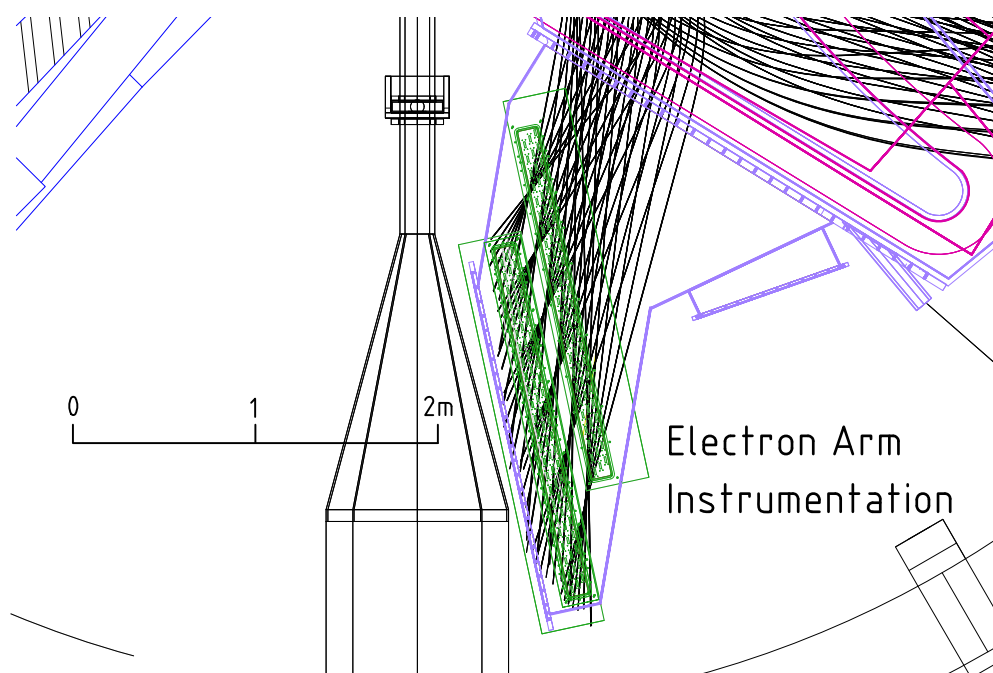


Figure 2.27: CAD detail drawing of one of the firsts simulated particles tracks at the electron arm of the KAOS spectrometer. The converging points of the tracks are situated over the focal plane. The green frame represents the supporting frame of the fiber detectors. The purple frame represents the vacuum chamber and the pink the magnet. Can be seen that the plane at right can not be moved more closer to the magnet due to the dimensions of the supporting frame, introducing some modification respect to the estimated position losing some acceptance respect what was expected.

destroy the fiber or change the physics behavior of the fiber and that the bent is quite stable after the heat application (fig. 2.28). The curvature of the fiber should be soft enough to avoid light loss due to the curvature. Further tests had shown than the bending did not introduce significantly light loss (fig. 2.29 down). The height of the fiber detector depends on two considerations, the acceptance in the non-dispersive plane of the spectrometer and enough length to bend the bundle without a big curvature radius, as explained before. For a smooth curve, the length of this part is of 165 mm. The exposed area to the scattered particles should end slightly higher over the plane at $\phi = 0$, with ϕ the non-dispersive angle in order to reduce Møller electrons and Bremsstrahlung at the detector. Since the spectrometer can vary its height position with respect to the height of the target, the acceptance in ϕ can be increased in one direction (sec. 1.2.2). The estimated length of the exposed area of both planes is of

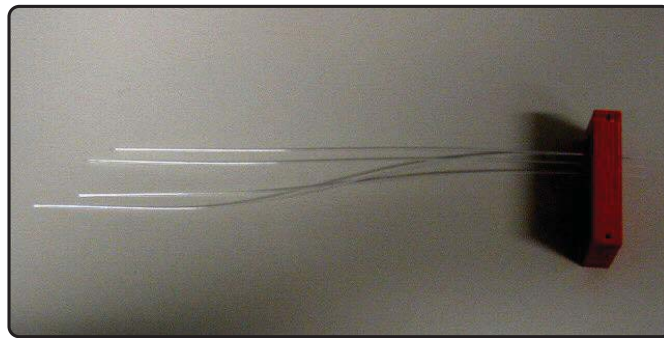


Figure 2.28: Photography of the bending test of singles fibers after heating. Three of them were bent just a few millimeters from the straight position and one was bent higher distance, comparable as the fiber bundles of the detector will be bent.

297.5 mm, making a total height, from the cookie to the end of the fiber bundle, of 422.5 mm.

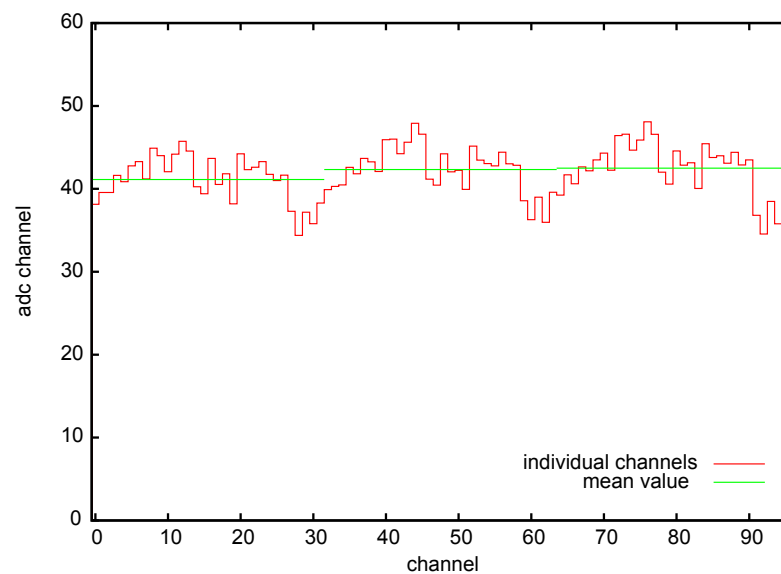


Figure 2.29: Plot of the ADC mean value of every individual channel for three consecutive fiber bundles made on a test beam and mean value of every bundle (green). The side bundles, channels 0 - 31 and 64 - 95, are bent to fit with the front-end board (sec. 2.2.2). It shows that even the shift on displacement is big the light transport is not reduced significantly [120].

Finally, the bundle will be positioned vertically with the PMT on top. This helps to obtain higher stabilization of the detector plane keeping a better verticality.

2.5 Construction of the fiber detector

2.5.1 Construction of the fiber bundle

The construction of the chosen fiber bundle, $\phi = 60^\circ$ slanted columns with closed rows (sec. 2.4.1.1), was done with the help of an aluminium position matrix, which helps to allocate the fibers and keep them in position meanwhile the gluing process was conducted. The position matrix has a size of $500 \times 95 \text{ mm}^2$. Its cross section and the way the fiber are positioned is shown in fig. 2.30, the technical specifications are given in the appendix A.2.

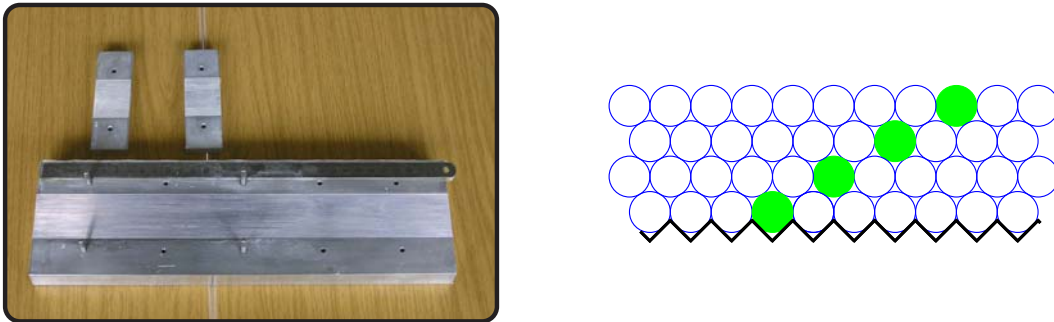


Figure 2.30: (Left) Photography of the position matrix for the build of the fiber bundle and two position jigs to keep the glued bundle pressed during the curing phase. (Down) Cross section of the position matrix, black line, with the fibers allocated. The green circles represent the four fiber corresponding to a single read-out channel.

During the building process, the use of dummy fibers is mandatory for the side where the fibers form an upper wedge. These dummies are retired later. A scheme of how the fiber bundle should be assembled is shown in fig. 2.31. The scheme shows the fibers view layout at the end of the bundle, opposite where the PMT will be placed. This is important since the layout is not symmetric and the inclination of the columns is different if the PMT is on top or on bottom when is positioned with the particles coming from the spectrometer.

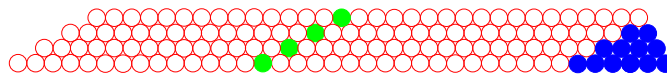


Figure 2.31: Scheme of the layout of the fiber bundle how should be assembled. The green circles represent the four fiber corresponding to a single read-out channel. The blue circles represent the fiber dummies necessary for the assembly of the fibers of the upper wedge.

The fibers are cut in 50 cm long pieces, since they come packed from the manufacturer in bunches of 2 m long or in a continuous roll. Each bundle needs $32 \text{ channels} \times 4 \text{ fibers/channel} + 12 \text{ dummies} = 140 \text{ fibers}$. The fibers are

manipulated with latex gloves to avoid scratches at all times. The fibers are glued with acrylic white paint with 10% in volume of water.

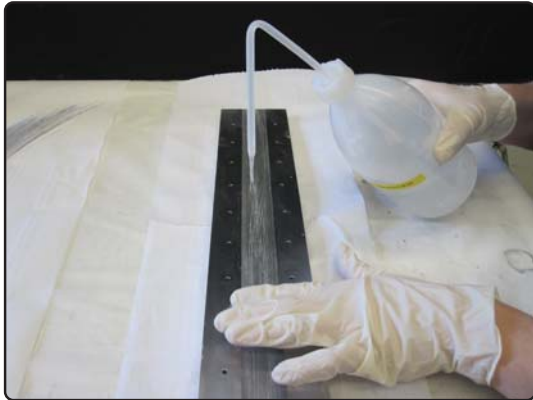
The process is as follows. First, over the position matrix is put a little bit of water, enough to moisten the surface where the fibers will be placed (fig. 2.32a). Putting water helps to keep the fibers in position and facilitates to remove the bundle after the paint is totally dry. Then, a first layer of 32 fibers are placed in the matrix, leaving a small length out of the matrix (fig. 2.32b). It helps to control the length of the fiber and remove the bundle from the matrix. Immediately, 6 dummies are placed contiguous to the layer, but in this case leaving a longer length than the normal fibers to identify clearly when they must be removed (fig. 2.32c). Once all fibers are placed, a light layer of paint is applied with a soft brush covering an area of ≈ 35 cm long (fig. 2.32d). Then a second layer of fibers is placed (fig. 2.32e). If it is necessary, more paint could be applied. It is important to apply an homogeneous quantity of paint in the internal part of the bundle since previous bundles built have been destroyed by the stress between zones painted and zones with lack of paint. The process is repeated two layers more until the desired layout is achieved (fig. 2.32f). The whole process takes between 20 - 30 minutes.

2.5.2 Polish of the end side of the bundle

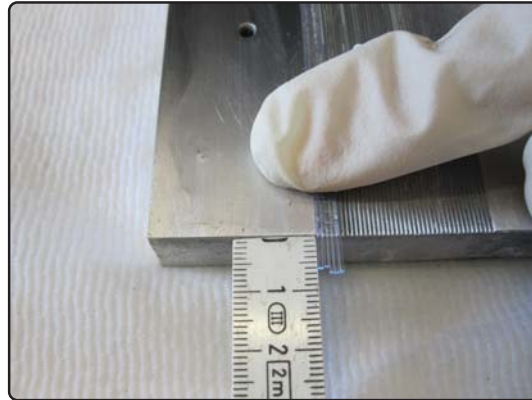
Once the bundle is built, it is left curing with the position jigs pressing the bundle for 24 hours. After this time, the bundle is carefully removed from the position matrix. The dummies are removed one by one taking care not to unglue the fibers (fig. 2.33a), specially the last one which only touches one fiber. Then a paint layer is applied in the surface which was in contact with the matrix and the edge where the dummies were. The bundle is placed in a plastic block with its shape to manipulate during the polishing process and not lose the position of the fibers. The first step is reducing the end of the bundle with a manual diamond saw (fig. 2.33b). The rest of the excess of the bundle (fig. 2.33c) is reduced to the level of the block with an electric sand paper machine (fig. 2.33d). Doing this facilitates the final polish with the high precision saw machine DIAPLAIN 6300 from MUTRONIC (fig. 2.33e). After the last polishing, the end of the bundle is ready (fig. 2.33f). The process takes around 20 minutes.

2.5.3 Assembly of the fiber bundle with the cookie

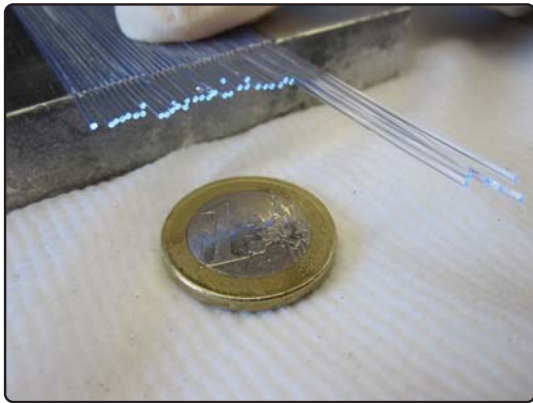
The bundle is now placed in an other plastic crimping block with its shape, but holding the whole body of the bundle, *i.e.* the corresponding part for detection. The polished end is leveled with the border of the crimping block (fig. 2.34a). The plastic block is attached to an aluminium plate and at the opposite side of the block is attached the cookie at the desired distance



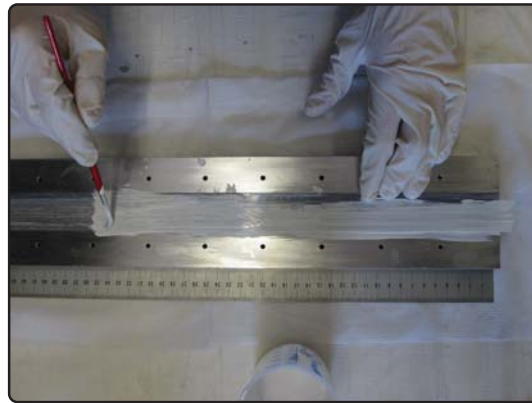
(a) Moisten of the matrix surface to hold the first layer.



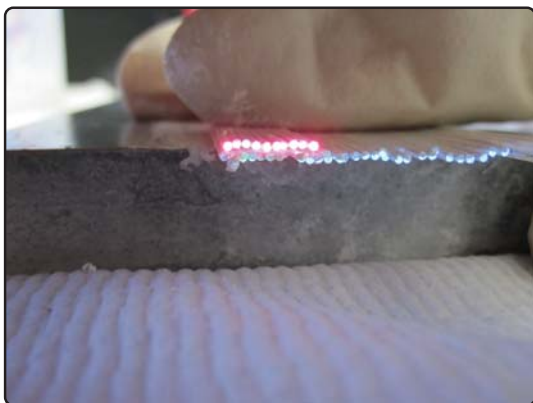
(b) Detail of the fibers in the matrix slightly out of the matrix.



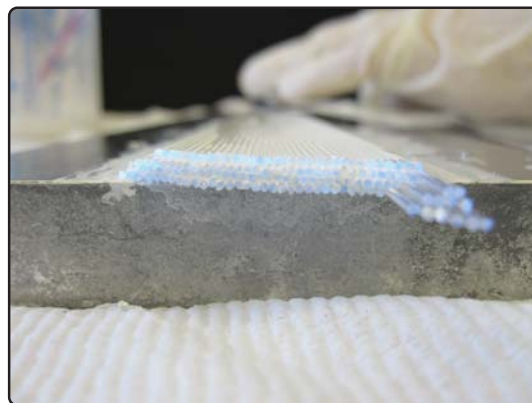
(c) First layer ready showing the fiber dummies remarkably out than the main fiber bundle.



(d) Application of the paint to the first layer.

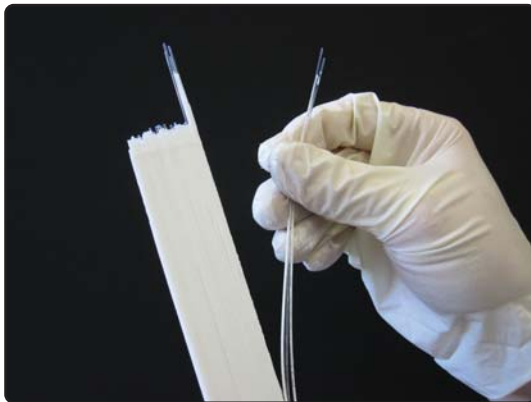


(e) Placing of the second layer, illuminated with red light for better identification.

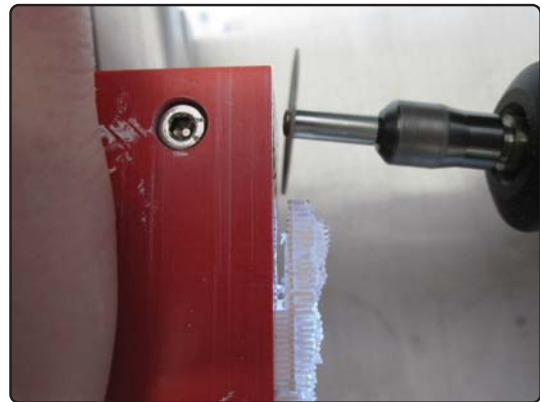


(f) Bundle finished and ready for curing.

Figure 2.32: Steps of fiber bundle construction.



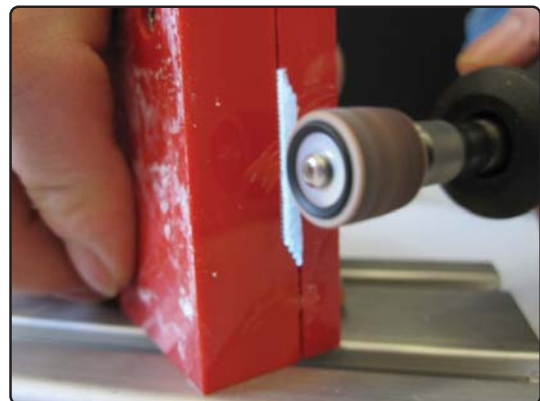
(a) Withdraw of the dummies fiber from the main bundle.



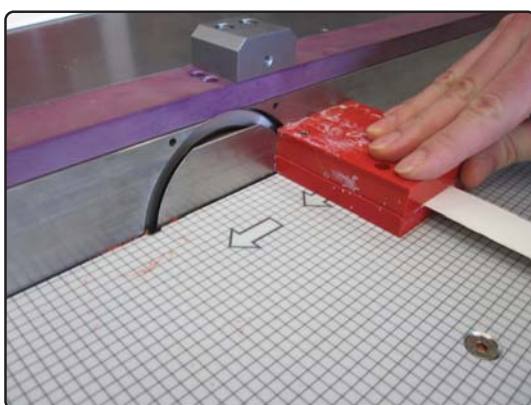
(b) Reduction of excess of fibers with a manual diamond saw.



(c) Detail of the block containing the bundle after the cut.



(d) Leveling the rest of the bundle with rotating sand paper.



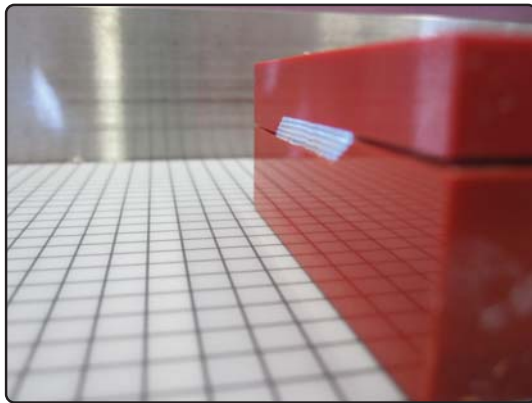
(e) Final polish with high precision saw machine.



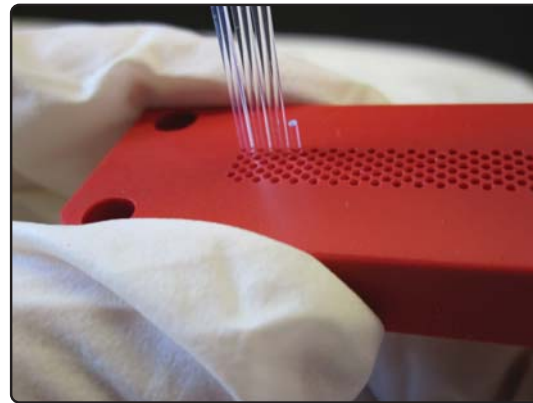
(f) Detail of the fiber bundle polished.

Figure 2.33: Polish phase of the end of the fiber bundle.

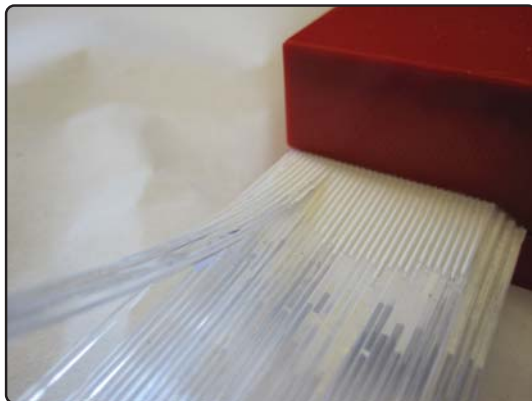
for the bundle length. The fibers are placed one by one in the corresponding hole of the cookie (fig. 2.34b). Since the bundle is made of four layers, is not complicated to identify the fibers consecutively (fig. 2.34c). The position can be checked with the use of light, covering the end of the bundle partially with a slit and observing how the light slit moves at the cookie side. It takes 40 - 50 minutes the entire assembly.



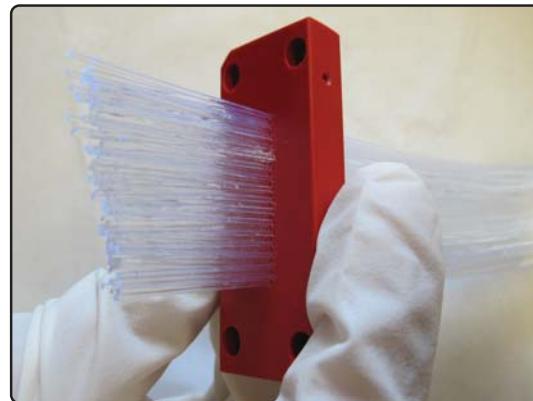
(a) The fiber bundle leveled with the plastic crimping tool.



(b) Allocation of the fibers one by one into the cookie.



(c) Detail of the fiber bundle attached in the crimping tool and how the layers is distinguishable from each other.



(d) The bundle assembled completely into the cookie.

Figure 2.34: Placing of the fibers into the cookie.

2.5.4 Bending of the fiber bundle and gluing to the cookie

With the fibers placed in the cookie, it is attached to the aluminium plate, mentioned before, straight to the bundle or shifted for the bent kind bundle (sec. 2.4.3). The plate with the bundle is placed in an air flow oven at 70°C for one hour (fig. 2.36 left). After cooling the whole set, the plate is placed vertically with the cookie at the bottom. In a flask is prepared a quantity of optical

glue, BC-600 from SAINT-GOBAIN, depending of the number of bundles to be glued. A quantity around 3 - 4 cc by bundle is enough for gluing purposes. The BC-600 is a two compound optical epoxy used normally to glue scintillators blocks with light guides, but since it is not aggressive with the fibers, it shows a good behavior for a vacuum seal and it is enough viscose for a slow flow through the fibers within the holes, making it an ideal choice as glue. It is used in a 3:1 resin-hardener mass proportion. It is applied with the use of syringes (fig. 2.36 right). It allows a more precise application without staining the surface. Enough glue should be applied to allow it flow through the holes of the cookie with the fibers⁵, but keeping some extra glue over the surface of the holes matrix to provide more stability and reinforcement to the fastened fibers. After applying the glue, the bundle is left curing for 24 hours.

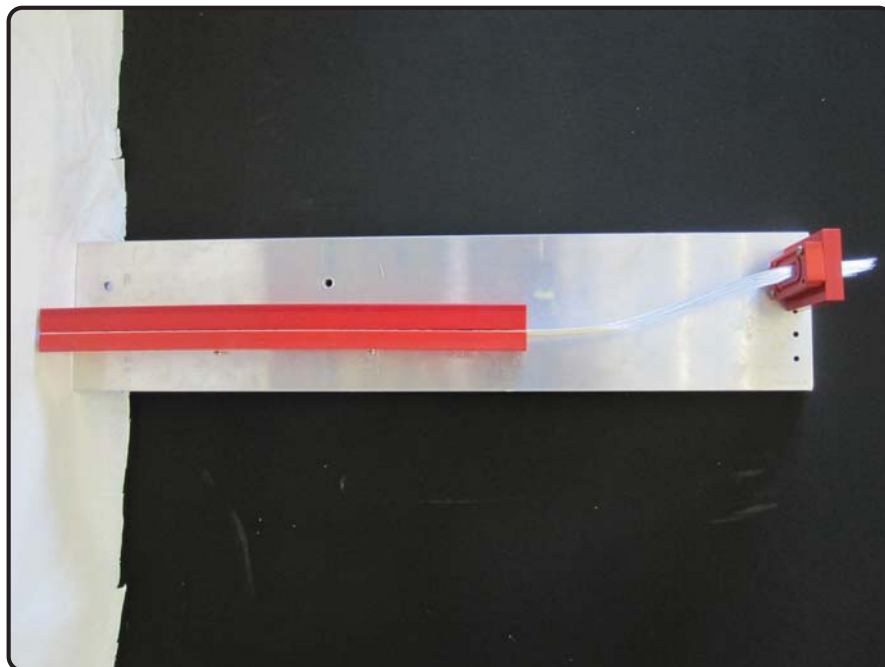


Figure 2.35: Photography of the aluminium plate and the crimping block with the bundle inside prepared to put into the air oven. the cookie (at right) is attached forcing the bent of the bundle. Note that there are some excess of fibers at the end of the cookie that should be removed.

Once the glue is cured, the excess of fibers out of the cookie are cut and the cookie is polished in the same way as explained in sec. 2.5.2. First with the manual diamond saw, then with a rotating sand paper to level the excess and finally with the high precision saw (fig. 2.37). In this case more care is necessary to avoid excess waste of the cookie since the thickness where the fibers are glued is only of 2.5 mm (app. A.1) and on average the high precision saw lowers the material about 0.5 mm.

⁵The fibers are 0.83 mm diameter and the holes through the fibers are placed are 0.9 mm diameter (app. A.1)

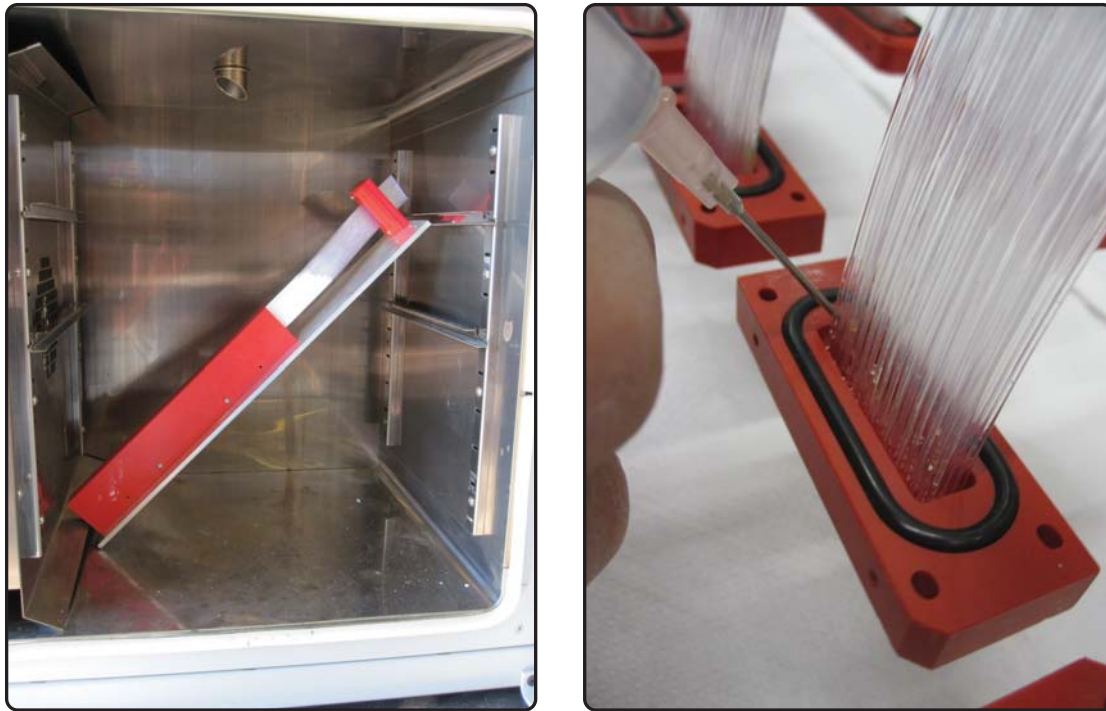


Figure 2.36: Left. Photography of the aluminium plate with the bundle into the air flow oven. The size of the oven allows to place three plates at time. Right. Detail of the application of the glue into the cookie with a syringe. The cookie has an O-ring placed.

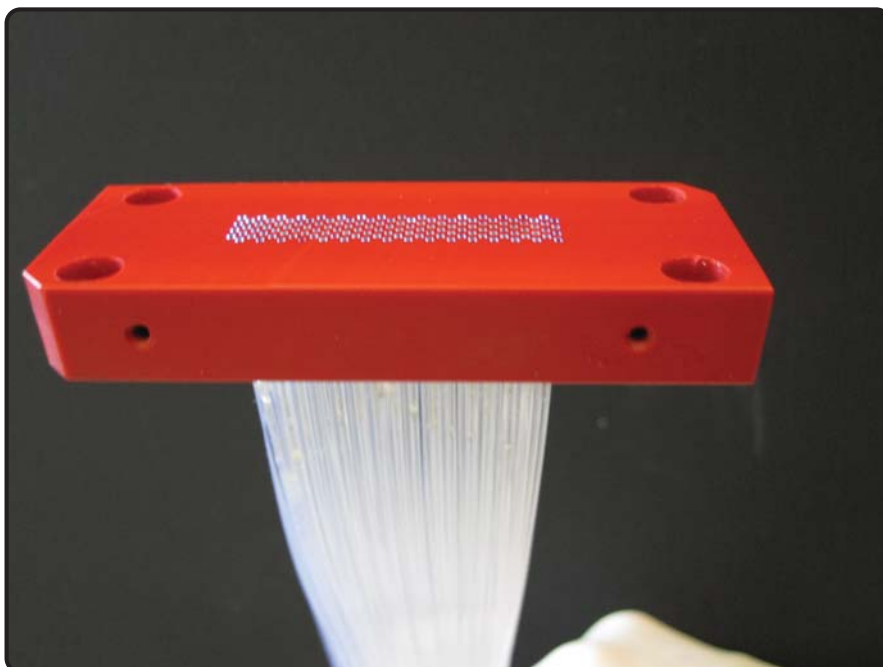


Figure 2.37: Detail of the cookie with fibers after polish.

The bundle is then tested for vacuum leaks in the vacuum workshop of the Institut für Kernphysik of Mainz. In case that the bundle does not pass the test, an extra layer of glue can be applied and then tested again.

2.5.5 Aluminization of the fiber bundles

After the bundles are tested for vacuum, they are covered with plastic, except the end of the fiber, and attached to the aluminium cap and proceed to seal the system. The air pump is switched on and it should be waited until the air pressure inside is in the order of 10^{-2} mbar. Then the jet pump is switched on and when the pressure is in the order of 10^{-5} mbar, the current source is switched on and the amperemeter current is set to get 6 - 8 A. When the pellet is totally melted, the shutter should be open and it should be waited for the deposition of the aluminium vapor occur, watching how it is deposited in the wall of the glass cylinder, normally 3 - 4 seconds after the shutter was opened. After the deposition happens, the current source is switched off. The communication pipe between the compressor and the chamber is closed to avoid oil contamination from the compressor due to the vacuum. Then, the jet pump and the compressor can be turned off, the chamber open and the fiber bundles retired. The whole process takes around 3 - 4 hours.

2.5.6 Alignment of the PMT along the fiber bundle

The PMT is attached to the cookie through two aluminium plates (fig. 2.39 left) which are screwed to the cookie and they fast the PMT from the base with screws (fig. 2.39 right). The pressure of the screws should be enough to fix the PMT keeping it static at the position determined by the alignment, but not too much for a risk of break.

It has been proven that it is possible to align the PMT anodes to the corresponding 4-fiber channel of the cookie [121]. In a black box, the bundle with the PMT is attached to an align tool which allows to move the PMT gently along the channels of the bundle with a level screw. A diode laser illuminates a fiber of a given channel and the energy asymmetry in the neighboring channels is measured. The laser, from HORIBA, produces blue light with pulses in the range of $10^{-12} - 10^{-9}$ s. The focalization and intensity of the laser can be manually adjusted directly in the light source and the pulse rate from the laser control module. The ADC gate is also produced by the laser control module through a NIM output. The laser is focused to one fiber, generally to channel 16, and the the channels 15 and 17 are connected to a LECROY CAMAC Charge ADC 2249A and the DAQ was done with a standard set-up of the A1 collaboration. The output asymmetry A is calculated as:

$$A = \frac{ADC_{17} - ADC_{15}}{ADC_{17} + ADC_{15}} \quad (2.14)$$



(a) Photography of two bundles attached to the cap covered and ready for aluminization.



(b) Photography of the two bundles after the aluminization..

Figure 2.38: Preparation before the aluminization and photography after the process of vaporization.

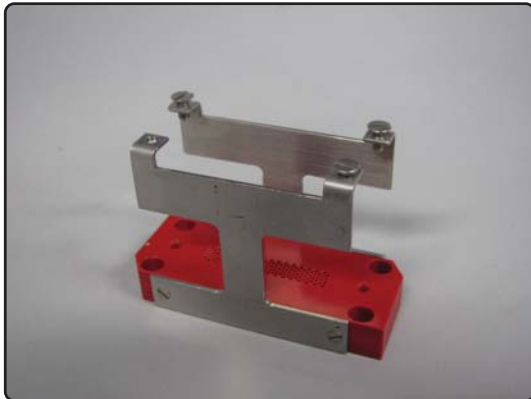


Figure 2.39: Left. Photography of the cookie with the aluminium clamping plates. Right. Detail of the fasten screws at bottom of the PMT base.

with the respective channels ADC_{17} and ADC_{15} corrected to the anode output of the PMT used in the alignment (sec. 2.2.1). A small run is done and from the measurement of the asymmetry, the PMT is moved with the level screw to one side or the other depending of the sign of the result and then the DAQ is done again. When the plot shows an asymmetry <0.01 , the alignment is done.

Figure 2.40 shows a typical output of a aligned module. When the alignment is achieved, the screws at the bottom of the PMT base are fastened and the module is ready (fig. 2.41)

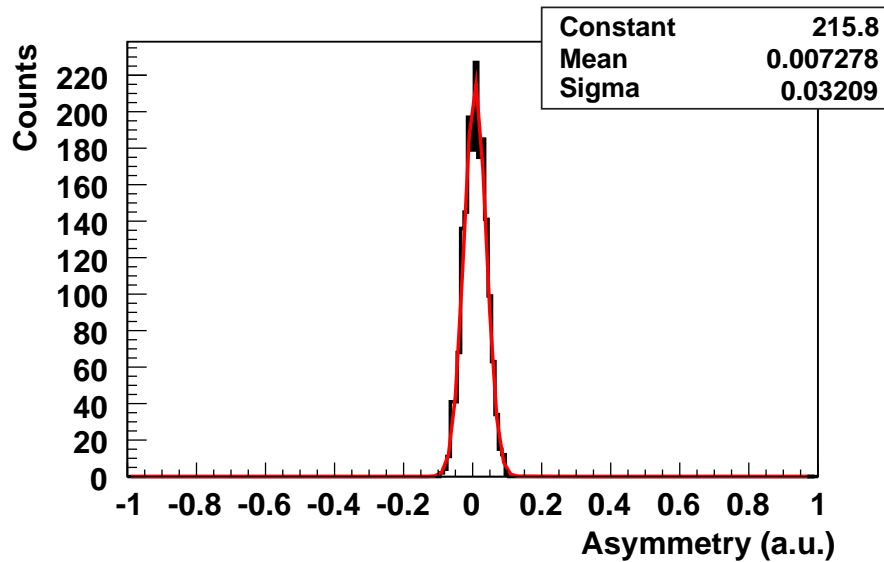


Figure 2.40: Typical asymmetry measurement from an aligned PMT. The red fit is made for orientation purposes. The mean value is zero, showing that the positioning of the fiber respect to the corresponding PMT channel is correct.

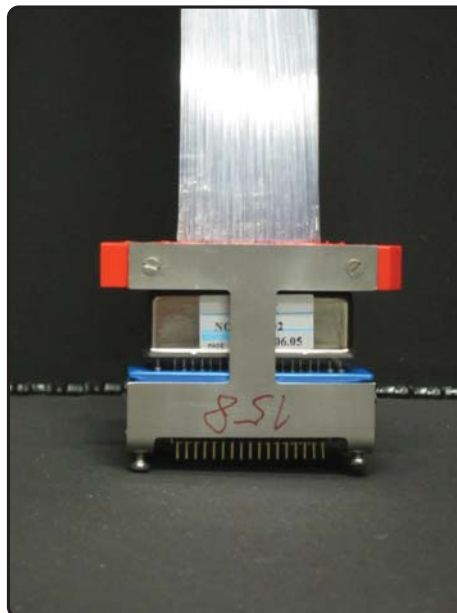


Figure 2.41: Photography of the module assembly and aligned. The PMT is fastened with the screws from the bottom preventing any movement from the desired alignment.

A flowchart of the construction of the modules is presented in fig. 2.42. The time estimated for the construction of one modules is summarized as:

1. Construction of the bundle: 30 m
2. Curing of the constructed bundle: 24 h
3. Polish of the end side of the fiber bundle: 20 m
4. Allocation of the fiber in the cookie: 50 m
5. Heating the bundle in the oven at 70°: 1 h
6. Glueing fiber bundle to the cookie and curing: 24 h
7. Polish of the cookie: 15 m
8. Vacuum test of the glued cookie: 20 m
9. Aluminization of the end side of the fiber bundle: 4 h
10. Alignment of the cookie with the PMT: 1 h

It makes and estimated time of 56.25 h per module. Of course, many modules were made in parallel and the construction tools for the modules do not suffer dead-time during the whole construction time of the modules, *e.g.* new modules could start to build after the 3rd step, reducing the total time for the construction of the whole hodoscope.

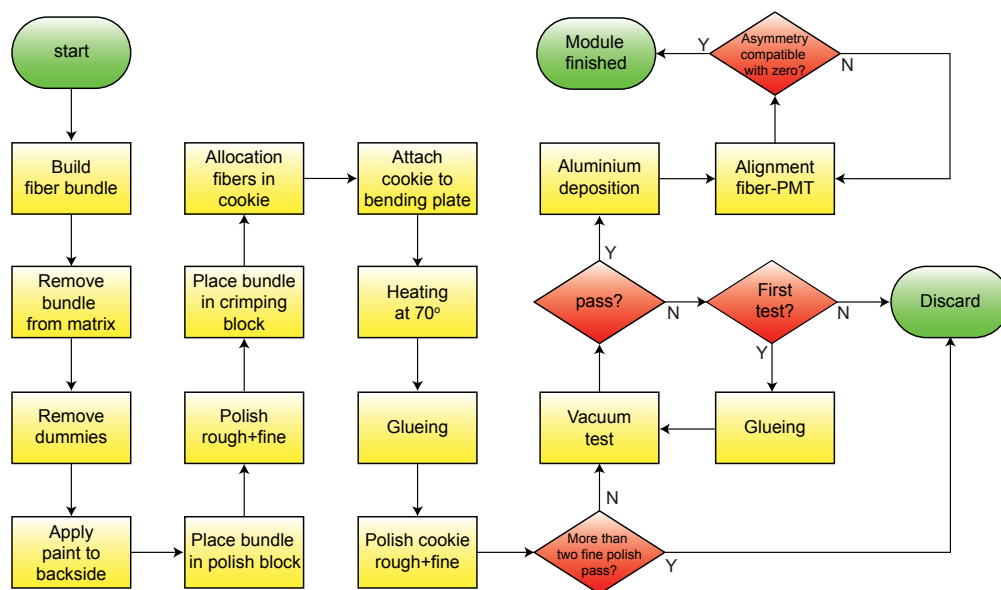


Figure 2.42: Flowchart of the construction of one fiber detector module

2.5.7 Assembly of the fiber hodoscope

As mentioned before, the fiber hodoscope is made of two fiber detectors planes, each one made of 72 fiber bundles + PMT modules. The modules are attached to an aluminium plate of $2180 \times 349 \text{ mm}^2$ and 15 mm thick with orifices of $26 \times 10 \text{ mm}^2$ where the fibers bundle go through (app. A.4). On one side, the modules are attached with screws to the plate, and on the other side there is a groove for an O-ring, for vacuum seal when the plate is attached to the vacuum chamber, and crimping columns to force the bundles in one plane (app. A.4 and fig. A.2).

The bundles are glued together with silicon and fixed with a crimping tool designed for this purpose (fig. 2.45a). The gluing of the bundle should start from the central bundles of the plane and continue to both sides at the time. This is because slight variations on the bundle's width caused by variations in the quantity of the paint used in their assembly, could tilt the bundles losing the verticality and introducing some stress in the direction of the point where the gluing of the plane started. With this procedure, the deviation of verticality and the stress are reduced (fig. 2.43).

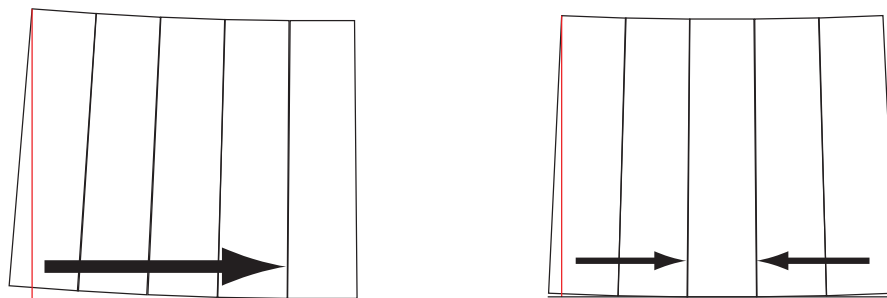


Figure 2.43: Scheme of how the stress and verticality depends on the starting point of gluing. Left. Starting point at one end of the plane. Right. Starting point at center. The different blocks represent the bundles slightly wider at the bottom. The red line shows the vertical and the deviation. The arrows indicates the direction of the stress force against the starting point.

The silicon is applied with a syringe (fig. 2.45b) and is spread with the finger moistened in liquid soap (fig. 2.45c). Five bundles can be glued at the same time and it takes 2-3 days for curing the silicon completely (fig. 2.45d and fig. 2.44). Although the fiber bundles show a perfect compact array, the gap between two neighbor bundles after gluing could be up to the order of 1 mm, providing some kind of inefficiency at the edges of the bundles.



Figure 2.44: Photography of the fiber detector plane assembled in a supporting frame.

2.6 Calibration of the fiber detector

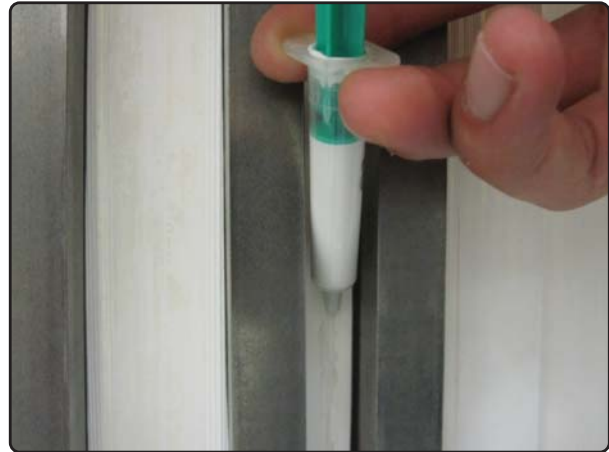
Particle detector must be calibrated in order to know its response to the particle which is to be detected. The fiber hodoscope, whose construction has been explained before, requires two kind of calibrations. One, a spatial calibration of the 4608 channels since the detectors main purpose is the reconstruction of the particle momentum through its spatial coordinate in the focal plane. The second a HV calibration of the MaPMT. Although the HV calibration is a basic step in any optoelectronic device, in this fiber hodoscope the calibration concept is more critical since its calibration cannot be realized for individual channels. So, a compromise of the mean value for the gain of individual channels for a given voltage supply of the PMT is needed.

A flowchart, summarizing the complete process of the calibration, is presented in fig. 2.46. Each calibration step needs a minimum number of measurements per plane. For position calibration 720 measurements/plane are needed. The ADC spectra for each channel requires 2304 measurements/plane and the gain of the MaPMT, 1512 measurements/plane. It takes a total of 9072 measurements to calibrate the whole detector (2 planes). This algorithm presents the handicap that can not be manually done due to the number of events needed in every calibration step and the estimated acquisition rate, 100 Hz. An approximate time schedule for manual calibration can be calculated assuming that from measurement to measurement it takes 5 min to set-up.

- 720 measurements \times 2000 events (positioning)
- 2304 measurements \times 10000 events (ADC spectra)
- 1512 measurements \times 10000 events (MaPMT gain)



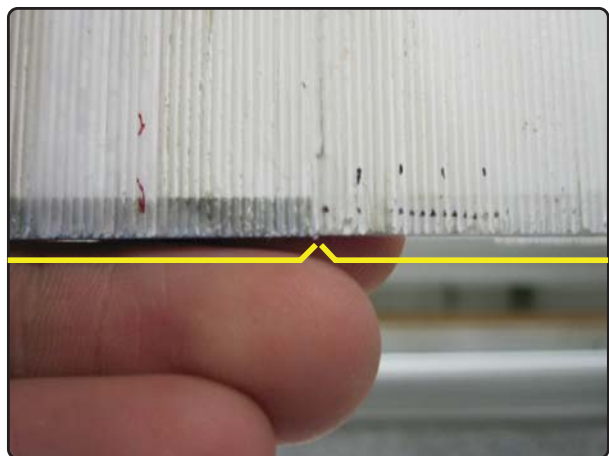
(a) Fiber bundles in the plane with crimping tools ready for glue.



(b) Application of the silicon for glue between the bundles with a syringe.



(c) Spread of the silicon layer applied in order to form a tiny layer.



(d) Detail of the union between two bundles after curing. The yellow line indicates the two bundles.

Figure 2.45: Photographs of the gluing of the bundles to make the focal plane.

making a total of 39.6×10^6 events, with a estimated rate of 100 Hz, 3.96×10^5 s.

With the time between measurements,

$$(720 + 2304 + 1512 \text{ measurements}) \times 300 \text{ s} = 1.3608 \times 10^6 \text{ s}$$

makes a total of 487.2 h continuous running. Since in this calculations, it is assumed that the process is made manually, a more realistic time schedule can be estimated. It can be assumed a normal work time of 6 h/day ($1/4$ day) and 5 work days/week. Therefore, it comprises

$$487.2 \text{ h} \times \frac{1 \text{ day}}{24 \text{ h}} \times \frac{4 \text{ work-day}}{1 \text{ day}} \times \frac{1 \text{ week}}{5 \text{ work-days}} = 16.24 \text{ weeks/plane}$$

If the time between measurements is not considered, that was assumed for manual set-up, the calibration time is reduced to 4.6 days of continuous data acquisition. This could be slightly longer due to mechanical issues.

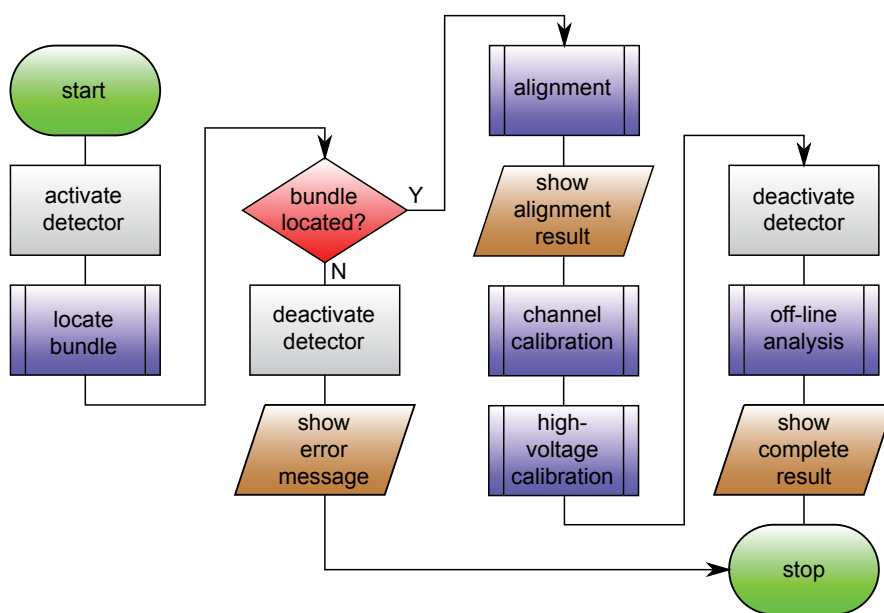


Figure 2.46: Flowchart of the position and gain calibration of the fiber hodoscope. Figure from [122].

All these time calculations were done considering optimum conditions for the measurements. In practice, it was not considered also, that the manual calibration implies the total human presence during the process, which implies high human time consumption untapped. It is clear that manual calibration process is hard and a long working time consumption makes a full automatization of the whole process mandatory. This automatization of the calibration process of the fiber detector planes was designed and made in collaboration with A. Esser, M. Biroth and P. Gülker [122].

2.6.1 Position calibration

The fiber plane, placed on a supporting frame, is placed in a black box with a plate where a radioactive source and the DAQ are arranged. The set-up is placed over a movable carriage over rails which is positioned alongside the detector plane by a stepping motor with a precision of 0.1 mm. A collimated ^{90}Sr -source with a beam diameter of 1 mm is arranged in an acrylic glass block. On the opposite side a narrow trigger detector which consists of a stack of scintillating fibers insures that the electrons have crossed the fiber detector. This trigger detector has a size of $20 \times 0.5 \times 20 \text{ mm}^3$ and is read out by a conventional PMT. A schematic of the calibration setup can be seen in fig. 2.47. In order to obtain only minimum ionizing particles inside the fiber detector, the discriminator threshold of the trigger detector was chosen to be as high as possible.

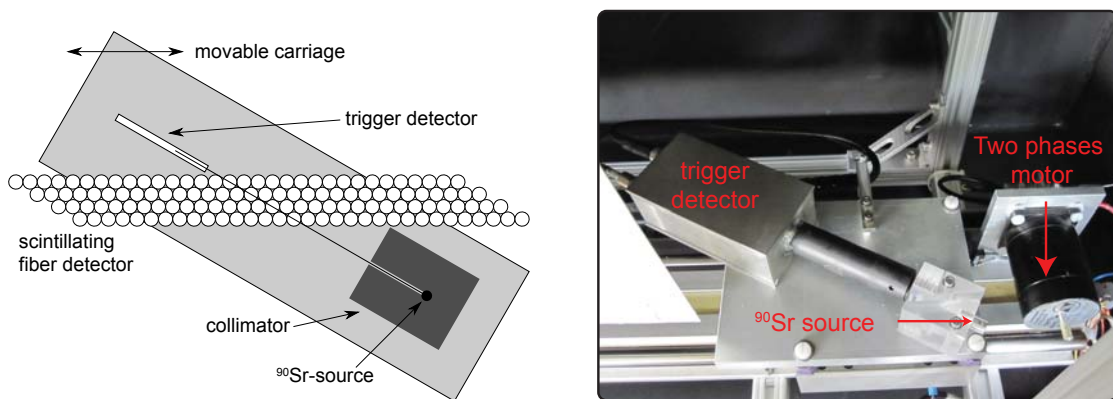


Figure 2.47: Left. Scheme of the calibration set-up. The collimated β -source and a trigger detector are mounted on a common carriage for automatic positioning alongside the fiber plane. Figure from [122]. Right. Photography of the calibration set-up in the black box. The two phase motor is used to move the carriage alongside the fiber plane.

The calibration software localizes one fiber bundle by moving the carriage to its approximate position and takes a test measurement to determine its initial position. From here, the carriage with the source is moved in front of the bundle, at 10 equidistant positions between the channel 6 and 24. For every position a data set of 2 000 events was acquired. From every event, the obtained cluster is analyzed to get the hit position. These clusters are caused by particles hitting scintillating fibers of multiple channels as well as optical cross-talk between neighboring channels. The hit position is calculated as the mean channel of the cluster, for each event, where all channels are weighted with their ADC value:

$$\bar{x} = \frac{\sum_{ch=0}^{32} ADC_{ch} \times ch}{\sum_{ch=0}^{32} ADC_{ch}} \quad (2.15)$$

This allows one, to achieve a position resolution less than the channel width, *i.e.* fiber diameter. The hit position for all events are represented in a histogram for a position distribution (fig. 2.48 left) for every carriage position. The analysis of every position distribution permits one, to obtain a correlation between the fiber channels and the carriage position which provides the calibration (fig. 2.48 right).

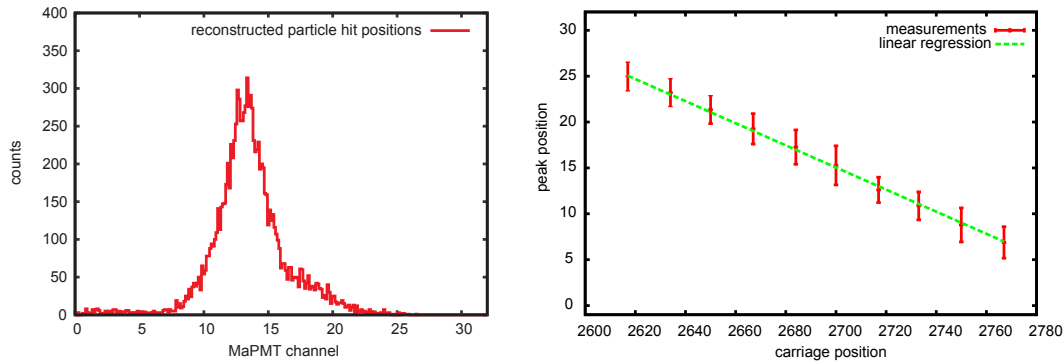


Figure 2.48: Left. Typical hit position distribution for a calibration carriage position at channel 13. One channel correspond to a fiber diameter, *i.e.* 0.83 mm. The tail of the distribution between channels 16 and 22 is caused by the tilted channel arrangement producing a higher probability for particles to be scattered into the trigger detector from the higher channel side. Right. Plot of the calculated position of the source in the fiber channel versus the corresponding carriage position, for a given bundle and linear fit of the distribution. Figure from [122].

The obtained positions of the individual bundles of scintillating fibers is used to reconstruct the hit position in the analysis of the data from the coordinate detector in real operation. From the individual fit of every bundle, the relative deviations of channel positions with respect to a linear arrangement is calculated from the coordinate at the origin of the linear fit. The relative deviations of the channel positions of all channels is shown in fig. 2.49. An important point of this calibration is that it corrects the offsets in the assembly between modules of the whole fiber detector plane (sec. 2.5.7).

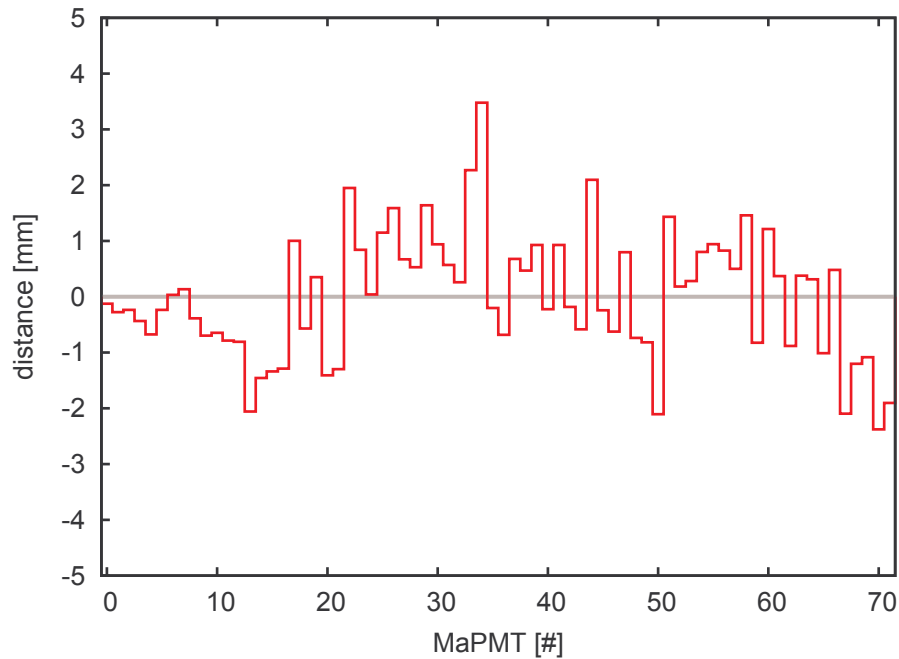


Figure 2.49: Deviations of the channel positions for all 72 modules of one fiber detector plane with respect to a linear channel arrangement. This data is used for correcting the channel positions in the coordinate detector data analysis. Figure from [122].

2.6.2 MaPMT gain measurement and HV calibration

Once the position of a fiber bundle has been measured, the individual gain of every channel is determined. For this, with the calibration previously determined, a set of 10000 events is taken for every channel of the fiber bundle at a fixed voltage of 900 V. In this case, to achieve a good energy resolution, it is necessary to assure that the entries in the ADC spectrum correspond to particles which have crossed the measured channel. Therefore, only events with hit positions in the range of the channel of interest contribute to the spectrum (fig. 2.50). The energy resolution achieved with this method is of the order of $\Delta E/E \approx 0.6$, for an accuracy of these measurements of the order of 1%.

For all 2304 channels of one plane, large gain variations of the order of 40% can be observed among individual MaPMTs and smaller variations of the order of 10% between channels of one MaPMT (fig. 2.51). From the data sheet, the gain uniformity among anodes is typically 1:15 (1:17 is the mean value of all PMTs from the data sheet purchased, table 2.2) with the edges having slightly lower gains on average (fig. 2.7). However the gain values specified in the data sheet do not correspond to the measured values, since the measurement also includes the optical properties of each channel.

With the gain measured for all modules, the high voltages can be adjusted to correct the gain variations among the modules. The high voltages are adjusted so that the ADC values for the channels with the highest gain

of every module are equal. This is made measuring the signal height of the two channels with the highest gain and the channel with the lowest gain for each MaPMT with 7 different high-voltages in the range of 600 V to 1000 V and adjusting the resulting measurements through a polynomial fit. Figure 2.52 shows the plot of all adjusted fits of the signal height as a function of the high-voltage for all PMTs of one fiber detector plane. The signal height changes as the 4.5th power of the high-voltage, although the data sheet of the H7259K indicates that is proportional to the 9th power. However, the last was measured as the ratio between the anode current and the photocathode current, while the calibration procedure measures the charge integrated single anode pulses.

Figure 2.53 shows the effect of this adjustment. Variations between different channels for a given module are compensated by setting individual discriminator thresholds for every 4 channels (sec. 2.3.1).

2.7 Fiber detector set-up

Since the fiber detector hodoscope consists in two planes of 24 triple boards (sec. 2.2.2) per plane, for a total of 144 modules, every module is identified in an unique form. The planes are called X and Θ , each triple board is numbered from 1 to 24 and every module of each triple board is named A, B and C. So a given module is labeled as $\langle \text{plane} \rangle - \langle 1-24 \rangle - \langle \text{ABC} \rangle$. The electronics crates are located behind the hadron arm detectors protected with a boron composite wall which reduce the radiation (figure). The RJ-45 cables which connect the triple boards with the DTD are 10 m long. Again, due to the high number of cables, $144 \text{ module} \times 8 \text{ cables per modules} = 1152 \text{ cables}$, a correct labeling is important to avoid transposition of the read-out channel. The cables are labeled with the number of the triple board, the name of the module and the number of the cable 1 to 8, i.e. $\langle 1-24 \rangle - \langle \text{ABC} \rangle - \langle 1-8 \rangle$ (fig. 2.54).

The cables are connected to the DTD sequentially from top to bottom. The crates allow to allocate 21 DTD modules and one crate controller. A total of 7 crates are necessary for the complete hodoscope. The DTD distributes its output signal among the TDC and the VUPROM modules. The signal to the TDC-CMC is conducted through a standard twisted flat cable of 3 m long with 68 pin Robinson-Nungent connectors. As mentioned before (sec. 2.3.2), four TDC-CMC are allocated in a CATCH module. For the whole hodoscope, 36 CATCH modules are necessary. A 9U VME-crate can allocate 16 CATCH modules with the corresponding Central Process Unit (CPU) controller, making a total of 3 crates. To the VUPROM modules, the signal is conducted through handmade cables with VHDCI connectors of 3.5 m long. Although the number of inputs of the VUPROM should be equal to the number of fiber modules, since the configuration of each module could be configured depending of their use (sec. 2.3.3), the number VUPROM modules depends on the trigger design (sec. 4.1). The first stage of the trigger design uses 12 modules with a 6 inputs and 2 outputs configuration, making 12 modules per plane for a total of 24 modules. The VUPROM modules are allocated in a 6U VME-crate which allows to place 18 modules with a dedicated VME CPU and a remote reset card. Figure 2.55 shows a scheme of the connection of a single fiber module. Figures 2.56a, 2.56b, 2.56c, 2.56d show different details of the fiber detector hodoscope placed in KAOS spectrometer. The DAQ and slow control of the detector is done with the standard software of the A1 collaboration, Mezzo for slow control and Aqua++ for data acquisition [123].

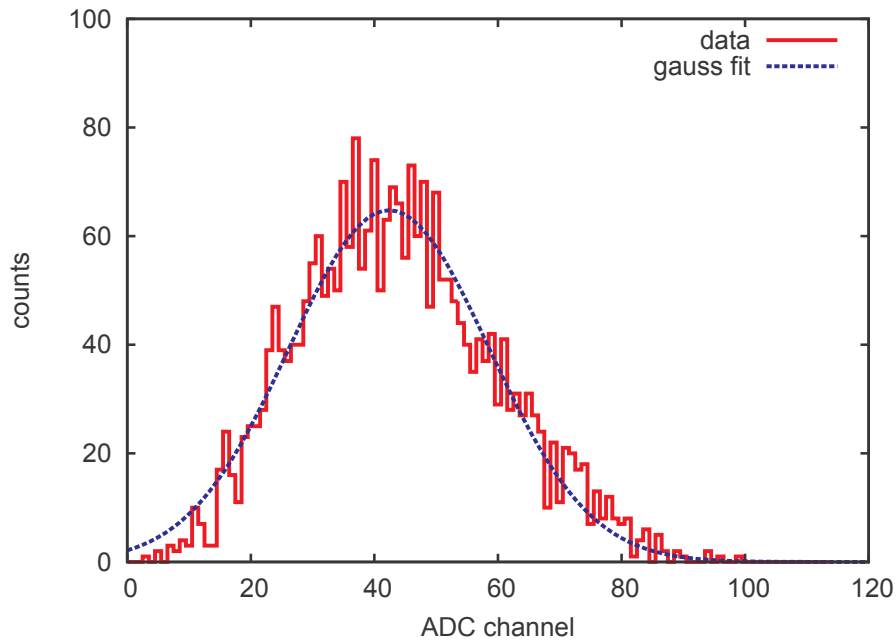


Figure 2.50: Typical ADC distribution for signal height measurement of one channel. The relative energy distribution is $\Delta E/E \approx 0.6$ leading to an accuracy in the measurement of $\sim 1\%$. Figure from [122].

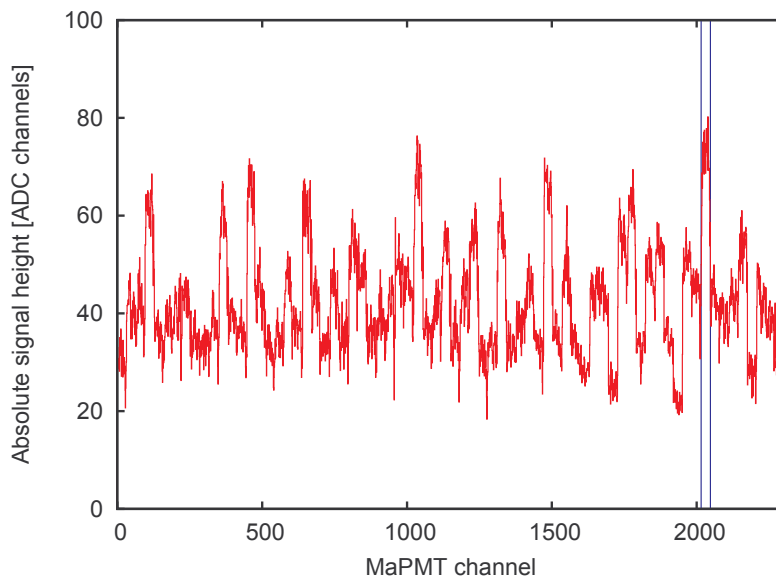


Figure 2.51: Measured signal heights for the 2304 channels of one detector plane. The vertical blue lines indicate the size of one MaPMT. Large variation between different modules as well smaller variations between the channels of one MaPMT can be seen. Figure from [122].

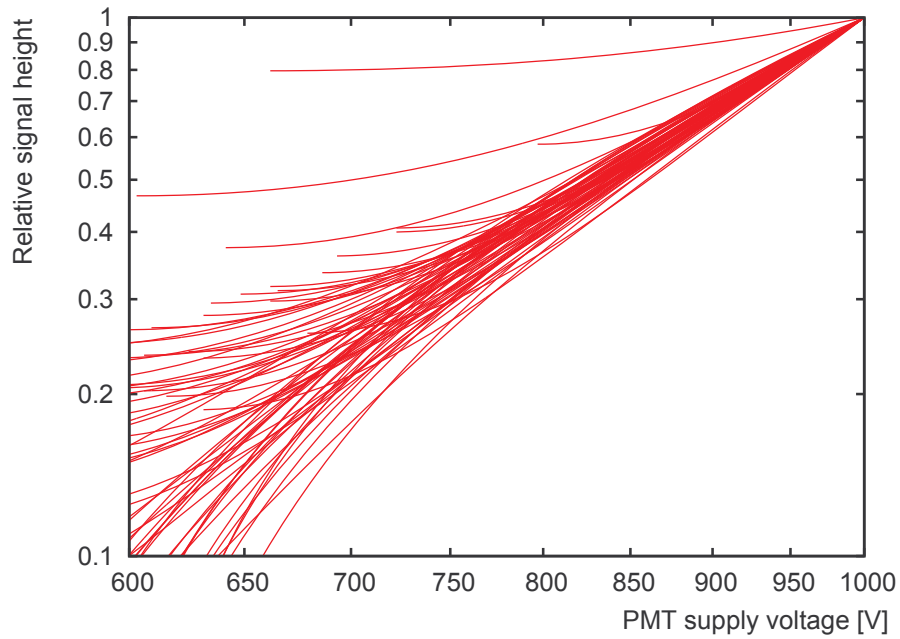


Figure 2.52: Relative signal height as a function of the applied high-voltage for the 72 MaPMTs of one fiber detector plane. Figure from [122].

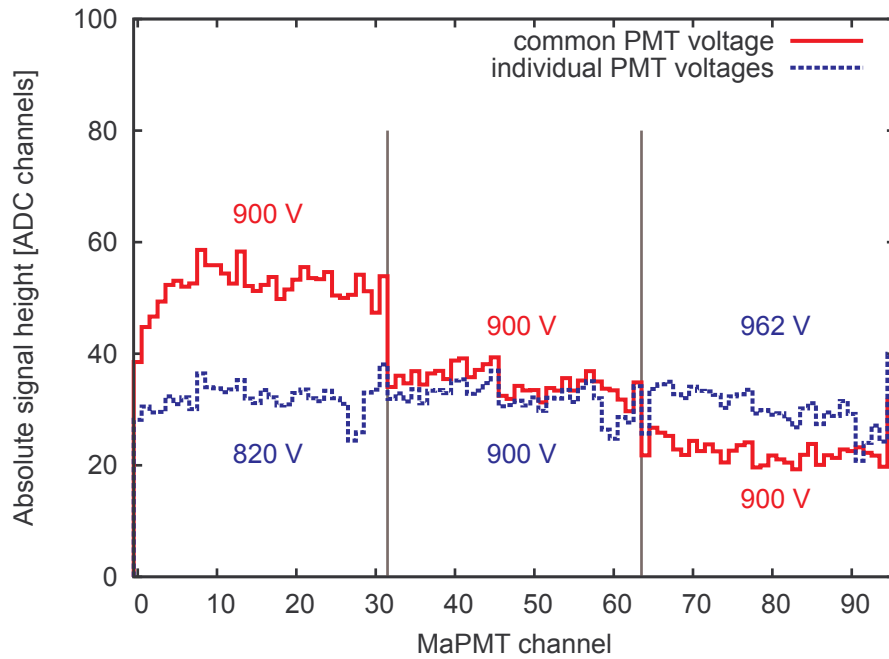


Figure 2.53: Measured signal heights of three neighboring modules, 96 channels. The solid red line shows the signal height with the MaPMT operated at 900 V. The dashed blue line, the signal height after the adjustment. The high voltages are adjusted in a way that the ADC values of the channels with the highest gain of each MaPMT are equal. Figure from [122].

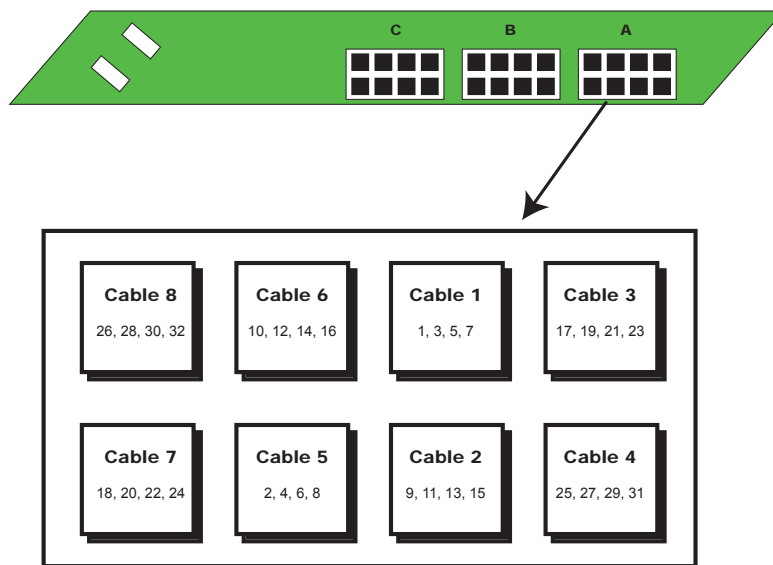


Figure 2.54: Scheme of how to connect the RJ-45 cables in the triple board and name of the modules in one triple board. The scheme of the triple board in the up side helps to locate the orientation for the correct connection of the cables. Each cable carries the signal of four PMT channels, but not in sequence. This connection sequence helps to debugging the channel map in the analysis software.

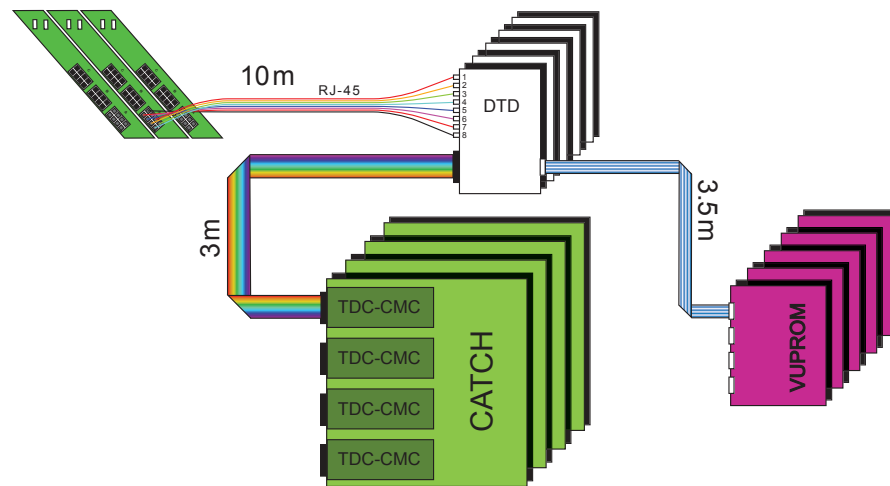


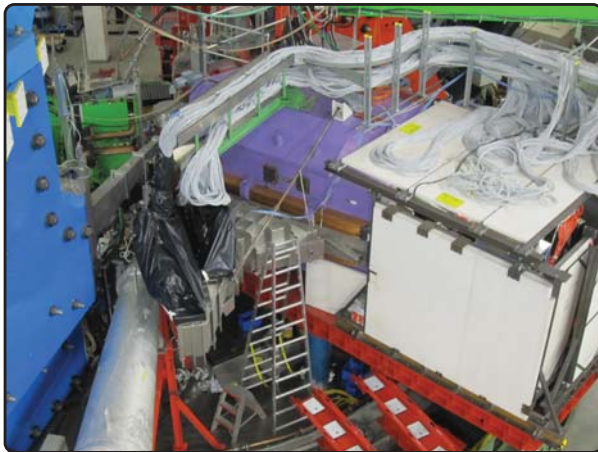
Figure 2.55: Scheme of the connection of a single module, not at scale. The signal from the MaPMT is sent to the DTD through 8 RJ-45 cables. The RJ-45 cables are colored to differentiate them easily. The DTD modules are in a 6U-VME crate and are controlled by a controller module (not in the scheme) which is handled by parallel port (sec. 2.3.1). The output from the discriminator is sent to the TDC-CMC by the front connector through standard flat cable with Robinson-Nungent connectors. The CATCH modules are placed in 9U-VME crates, each crate controlled by a dedicated VME CPU. The output of the TDC-CMC through the CATCH interface is sent to the readout buffer PC (sec. 2.3.2). The signal from the backside of the DTD goes to the VUPROM through handmade cables with VHDCI connectors. The VUPROM modules are placed in 6U-VME crates, each crate controlled by a dedicated VME CPU (sec. 2.3.3). The VUPROM process the signal to provide the trigger of the electron arm (sec. 4.1).



(a) Photography of one detector plane in the vacuum chamber without the cables.



(b) Photography in detail of the triple boards with the signal cables already placed and the flat cables between the triple boards to power and control the HV bases of the MaPMT. The long blue flat cable is the main power and control cable from the HVSyS512 module



(c) General view of the KAOS spectrometer with fiber detector hodoscope installed (covered with black plastic). The hadron arm instrumentation is placed inside the radiation protection white walls at right.



(d) Photography of the front-end electronics of the fiber detector hodoscope.

Figure 2.56: Photographs of the cabling of the fiber detector in KAOS.

Beam tests at GSI

The fiber detector modules built before the fiber detector hodoscope, were tested under different conditions at GSI. Different layouts of the fiber bundle were tested, as their theoretical space resolution is quite similar. [118]

3.1 Performance test at GSI with carbon beam

A set-up with three bundles of 0° layout (sec. 2.4.1.1) in a ^{12}C beam of 2 AGeV [124] was tested in GSI Cave C.

Two of the bundles were aligned in one plane and the third one was placed in parallel to the other two and in front of them, as is shown in fig. 3.1 and fig. 3.2 left.

As the standard set-up was designed to extract energy information from the detector in only two channels of the multiplexed connectors at a time (sec. 2.3.1), a piggyback board was designed to be attached to the DTD (fig. 3.2 right). The analog signal from the piggyback board was read by two CAMAC ADCs Model 2249A from LECROY. The trigger was provided by a scintillator paddle 2 m upstream in the beam line.

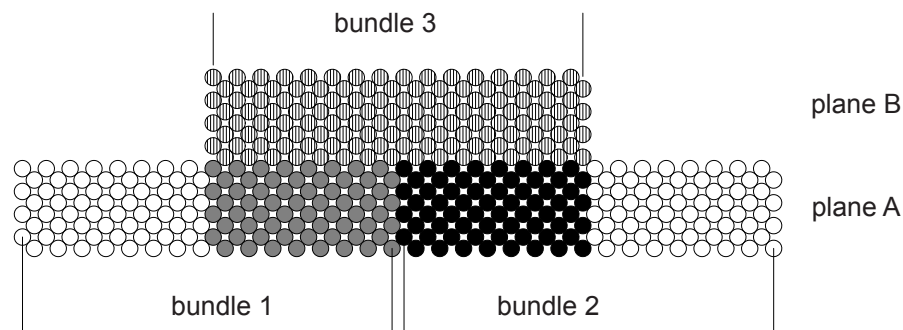


Figure 3.1: Layout of the three fiber bundles forming two detection planes. The 256 shaded or filled fibers were read out via 64 MaPMT channels (32 per plane).

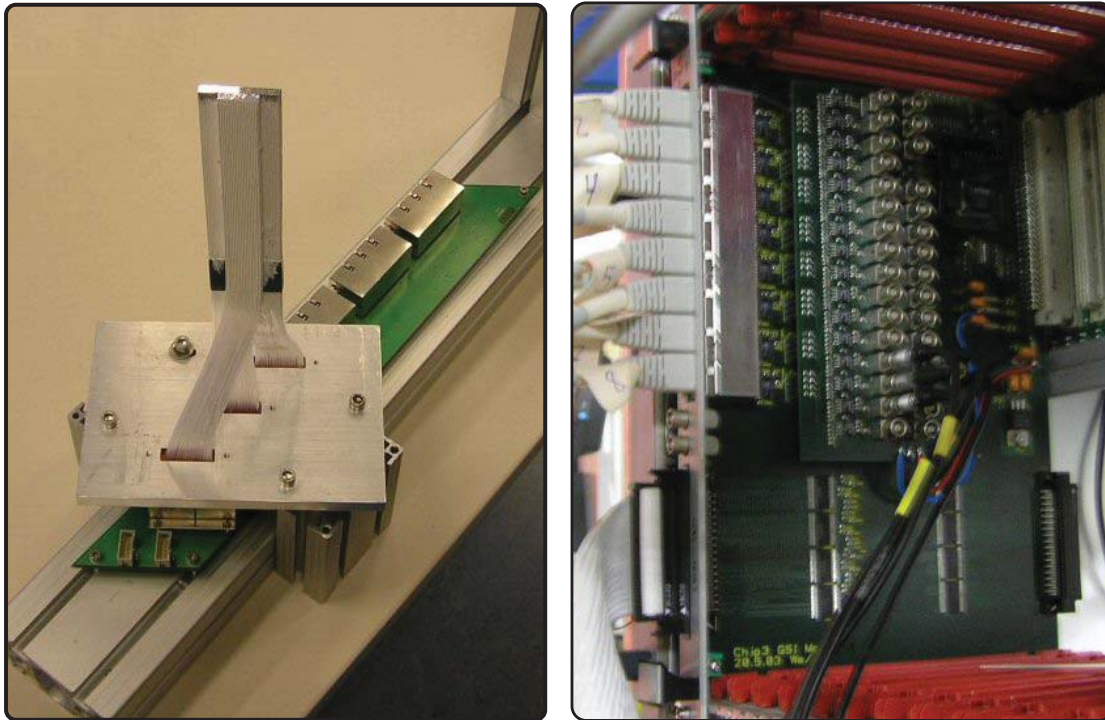


Figure 3.2: Left. Photograph of the fiber detector used in the ^{12}C beam at GSI over a MAYTEC profile. The triple board used was one of the first versions. Right. Photograph of the piggyback board for analog signal output, attached to the DTD. It has 32 50Ω connectors, one per MaPMT channel.

The time resolution was obtained making iterations over all hits in a plane including multiple hits in a channel, in order to search for clusters of correlated hit times.

The cluster with the time closest to the trigger signal was retained, and within the cluster, the time of the first received signal was chosen as the hit time. The algorithm was implemented to request a minimum time separation of 10 ns between clusters and a hit in a coincidence window of 20 ns width. Since the time resolution was obtained from the difference between the two hit times in the two planes of fibers, $t_A - t_B$, no walk-correction was needed because the DTD suppressed it (sec. 2.3.1.1).

The residual time was distributed with a width of $t_{FWHM} = 330$ ps (fig.3.3) and without any significant dependence on the PMT high voltage. The time resolution of a single fiber plane was derived to be $\Delta t_{FWHM} \sim t_{FWHM}/\sqrt{2} = 230$ ps.

The pulse height spectra were fitted for different high voltages in order to get the normalization, A_i , and the pedestal position, p_i , for each ADC channel i . After the calibration, the spectra were corrected for channel-to-channel gain variations. 11 neighbouring channels in one plane, and the same number in the plane directly behind it, were available for pulse height information.

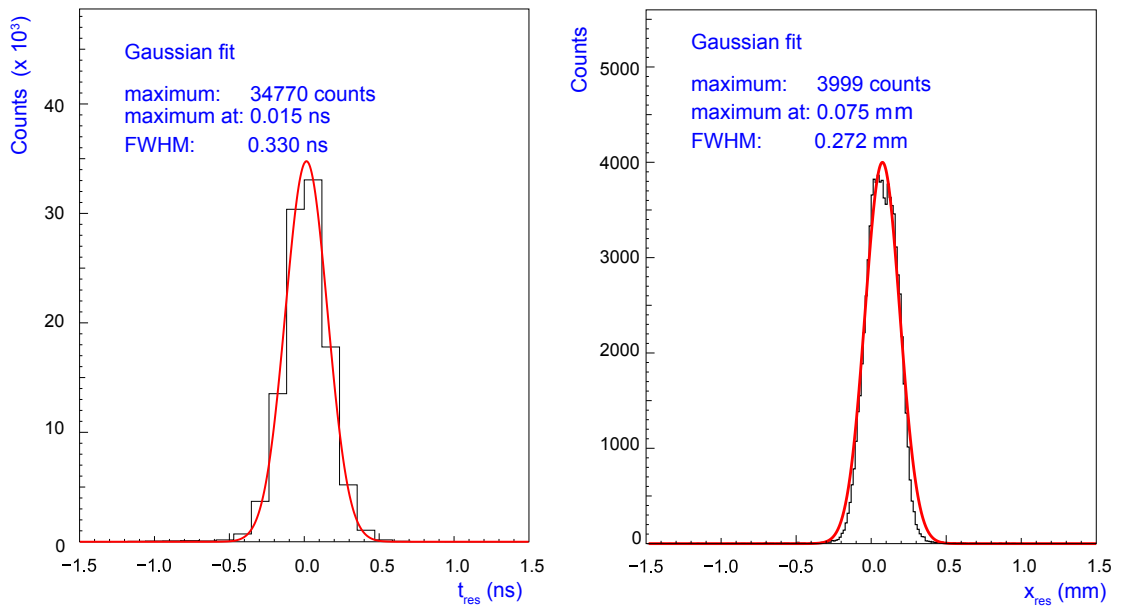


Figure 3.3: Left. The residual of hit times between two detector planes, $t_A - t_B$. A Gaussian fit is shown providing a width of $t_{FWHM} = 330$ ps. The time resolution of a single detector plane was determined to be $\Delta t_{FWHM} \sim t_{FWHM}/\sqrt{2} = 230$ ps. Right. The residual of track position estimates between both detector planes, $x_A - x_B$, using the centroid of charges. A Gaussian fit is shown providing a width of FWHM = 0.27 mm, however, the distribution is non-Gaussian with two overlapping peaks because of the discretisation in fiber channels. Figures from [118].

The hit channel was determined by the pulse height maximum. ?? shows the correlation between the centroids of charges in both detector planes. The step structure was a consequence of the discretisation in fiber channels as it can be seen that the pitch between each step was $\Delta c_A, \Delta c_B \approx 0.6$ mm, which was the pitch of the read-out columns of the 0° fiber detector.

The residual of the hit position, defined as the difference between the two track position estimates in the two planes of fibers $x_A - x_B$, was measured with a FWHM = 272 μm (fig. 3.3 right). This accuracy was sufficient for the unique identification of the hit channel, which led to a spatial accuracy of $0.6 \text{ mm}/\sqrt{12} \approx 170 \mu\text{m}$ (rms).

The channel with the pulse height maximum was strongly correlated to the hit time channel (fig. 3.4), as was defined before, showing that the ADC calibration and TDC offsets values had been correctly determined.

Since the fiber detector will be used without any analog read-out, it was interesting to estimate the spatial accuracy with the hit time channel information. Since the absolute position of the particle tracks was not known, the hit channel mean value was compared with the estimated position from the ADC information, which was assumed to be more accurate.

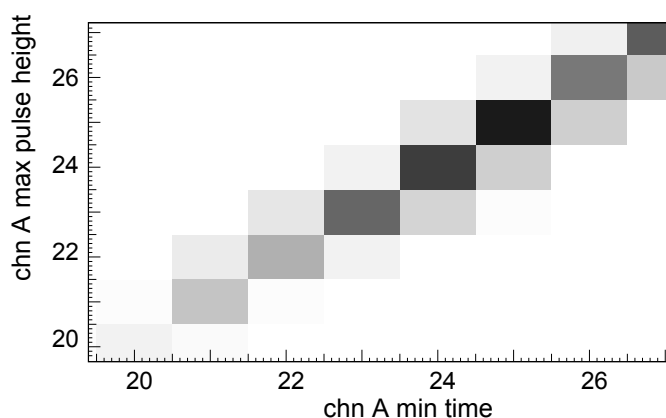


Figure 3.4: Gray-scale plot showing the strong correlation between the hit time defining channel and the channel of maximum pulse height in detector plane A. Figure from [124].

The difference between the hit channel mean value (as simple estimator of the track position) and the reconstructed position, was calculated requiring a minimum ADC value, around 70% of the maximum, to simulate a given discriminator threshold.

This difference included the contribution from the uncertainties in position estimators and the granularity of the fiber array. The measured distributions were characterized by $\langle \text{FWHM} \rangle \sim 0.6 \text{ mm}$ (approx. the fiber pitch), $\langle \text{RMS} \rangle = 0.5 \text{ mm}$, and $\langle \text{FWTM} \rangle < 1 \text{ mm}$.

The detection efficiency of a plane, defined as the probability to find at least one hit in one plane when the other plane provide a hit, was above 99%.

3.2 Performance test at GSI with different particle species beam

Another fiber detector in a $p/\pi^+/d$ beam of 3.3 Tm magnetic rigidity with dominant protons of 1 GeV/c momentum and ^{12}C beam of 2 AGeV energy [125] was tested in GSI Cave A. As was done with the test in Cave C (sec. 3.1), the set-up consisted in three fiber bundles, two of those bundles forming a plane, called plane A, and a third bundle placed behind them, plane B, although for this test, a 60° fiber layout geometry (fig 3.5) was used. The bundles were aligned in such a way that the columns were parallel to the beam direction. The trigger was derived from plane B and a DAQ that was similar to the previous test was used

The residuum from the hit time was measured with a width of 720 ps for the beam of different particles (fig. 3.6 left) and 510 ps for the ^{12}C beam. This derives a time resolution for individual fiber modules of $720/\sqrt{2} = 510 \text{ ps}$ and $310/\sqrt{2} = 220 \text{ ps}$ respectively.

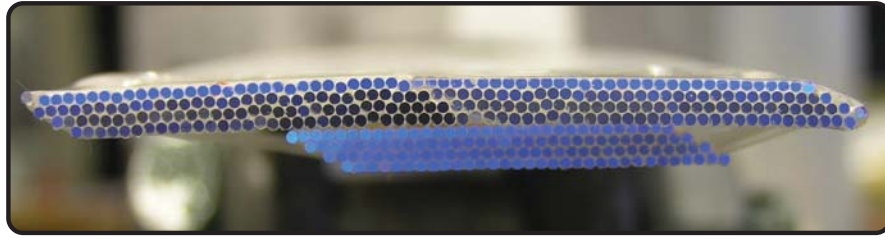


Figure 3.5: Photograph of the arrangement of the fiber bundles for the test in the Cave A of the GSI.

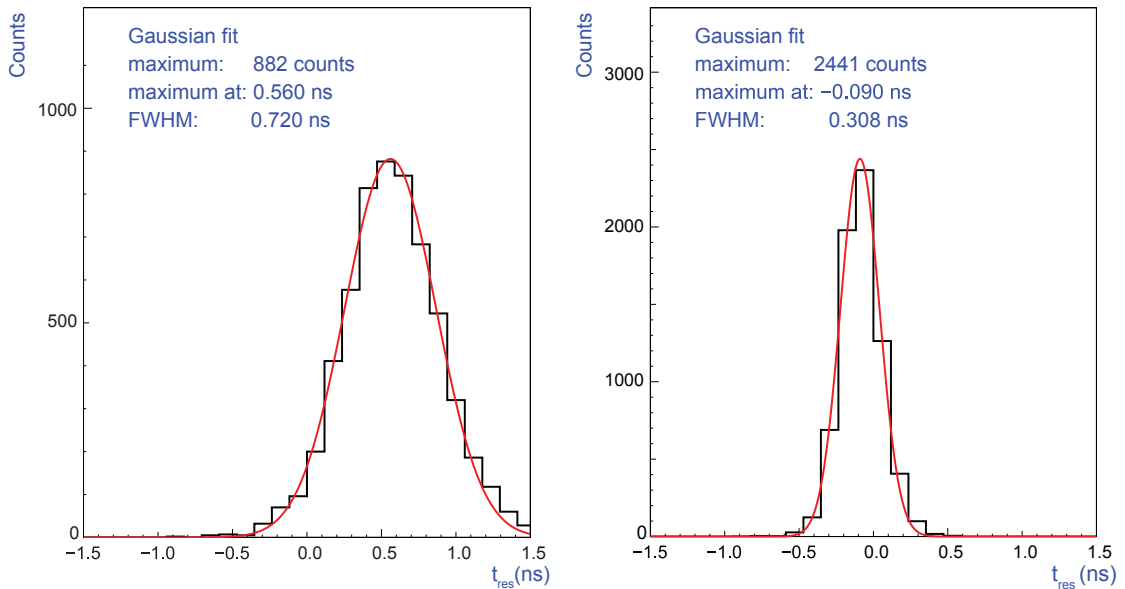


Figure 3.6: Left. The residual of hit times between two detector planes, $t_A - t_B$. A Gaussian fit is shown providing a width of $t_{FWHM} = 720$ ps. The time resolution of a single detector plane was derived to be $\Delta t_{FWHM} \sim t_{FWHM}/\sqrt{2} = 510$ ps [118]. Right. The residual of hit times from ^{12}C beam. The $t_{FWHM} = 310$ ps for an single fiber module time resolution of 220 ps. Figures from [125].

The multiplicity distributions of both planes showed an average maximum at $N \sim 5$ channels (fig. 3.7). These values were the consequence of small misalignments of the PMT with the fibers and mainly cross-talk in the glass window of the MaPMT.

By using the pulse height information the hit channel was determined as the centroid of charges. The residuum of the hit position defined as the difference between the two estimates in the planes, shows a width of $FWHM \sim 460 \mu\text{m}$ (fig. 3.8 left). This resolution could be improved considering the gain variations between different channels.

By using the pulse height information, the hit channel was determined as the centroid of charges. The residuum of the hit position, defined as the difference between the two estimates in the planes, showed a width of $FWHM \sim$

460 μm (fig. 3.8 left). This resolution could have been improved considering the gain variations between different channels.

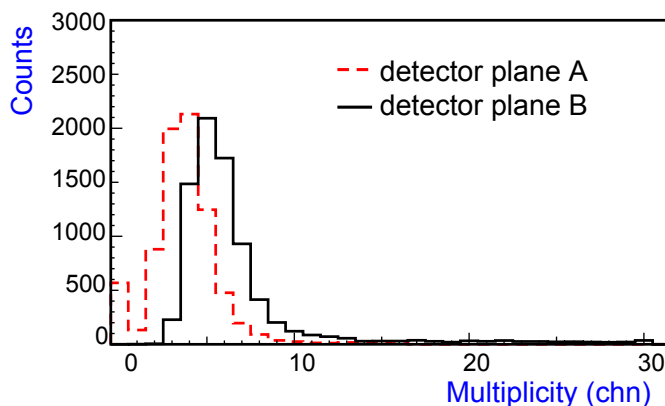


Figure 3.7: Multiplicity distribution of the two planes of the fiber detector showing a maximum of $N \sim 5$ channels on both planes.

From the distribution of the pulse height sum over all channels of plane B for the cocktail beam, a Gaussian fit showed a relative variation in the energy deposition of $\Delta E/E \sim 60\%$ (fig. 3.8 right).

3.3 Conclusions from the performance tests

The beam test performed with the different bundles layouts had provided some important conclusions.

All tests have shown a similar multiplicity although they were aligned with the beam. This multiplicity has been associated with optical cross-talk, secondary electrons and the misalignment of the PMT with the fibers in the cookie. The cross-talk is intrinsic in the MaPMT and the secondaries are products of the interaction of the beam with the materials which one cannot do much about it without an analog read-out, which was not implemented for the fiber hodoscope.

The misalignment is an issue that can be improved by mechanical ways (sec. 2.5.6). A perfect alignment helps to reduce the optical cross-talk, but never below 3 channels for an ideal hit of one channel of the bundle.

Even so the fiber detector has shown a good performance with an excellent time resolution of $\Delta t \sim 220$ ps with a ^{12}C beam and a spatial resolution of $\Delta x \sim 460\mu\text{m}$. It makes the scintillator fiber detector suitable as a focal plane detector and trigger for the hypernuclear experiments with KAOS.

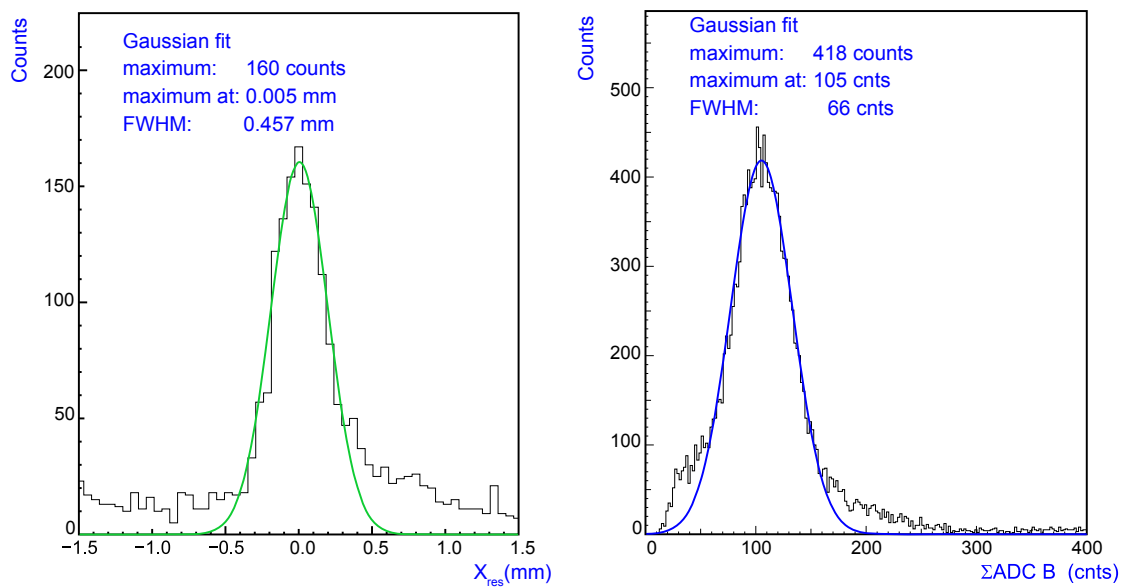


Figure 3.8: Left. Residual distribution of the track position estimates between both planes using the centroid, for the cocktail beam. The Gaussian fit shows a $\Delta x_{FWHM} \sim 460 \mu\text{m}$. Right. Distribution of the pulse height sum over all channels of plane B for the cocktail beam. From the Gaussian fit a relative energy resolution $\Delta E/E \sim 60\%$ can be deduced. Figures from [125].

Electron-Arm Spectrometry

Two test beams were used to characterize the fiber hodoscope under beam conditions. One, in 2009 [126], for trigger performance and for background studies, using a 585 MeV beam energy; another one, in 2010, to obtain calibration data for the Monte-Carlo studies to extract the optics parameters of the detector in KAOS using a 510 MeV beam energy for the coincidence between both fiber planes. Both tests were made using a 130 mg/cm^2 polyethylene CH_2 target.

4.1 Fiber detector trigger

The trigger concept was designed by A. Esser [127, 126]. It was developed with enough flexibility to allow in-beam tests of the electron arm and for hypernuclei electro-production experiments.

For in-beam tests, the trigger system was based on a fast clustering algorithm to define the hit position and thus the charged particle track. Also a hit multiplicity cut helped to reject spurious hits. It was programmed to minimize accidental triggering rates and to reject background events that do not come from the spectrometer *i.e.* the desired reaction products from the target.

In hypernuclei electro-production experiments, the trigger also includes the correlation between the momentum of the particles in the focal plane of the spectrometers. This sensitivity to the kinematics allows one to select a given missing mass range by the trigger. The temporal correlation between hits is used to identify and reject pile-up and to select specific particles via time of flight measurement.

The trigger is obtained through the VUPROM modules, described in sec. 2.3.3. In order to satisfy the requirements of the trigger, a total of 37 modules are needed. A scheme of the trigger implementation is shown in fig. 4.1.

In the first stage (fig. 4.3a) the information is processed from all fiber modules through the DTD, for which 72 VHDCI inputs per plane are needed

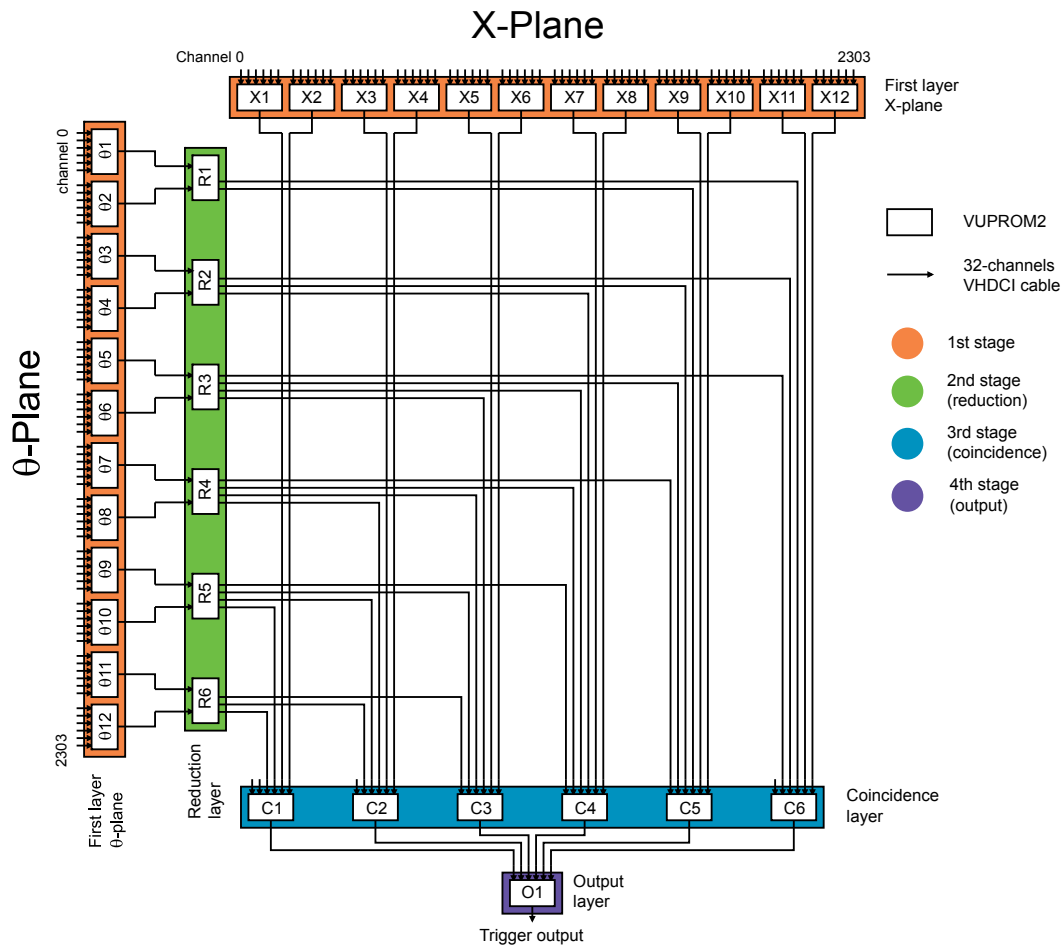


Figure 4.1: Trigger scheme used during the beam-test of the electron-arm detectors. Each white box represents a VUPROM module; colored areas represent the four different stages of the trigger logic; arrows indicate 32-channel VHDCI cables. Each fiber plane has its own first layer and Θ -plane reduction layer. The coincidence and output layers combine the signals from the two planes. A total of 37 modules are needed to satisfy the requirements on the trigger. Figure from [126].

in this stage. In practice, the first stage involves 12 VUPROM modules with 6 VHDCI inputs per plane. Each module in this stage provides two outputs, one to transmit information to the next stage and one used for debugging. In this stage there are two logic units. A 6:1 reduction unit, which serves as a gate for all channels and a cluster finder unit, since a particle hit always causes a cluster of correlated signals in the neighboring channels due to the geometry.

Clusters are identified reading the signals in n neighboring channels and request absence of signal in the next lower and higher channels within a given time period. Figure 4.2 shows the scheme of the logic unit.

A Pulse-Width Discriminator (PWD) is used in order to discard short pulses which are the result of different delays in the input signals. It divides the signal in two, one of them delayed with respect to the other. Then the signals are connected to an AND gate. Only signals with a length greater than the delay, produce an output signal. Clusters with large sizes are discarded to reduce the background from scattered particles which cross the fiber detector planes with large angles with respect to the normal on the detector plane. On the other hand, extremely small clusters are produced by noise. The size of the clusters can be set online through the VME bus and can be adapted depending of the experimental conditions.

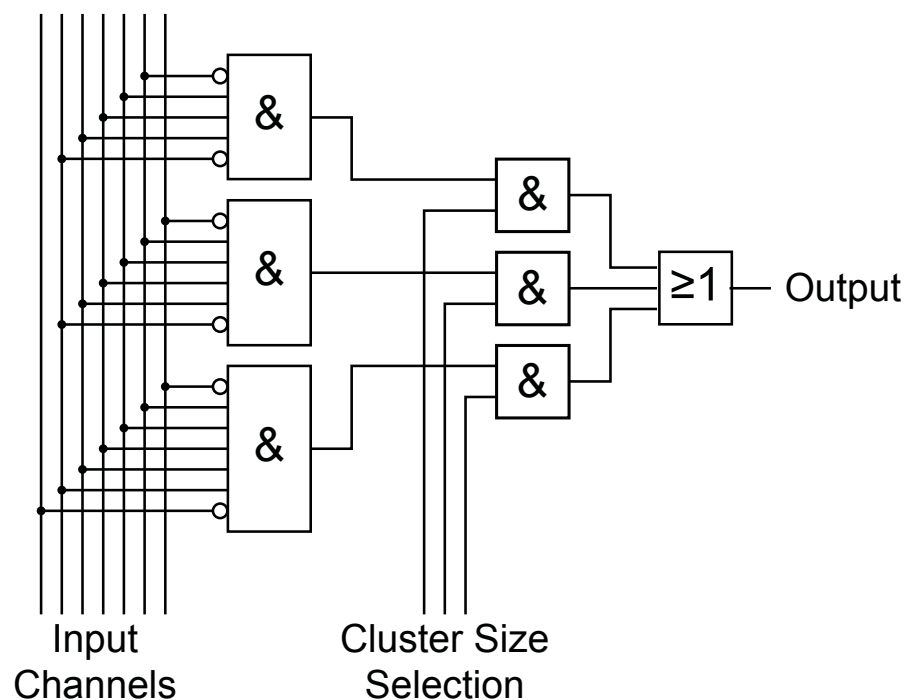


Figure 4.2: Scheme of the logic unit used for finding clusters of a size $n=3$ to 5..

The input signal is connected to AND gates, so that an output signal is only produced when a given signal size is found. The upper and lower neighboring channels are connected in negative to obtain a cluster of the desired size. Figure from [126]

The second stage (fig. 4.3b) is used only after the first stage of the \ominus -plane. Its purpose is to reduce the number of channels by a factor 2 executing an OR between neighboring channels and providing the signal information on several outputs in parallel.

The information from the X -plane and the \ominus -plane is combined in the third stage (fig. 4.3c). It consists of five different logic units, in parallel, combined with a multiplexer to choose the logic of the output. Those five logic units are: one 6:1 reduction unit, with a similar function as the one on the first stage. One unit to check temporal coincidences between the X and \ominus -planes. One 2:1 reduction unit for an OR output for the channels from the X -plane. One reduction unit of 4:1 is implemented for the \ominus -plane. The fifth logic unit consists of a coincidence matrix in order to perform an acceptance test for the reconstructed tracks when a hit correlation between both planes is required. The accepted combinations of hit positions in both planes are stored in a binary matrix externally calculated. An output is produced when a cluster is produced and the corresponding matrix element is nonzero. In this stage, each VUPROM handles a range of 384 channels of the X -plane and up to 1536 channels of the \ominus -plane. This setup was chosen to cover the angular acceptance known from simulations with the highest granularity.

The output consists of a single VUPROM module that receives the information of accepted trajectories from the coincidence stage and produces the output signal. Two logic units in parallel are implemented. One is a coincidence unit between accepted signals of the X - and \ominus -planes, the other is an OR gate. Due to the complexity of the four stages, each one has a different latency. The first stage has 68 ns latency, the reduction stage 22 ns, the coincidence stage has 23 - 30 ns depending on the selected trigger and the output stage has 30 ns. The through-put time for raw signals is 104 ns, the generation of an X AND \ominus trigger needs 143 ns and additional tracking conditions require extra 7 ns. There is no event-by-event variation of the latencies and a time jitter of ± 1.5 ns occurs in each stage, producing a total jitter of ± 3 ns.

4.1.1 Trigger Control System

The function of the Trigger Control System (TCS) is to distribute the trigger source and time reference to the CATCH modules from a single source, as the output stage explained before. The TCS is based on the COMPASS system [128] using a laser module and passive optical splitters. The main component of the trigger distribution is the TCS controller, a 6U VME module, that is triggered by a First Level Trigger (FLT) from the VUPROM system (sec. 4.1). The system is completed with one time and trigger control laser crate that operates at 155.52 MHz, two layers of optical 32-channel splitters and a total of 37 TCS receivers. The receivers decode the trigger and deliver it to the CATCH modules housed in the same VME crate (sec. 2.3.2).

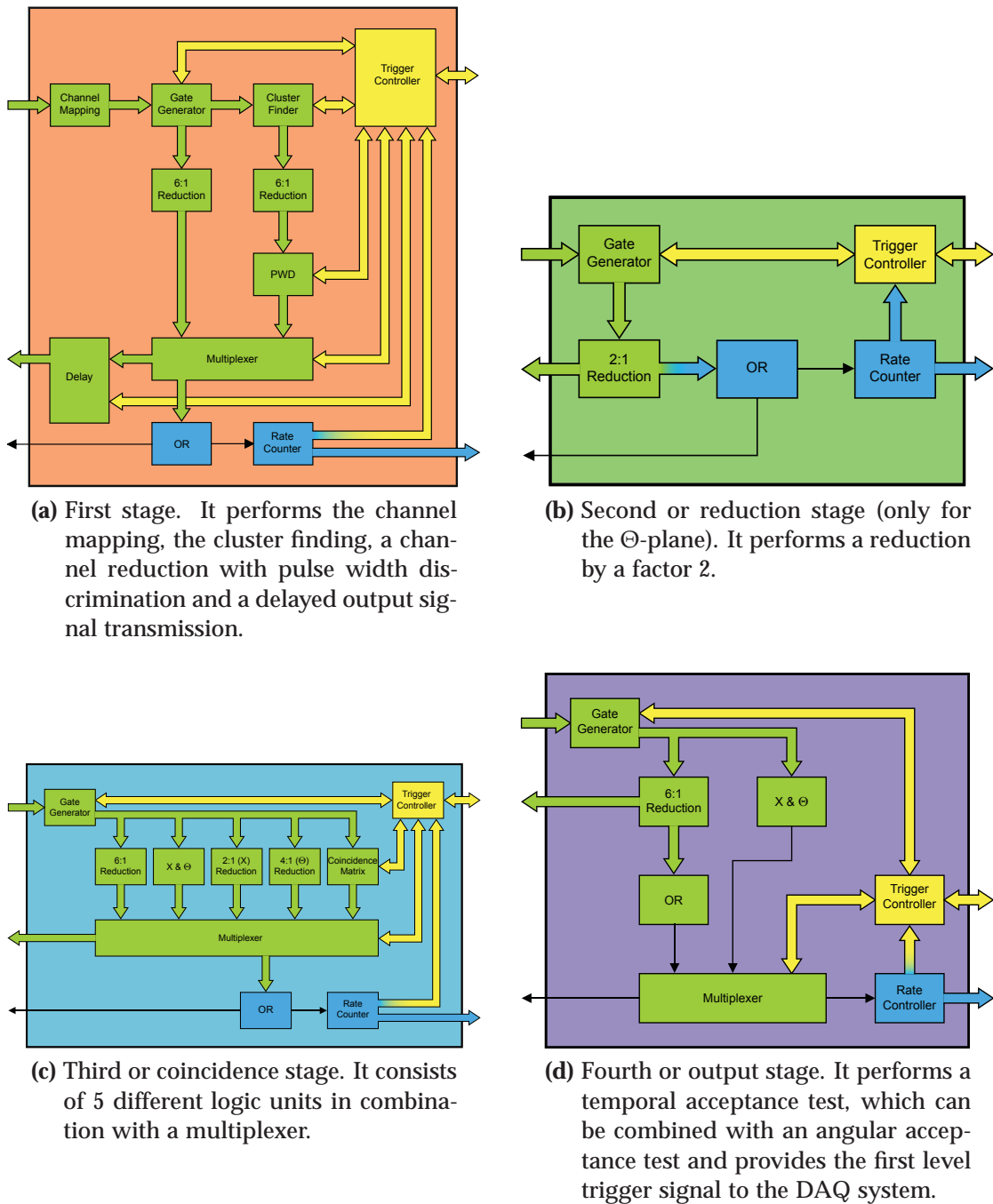


Figure 4.3: Composition of the different stages of the trigger system. Each color corresponds to the color stage in fig. 4.1. Each box represents one functional unit. Basic logic signals are represented as thin arrows and parallel signals as thick ones. The color code reflects the main purpose of the unit: green colored units and signals are part of trigger signal processing, yellow colored components are part of the trigger control, and debug or monitoring components are colored in blue. Figures from [126].

4.2 In-beam tests at MAMI

In the 2009 beamtime, 51 PMT for the X -plane (1632 channels) and 21 PMT for the Θ -plane (672 channels) were tested all consecutively and in the center area of the planes.

For an energy of MAMI of $E_e = 585$ MeV, the kinematic parameters for a $p(e,e'p)$ reaction, with electrons detected at KAOS, $\theta_{e'} = 39^\circ$, and protons in Spectrometer B, both with respect to the beam direction, are:

$$\begin{aligned} E_{e'} &= 313.1 \text{ MeV} \\ \theta_p &= 60.1^\circ \\ |\mathbf{p}_{p'}| &= 372 \text{ MeV}/c \end{aligned}$$

On the other hand, in the 2010 beamtime, the X -plane was completely assembled and connected, while only some modules were available for the Θ -plane and not consecutively, making two detection regions in Θ -plane.

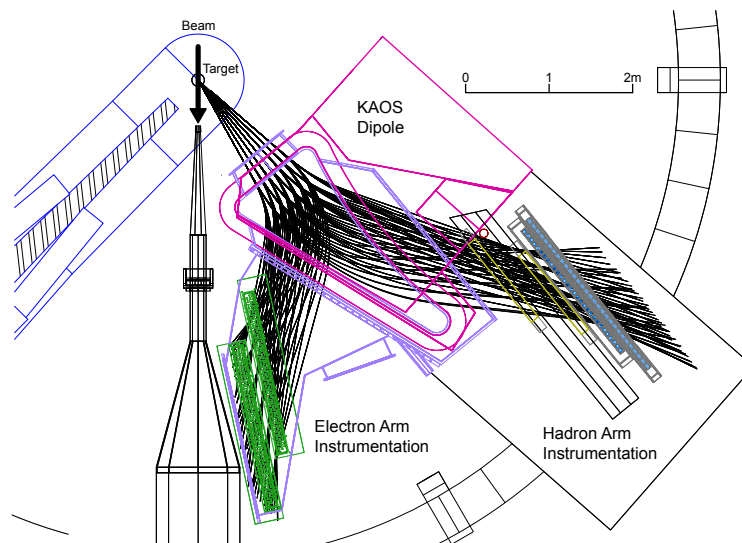


Figure 4.4: CAD drawing of the KAOS double-arm spectrometer setup as used for the in-beam testing of its read-out and trigger electronics during 2009 and 2010. Positive and negatively charged particles through the spectrometer are shown by full lines from target to detection planes. The position of the electron-arm detector and front-end boards is indicated by the green color, its angle to the target is approx. $8\text{--}10^\circ$. In this setup the fringe field from the dipole coil deflects low momentum particles directly scattered into the direction of the electron-arm detector.

With an energy of MAMI of $E_e = 510$ MeV, the kinematic parameters for a $p(e,e'p)$ reaction, with protons detected at KAOS, $\theta_p = 37.5^\circ$, are:

$$\begin{aligned}\theta_{e'} &= 80.3^\circ \\ E_{e'} &= 351.0 \text{ MeV} \\ |\mathbf{p}_p| &= 567 \text{ MeV}/c\end{aligned}$$

Due to the emission angle of the scattered electron, it was detected with Spectrometer C (sec. 1.2.1.1). The use of protons instead of electrons helps to characterize the fiber detector better since electrons produce more secondary radiation when they interact with materials and they can be also significantly altered in direction.

4.2.1 Background sources and trigger signal filtering

The place where the fiber planes are located make them sensitive to a huge amount of secondary products from the beam interaction with the target. One of the predominant background sources are electrons from Bremsstrahlung. At extreme relativistic energies, both, the photon and the outgoing electron, tend to proceed in the same direction as the incident electron [129] with an emission angle of the order of a few milli-radians [130].

In the test beam of 2009 and 2010, this source of background is not relevant since the fiber detector is completely out of the region of interaction of Bremsstrahlung electrons (the outer fiber plane is located between 8° and 10° as can be seen in fig. 4.4). For electroproduction experiments at 0° , this consideration is more critical, but in a similar way as the experiment E01-011 in JLab (sec. ??), the cone of Bremsstrahlung electrons is by avoided making the fiber detector with a height shorter than the distance to the dispersive plane (sec. 2.4.3) and the possibility to change the height of KAOS respect to the target (sec. 1.2.2).

Another important source of background is from Møller scattering¹. Electrons from Møller scattering have a wider spread than Bremsstrahlung, depending on the electron beam energy. The energy of the scattered electrons is calculated with the equations [131]:

$$\begin{aligned}E &= E_0 \cos^2 \frac{1}{2}\theta_{cm} \\ \theta_{cm} &= 2 \arctan \left(\left(\frac{1}{2} \left(\frac{E_0}{m_e} + 1 \right) \right)^{1/2} \tan \theta \right)\end{aligned}$$

where θ_{cm} is the angle in the center of mass system, θ the angle in the laboratory system, E the energy of the scattered electron and E_0 the energy of the electron beam.

Again, in the beam tests of 2009 and 2010, with the fiber detector placed between 8° and 10° with respect to the beam direction, the energy of the Møller

¹Scattering of electrons by electrons

scattered electron is between 40-50 MeV (fig. 4.5), so most of the electrons were deflected in the fringe field of the dipole or scattered in the vacuum chamber walls (fig. 4.4).

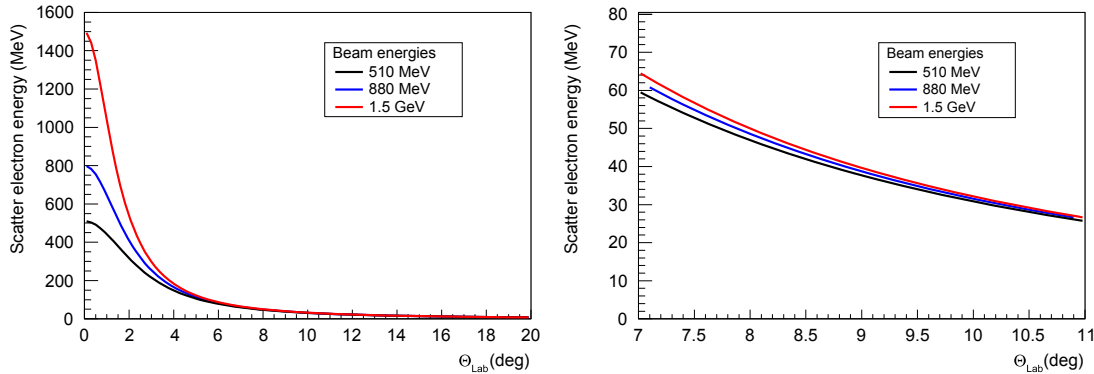


Figure 4.5: Left. Plot of scattered Møller electron energy vs laboratory scattering angle, for 510, 880 and 1500 MeV electron beam energies. Right. Zoom of the region of interest for the fiber detector. The energy of the scattered electron is practically independent of the beam energy at higher scattering angles.

With a beam at 0° in experiments for electroproduction of strangeness, the high energetic Møller scattering electron can be avoided because the design of the fiber bundle as was explained before, but it is still a high source of background as can be seen in the Møller production cross section in fig. 4.6 calculated from the Møller production cross section in lab system [132]:

$$\left(\frac{d\sigma}{d\Omega}\right)_{Lab} = r_0^2 \left(\frac{4(\gamma+1)}{\beta^2\gamma}\right)^2 \frac{\cos\theta}{(2+(\gamma-1)\sin^2\theta)^2} \left(4y^4 - 3y^2 + \left(\frac{\gamma-1}{2\gamma}\right)(1+4y^2)\right) \quad (4.1)$$

where:

$$\begin{aligned} r_0 &= \frac{e^2}{m_e c^2} = 2.818 \text{ fm}; \text{ classical electron radius} \\ \gamma &= (1-\beta)^{-1/2} = \frac{E_{beam}}{m_e} \\ y &= \csc\theta_{cm} \\ \sin\theta_{cm} &= \frac{((2(\gamma+1))^{1/2} \sin 2\theta)}{2+(\gamma-1)\sin^2\theta} \end{aligned}$$

Elastic/quasi-elastic scattering at target elements (C and H in this case) and coherent scattering (from C nuclei) are also background sources. Varying the current of the MAMI electron beam, the raw signal rates in the X-plane

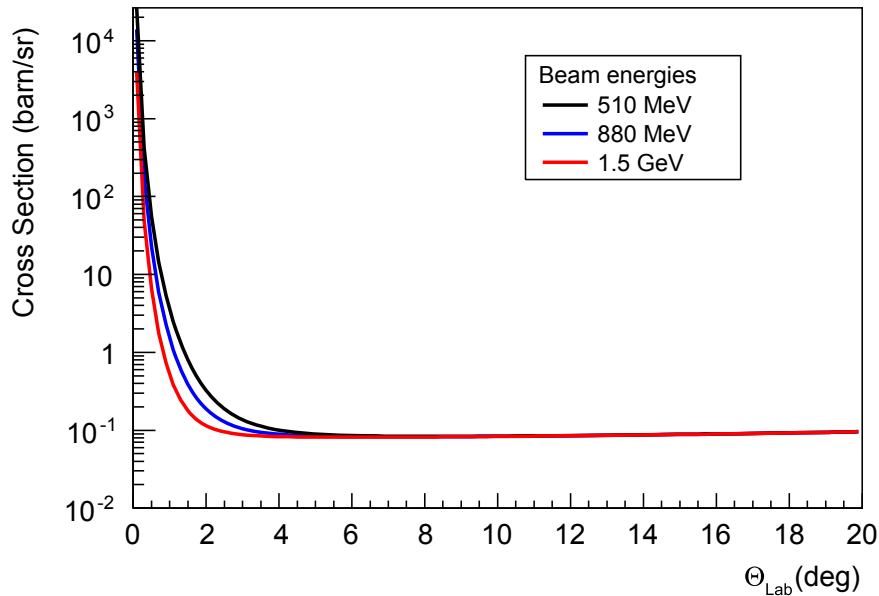


Figure 4.6: Møller scattering production cross section, in lab-system, for 510, 880 and 1500 MeV electron beam energies. At $\sim 5^\circ$ the cross section is practically independent of the beam energy.

were compared with the calculated rates of Møller scattering, elastic/quasi-elastic scattering off H and C and coherent scattering off C nuclei directly from the target (fig. 4.7). Taking out the Møller scattering as was explained before, the measured rate is in good agreement with the calculated rates for scattering on these nuclei.

All these sources of background can be reduced through the analysis of the signal produced in every event triggered. Figure 4.8 (left) shows a typical event display from the fiber detector. The signals produced are classified as (1) single random hits, (2) signal clusters, (3) after-pulses² and (4) trigger reference time. Figure 4.8 (right) shows a magnification of the signal cluster. The cluster is spread over 7 channels and 0.8 ns. It is known from previous tests (sec. 3.1) that charged particles crossing the fiber detector produce this kind of signal. In the case of two clusters being produced in the same event, the cluster with the time closest to the trigger signal is retained. Within the cluster, the time of the leading signal is chosen as the hit time.

The minimal temporal and spatial distance between signals in a cluster is defined before the analysis. Signals of type (1) and (3) are filtered out by the clustering algorithm of the trigger system (sec. 4.1). With this, the rate drops by a factor 10 with respect to the raw signal.

Requesting coincidences between both planes, the rate is reduced by a factor of 200 after the cluster filter, rejecting a high degree of particle back-

²Signals produced in a given channel that produced a previous signal during the same event.

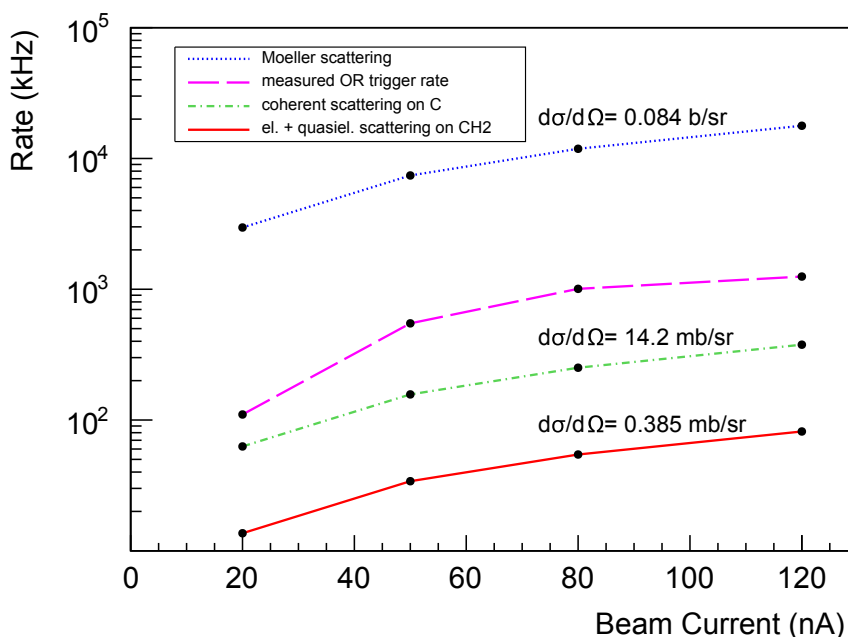


Figure 4.7: Signal rate comparison in X-plane during 2009 beam time as a function of the electron beam current. Measured raw signal rates are compared with the calculated scattering rates of Møller scattering, elastic/quasi-elastic scattering at H and C and coherent at C nuclei. Values for the differential cross-sections are shown. Figure from [126].

ground. Table 4.1 summarizes the rate reduction with the different trigger types. A total reduction of the trigger rate of 1 : 2000 is achieved for these tests.

Events with simultaneous temporal and spatial pile-up, like a background particle hitting the same cluster at the same time as a particle coming from the magnet, introduce some inefficiency to the trigger logic. For in-beam tests, such events could be neglected, but for later extensions, when the logic will include conditions on the reaction kinematics, a trigger efficiency smaller than 100% will be inevitable.

4.2.2 2010 beam test

With the central momentum of spectrometer C fixed at 350 MeV/c, the magnetic field of KAOS was changed in small steps³.

The correlated hits between planes X and \ominus for different magnetic field values are plotted (fig. 4.9). The length of the correlated data from the elastic reaction is limited by the horizontal angular acceptance of spectrometer C, which is quite smaller than KAOS. Since not all of the modules from the \ominus -plane were available, the gap between the two regions with modules prevents

³The control of the magnetic field of KAOS is done through a script scaled in units of the central momentum of the hadron side of the magnet.

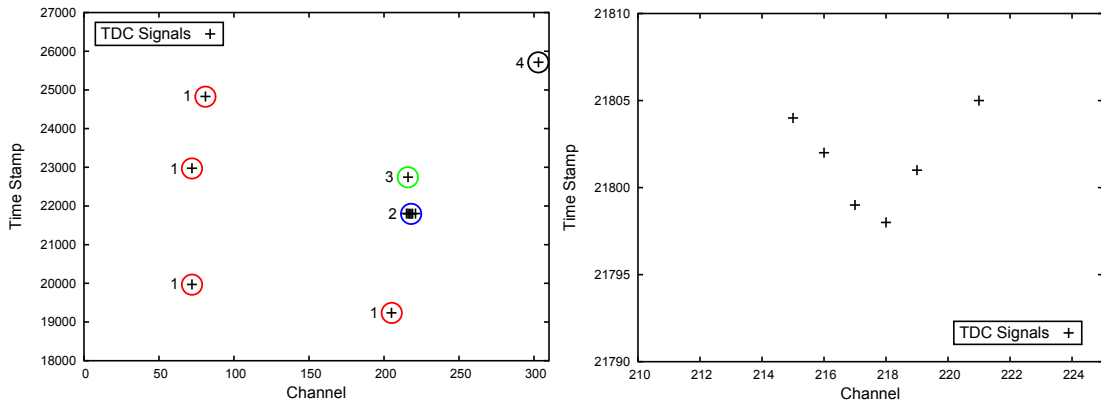


Figure 4.8: Left. A typical event display of the fiber detector during the in-beam test. Each cross represents the leading edge time (in time bins of $\Delta t \approx 118$ ps). Different signal types are seen in this event: (1) single random hits, (2) a signal cluster with (3) after-pulse, and (4) the trigger reference time. Right. Magnification of the signal cluster by the charged particle. Figure from [126].

one knowing the length of the line. The coincidence rate between C AND X AND \ominus was around 1 Hz with a beam current of 200 nA. Even with this low current, the target of CH₂ was degrading so fast that in the last data acquisitions the correlated line between both planes became quite blurred. This data can help spatially position the fiber planes in the simulation.

The reconstructed incident angle was also plotted in order to obtain more information to achieve a more precise simulation. The incident angle α , is calculated, following the scheme in fig. 4.10, as:

$$\alpha = \arctan \frac{a}{Z} \quad (4.2)$$

where:

$$\begin{aligned} a &= ((\text{ch } \ominus \times 0.83 \text{ mm}) + X_{\text{offset}} - (\text{ch } X \times 0.83 \text{ mm})) \\ X_{\text{offset}} &= 603.87 \text{ mm} \\ Z &= 258.63 \text{ mm} \end{aligned}$$

the channels are scaled in fiber diameters, and the angle is expressed in rad (converted in deg for plot purposes).

The reconstructed incident particle angle for different KAOS magnetic configurations (fig. 4.11) shows a strong peak around $72^\circ - 75^\circ$. From knowledge of this data, the planes can correct the tilt position (angular) in the simulation.

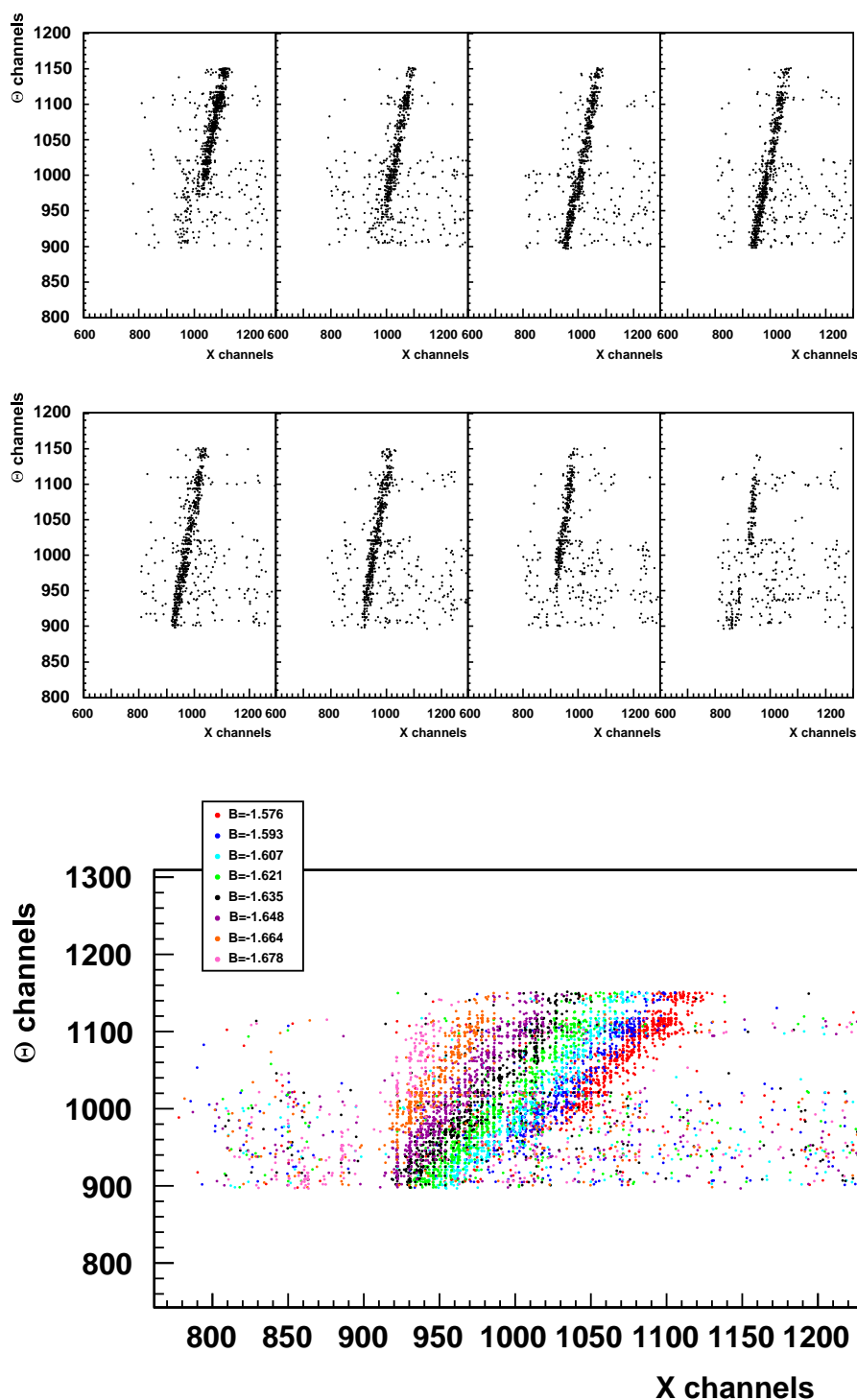


Figure 4.9: Top. X plane vs Θ -plane hits plots corresponding to different KAOS magnetic fields, from left to right, -1.576 T, -1.593 T, -1.607 T, -1.621 T, -1.635 T, -1.648 T, -1.664 T, -1.678 T. The dark line corresponds to the correlated signal in both planes from the protons of the elastic reaction. Since not all modules from the Θ -plane are available, the length of the “elastic” line could not be well determined. The plot corresponding to the -1.678 T configuration shows degrading data as a result of the destruction of the CH_2 target. Bottom. All plots superposed in one plot. Each set of data is plotted in a different color. It shows more evidently, how the “elastic” line moves with respect to the fiber planes with the variation of the magnetic field.

Table 4.1: Measured Trigger Rates in the Electron-Arm of the KAOS spectrometer during beam tests in 2009. The current of the 585 MeV Electron Beam on a 130 mg/cm^2 thick CH_2 target varied between 10 and 100 nA.[126]

Trigger Type	Trigger Rate (kHz)	Trigger Rate (kHz)
	@ 10 nA	@ 100 nA
Raw Signal Rate	100 ± 100	1120 ± 30
Clusters in X	7.33 ± 0.09	47.0 ± 0.2
Clusters in Θ	5.91 ± 0.08	37.3 ± 0.2
$X \text{ OR } \Theta$	13.2 ± 0.1	83.9 ± 0.3
$X \text{ AND } \Theta$	$(63 \pm 8) \times 10^{-3}$	$(490 \pm 20) \times 10^{-3}$
Random Coincidences	$(3.46 \pm 0.06) \times 10^{-3}$	$(140 \pm 1) \times 10^{-3}$

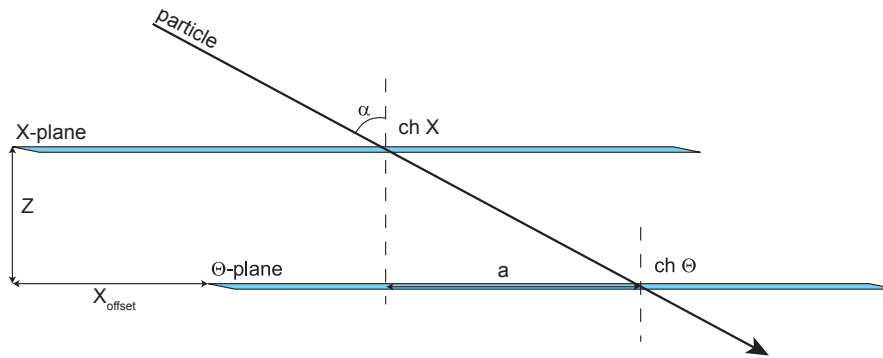


Figure 4.10: Scheme for incident angle reconstruction. Z and Y are the offset distances of both detector planes, determined by CAD drawings. The incident particle cross both planes with an angle α , activating channels $\text{ch } X$ and $\text{ch } \Theta$. The relative distance between the hitting channels is a .

4.3 Monte-Carlo simulation of the fiber detector

The data obtained in the 2010 beam time was used to calibrate a Monte-Carlo simulation of the fiber detector. It was made in order to extract the optical properties of the fiber detector in the KAOS spectrometer. It was done with the framework of Geant4 [115]. The main structure of the code was done by L. Nungesser [86] and adapted in this work for the analysis of the fiber detector.

The first step to characterize the fiber detector in the simulation is to reproduce the elastic reaction as was done during the beam time.

In Geant4, the input parameters are the emission angles of the electron within the acceptance of Spectrometer C. With the use of a uniform distribution, the angles are randomized in the range:

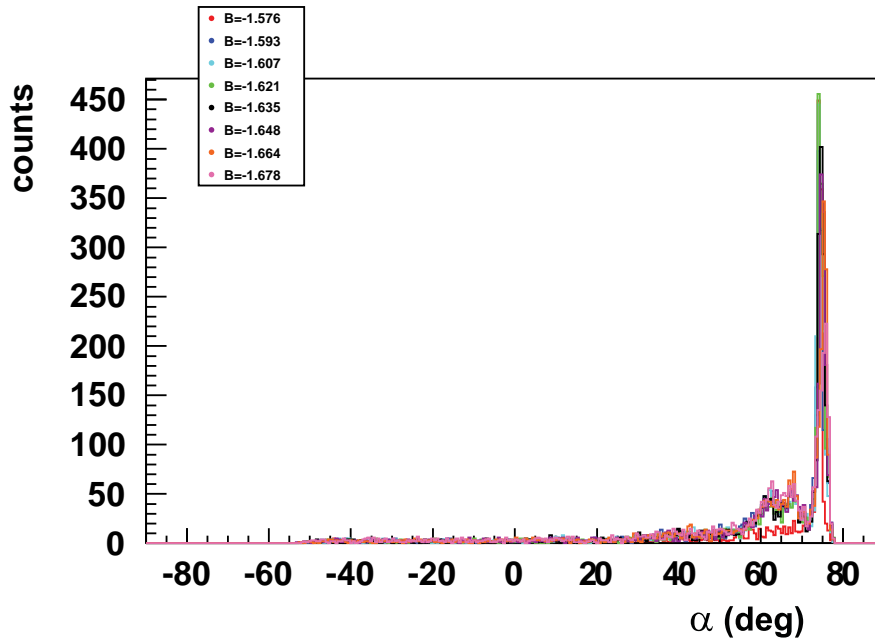


Figure 4.11: Reconstructed incident particle angle for -1.576 T, -1.593 T, -1.607 T, -1.621 T, -1.635 T, -1.648 T, -1.664 T, -1.678 T KAOS magnetic fields. The peak related to the proton from the elastic reaction is located around $72^\circ - 75^\circ$.

$$\theta \in [-5.7^\circ, 5.7^\circ] \Rightarrow \pm 100 \text{ rad}$$

$$\phi \in [-4^\circ, 4^\circ] \Rightarrow \pm 70 \text{ rad}$$

with θ as the horizontal acceptance angle and ϕ the vertical acceptance angle of Spectrometer C (sec. 1.2). For convenience, the angles are transformed to a spherical system frame (fig. 4.12) through the relations:

$$\theta_{sc} = \arccos \frac{1}{\sqrt{\tan^2 \theta + \tan^2 \phi + 1}}$$

Then the generator for an elastic reaction uses the formulas (considering $m_e \approx 0$):

$$\begin{aligned} |\mathbf{p}_{e'}| &= \frac{m_p E_e}{E_e + m_p - (E_e \cos \theta_{sc})} \\ E_p &= E_e + m_p - |\mathbf{p}_{e'}| \\ |\mathbf{p}_p| &= \sqrt{E_p^2 - m_p^2} \end{aligned}$$

where, m_p is the mass of proton, E_e the energy of electron beam, E_p and $|\mathbf{p}_p|$ the energy and momentum modulus of scattered proton and $|\mathbf{p}_{e'}|$ the momentum

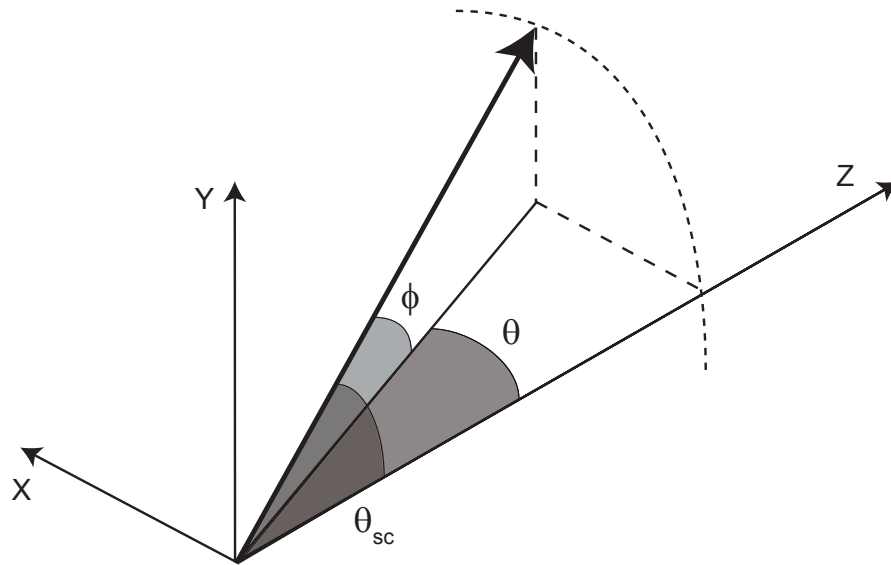


Figure 4.12: Scheme of the relation between cartesian angles from the spectrometer acceptance and scattering spherical angle.

modulus of the scattered electron. Only the energy of the incident electron and the cartesian angles of the acceptance of Spectrometer C, where the scatter electron was detected, are needed as input.

The direction of the scattered proton is calculated through momentum conservation:

$$\phi_p = -\arcsin\left(\frac{|\mathbf{p}_{e'}|}{|\mathbf{p}_p|}\right) \sin \phi$$

$$\theta_p = -\arcsin\left(\frac{|\mathbf{p}_{e'}|}{|\mathbf{p}_p|}\right) \sin \theta$$

The KAOS spectrometer was also simulated with its magnetic field map, provided by the KAOS collaboration from GSI and the two planes of the fiber detector[86] (fig. 4.13). The data acquisition was done requesting the energy deposition for each individual fiber and summing fibers of the same channel to store the channel hit. The energy deposition information could be used in order to simulate some kind of discriminator. In this simulation, the only information used was the hit channel without any energy request. Finally, only hits in both fiber planes were considered.

With the correlation hits plot between planes and the angle reconstruction, the simulation was programmed to achieve similar behavior to the real detector. Figure 4.14 shows the overlap plot of the real data, corresponding to a KAOS magnetic field of $B=-1.621$ T, with the simulated data.

In order to have a clean data set in the simulation, the scattering interaction of the simulated particles with the materials was highly suppressed. The simulation showed good agreement with the real data although some dis-

crepancies could be associated with the simulated magnetic field, specially the fringe area that could not be well implemented, and with the exclusive use of the hit channel information without any energy cut. Even so, this data made a suitable first approach to extract the optical properties of the fiber detector in the magnet.

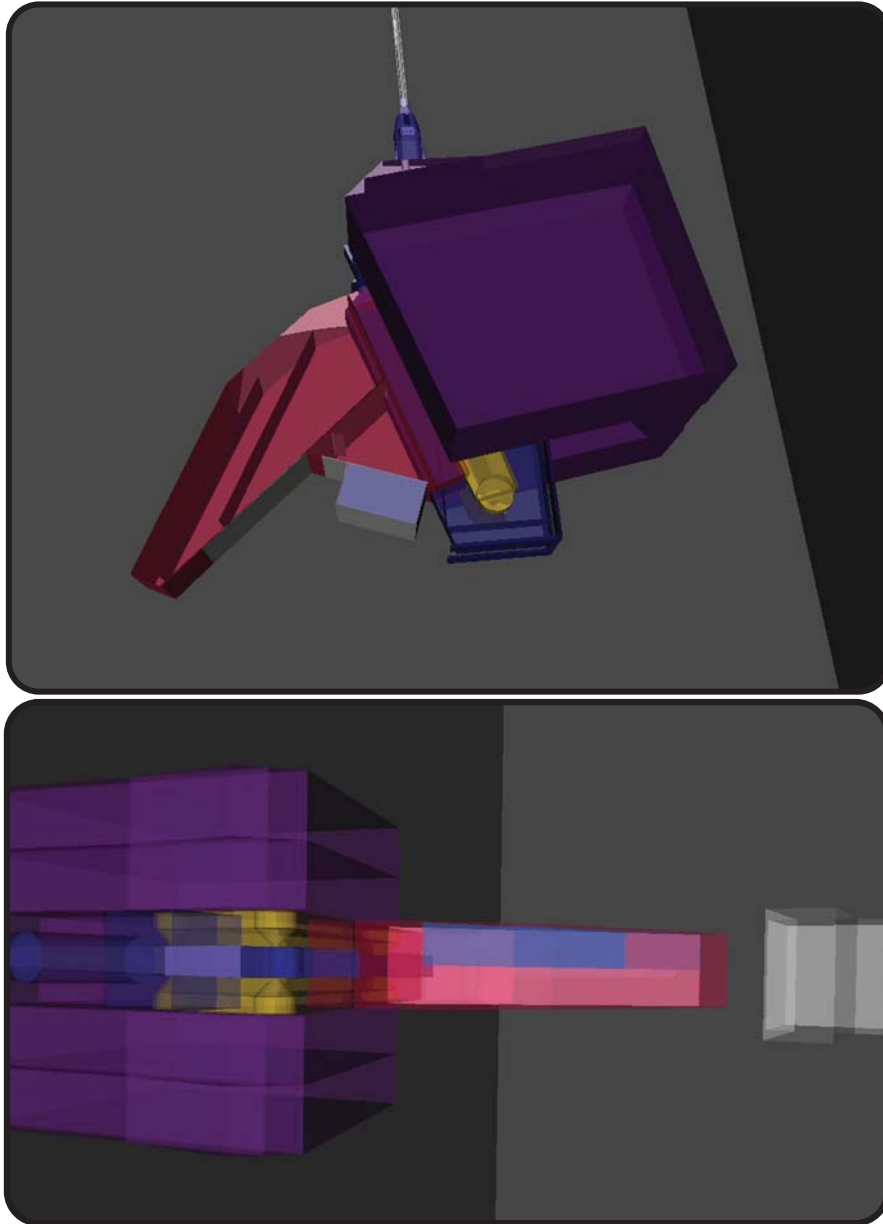


Figure 4.13: Pictures of the simulated KAOS spectrometer. Top. The new vacuum chamber of the fiber detector is represented in red, the yoke magnet in violet, the pole shoe in yellow and the new beam dump in light grey. Bottom, the picture shows how the fiber detector planes, in blue, extend close to the middle plane of the magnet.

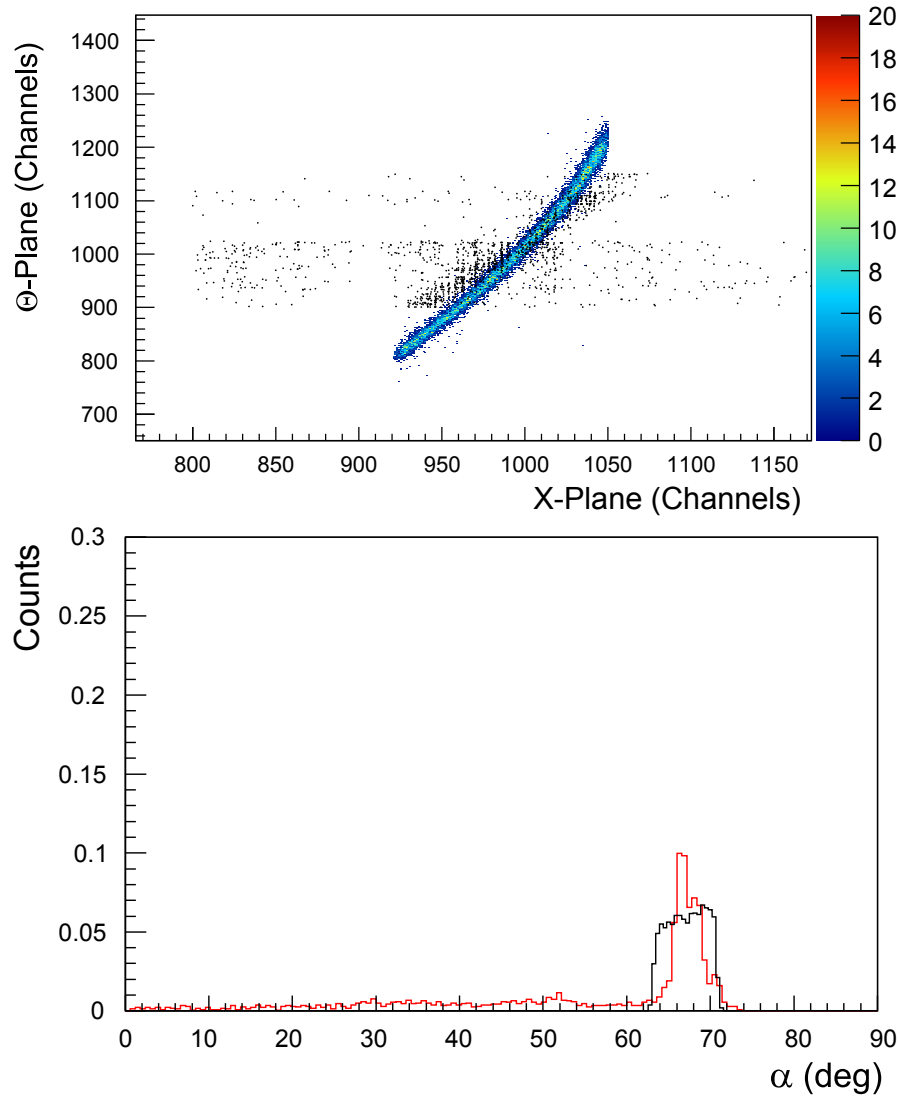


Figure 4.14: Top. Correlated hit pattern between Θ - and X -planes. Overlapped are the simulated data, in color scale, and real data, in black. The simulated pattern shows a good agreement with respect to the real data, although discrepancies can be associated with the fringe magnetic field which was not properly implemented in the code. Bottom. Overlap of the normalized reconstructed angle from real (red) and simulated data (black). The width of the simulated data peak can be associated with the exclusive use of hit channel data in the simulation without any energy restriction.

4.4 Fiber detector magnet-optics in KAOS

4.4.1 Theory of charged beam transport optics

The treatment for the determination of the parameters of the trajectories of charged particles in a magnetic field is based in the work of Karl L. Brown [133]. This work provides the complete mathematical treatment for the study of charged particles trajectories through static magnetic systems, based in development of a general vector differential equation under certain conditions and relating it with the Taylor's expansion of trajectories deviated from an arbitrary central trajectory. In this thesis, the study of the trajectories of the charged particles will be done to first order of such an expansion, which can be expressed as a matrix formulation.

4.4.1.1 Equation of motion in a magnetic field

A moving particle, with velocity \mathbf{v} , mass m and charge q under a magnetic field \mathbf{B} , experiences a force described by the Lorentz's force equation⁴ :

$$\frac{d\mathbf{p}}{dt} = q(\mathbf{v} \times \mathbf{B}) \quad (4.3)$$

If the magnetic field could be considered static and homogeneous, the force for a charged particle crossing the magnetic field, perpendicular to the force lines, is centripetal:

$$\frac{mv^2}{\rho} = qvB \quad (4.4)$$

therefore the particle follows a circular path of radius ρ . From eq.4.4, the momentum of the particle is:

$$p = qB\rho \quad (4.5)$$

i.e. with a given magnetic field, particles with different momentum are separated following the ρ path. Thus, it is possible to determine the momentum of the particle measuring the position of the particle after passing the magnetic field. The determination of the position of the particle after its passing the magnetic field is determined using a matrix treatment.

4.4.1.2 Solution and matrix formalism for the trajectory of a charged particle through a magnetic field

In order to study the trajectories described by a charged particle, only one previous restriction is imposed on the field to simplify the calculus. Relative to a plane, called magnetic midplane, the magnetic scalar potential φ is an

⁴The general expression of the Lorentz's force, *i.e.* under a electromagnetic field, is:
 $\mathbf{F} = q[\mathbf{E} + (\mathbf{v} \times \mathbf{B})]$

odd function in the transverse coordinate y (direction perpendicular to the midplane), *i.e.* $\varphi(x, y, t) = -\varphi(x, -y, t)$ ⁵. In terms of the magnetic field, this is equivalent to:

$$\begin{aligned} B_x(x, y, t) &= -B_x(x, -y, t) \\ B_y(x, y, t) &= B_y(x, -y, t) \\ B_t(x, y, t) &= -B_z(x, -y, t) \end{aligned}$$

It implies that in the midplane $B_x = B_t = 0$ and only B_y remains nonzero. Therefore, in the midplane, \mathbf{B} is normal to the plane and any particle trajectory lying in the midplane remains there through the system. The midplane is also called the dispersive plane because in this plane particles with different momenta disperse. The reference frame used in the derivation of the equation of motion is shown in fig. 4.15.

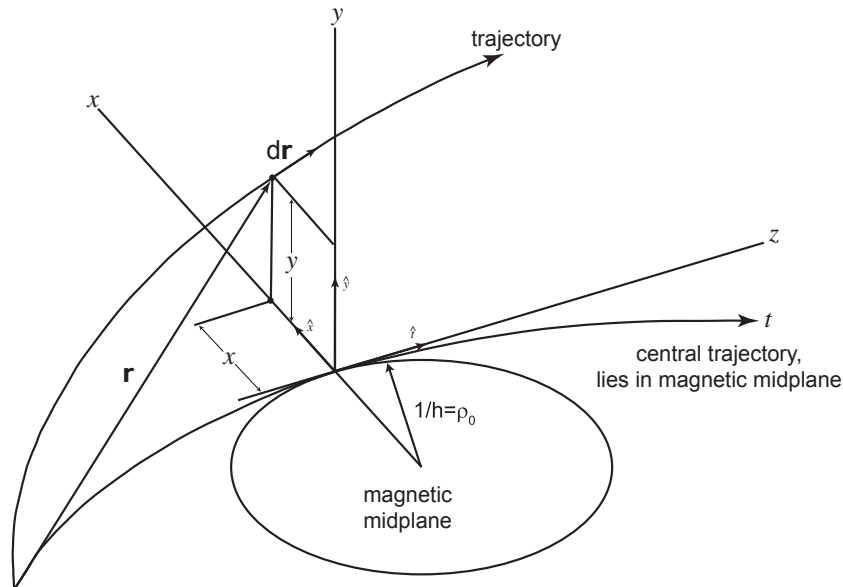


Figure 4.15: Curvilinear coordinate system used in the derivation of the equations of motion.

Observe that the coordinate system used is a right handed system which satisfies $\hat{t} = \hat{x} \times \hat{y}$. The trajectories are described by mean of a Taylor's expansion with respect to a reference trajectory, which lies within the magnetic midplane, called the central trajectory and as function of t .

The definition of the coordinates used in the derivation of the equation of motions is as follows:

- x : radial deviation from the central trajectory.

⁵Note that these are curvilinear coordinates, *i.e.* in each point of the trajectory, can be defined a rectangular system with x and y as transversal components and t as longitudinal component

- y : transversal deviation from the central trajectory.
- Θ : angle of the trajectory with respect to the central trajectory, in the dispersive plane. In the paraxial approximation $\Theta \approx \tan \Theta = dx/dt$.
- Φ : angle of the trajectory with respect to the central trajectory, in the transversal (or non-dispersive) plane. In the paraxial approximation $\Phi \approx \tan \Phi = dy/dt$.

Two more variables are needed, which are not obvious from the reference system drawn:

- l : path length difference between the trajectory and the central trajectory.
- δ : relative momentum difference with respect to the momentum of the central trajectory, $\Delta p/p_0$.

The Taylor expansions for the spatial parameters, in the most general form to n^{th} order, are:

$$\begin{aligned} x(t) &= \sum_{i,j,k,l,m=0}^n (x|x_0^i y_0^j \Theta_0^k \Phi_0^l \delta^m) x_0^i y_0^j \Theta_0^k \Phi_0^l \delta^m \\ y(t) &= \sum_{i,j,k,l,m=0}^n (y|x_0^i y_0^j \Theta_0^k \Phi_0^l \delta^m) x_0^i y_0^j \Theta_0^k \Phi_0^l \delta^m \\ \Theta(t) &= \sum_{i,j,k,l,m=0}^n (\Theta|x_0^i y_0^j \Theta_0^k \Phi_0^l \delta^m) x_0^i y_0^j \Theta_0^k \Phi_0^l \delta^m \\ \Phi(t) &= \sum_{i,j,k,l,m=0}^n (\Phi|x_0^i y_0^j \Theta_0^k \Phi_0^l \delta^m) x_0^i y_0^j \Theta_0^k \Phi_0^l \delta^m \end{aligned}$$

where the subscript 0 indicates the value of the parameter at $t=0$. These five initial values will have the value 0 for the central trajectory itself. The parentheses are symbols for the Taylor coefficients to be determined. From the midplane symmetry, required at the beginning, it is obtained that the constant term is zero and the terms that would indicate a coupling between the coordinates x and y are also zero.

In a first approximation, the Taylor's expansion can be expressed in matrix form:

$$x_i = \sum_{j=1}^6 R_{ij} x_j(0)$$

where R_{ij} is a first order matrix element and:

$$x_1 = x, x_2 = \Theta, x_3 = y, x_4 = \Phi, x_5 = l, x_6 = \delta$$

finally $x_j(0)$ is the value of the j -coordinate at $t=0$. The matrix representation is:

$$\begin{pmatrix} x(t) \\ \Theta(t) \\ y(t) \\ \Phi(t) \\ I(t) \\ \delta(t) \end{pmatrix} = \begin{pmatrix} R_{11} & R_{12} & 0 & 0 & 0 & R_{16} \\ R_{21} & R_{22} & 0 & 0 & 0 & R_{26} \\ 0 & 0 & R_{33} & R_{34} & 0 & 0 \\ 0 & 0 & R_{43} & R_{44} & 0 & 0 \\ R_{51} & R_{52} & 0 & 0 & 1 & R_{56} \\ 0 & 0 & 0 & 0 & 0 & 1 \end{pmatrix} \begin{pmatrix} x_0 \\ \Theta_0 \\ y_0 \\ \Phi_0 \\ I_0 \\ \delta_0 \end{pmatrix} \quad (4.6)$$

The elements $R_{13} = R_{14} = R_{23} = R_{24} = R_{31} = R_{32} = R_{41} = R_{42} = R_{36} = R_{46} = 0$ are a consequence of the restriction from the midplane symmetry. The zeros in the sixth row result from the restriction of static magnetic fields [133, 134].

In the first-order approximation, the determinant of a transfer matrix is the unity whether or not we assume the midplane symmetry [135]. This means that the matrix corresponds to an orthogonal transformation. As its determinant is +1, corresponding to a right-handed coordinate system.

The non-zero terms of the matrix could be determined by Monte-Carlo methods. For visual commodity in the following calculations, is appropriate to use brackets nomenclature for the matrix elements:

$$\begin{aligned} R_{11} &= \langle x|x_0 \rangle & R_{12} &= \langle x|\Theta_0 \rangle & R_{16} &= \langle x|\delta_0 \rangle \\ R_{21} &= \langle \Theta|x_0 \rangle & R_{22} &= \langle \Theta|\Theta_0 \rangle & R_{26} &= \langle \Theta|\delta_0 \rangle \\ R_{33} &= \langle y|y_0 \rangle & R_{34} &= \langle y|\Phi_0 \rangle \\ R_{43} &= \langle \Phi|y_0 \rangle & R_{44} &= \langle \Phi|\Phi_0 \rangle \\ R_{51} &= \langle I|x_0 \rangle & R_{52} &= \langle I|\Theta_0 \rangle & R_{56} &= \langle I|\delta_0 \rangle \end{aligned}$$

4.4.2 Characterization of the fiber detector in KAOS

Since the fiber detector consists of two planes, which measure the X and Θ -coordinates, the simulation is restricted to these two coordinates which can be compared with the data obtained in the beam time. In order to characterize the fiber detector within the simulation, a simulated field of $B=1.4$ T was chosen. With this field, the central momentum, defined as the momentum of the particle which crosses the fiber plane at the central channel (ch. 1152), is fixed in $p_0 = 482.7$ MeV. Each event produced in the simulation is stored when the particle crosses both planes, even so the analysis is produced mainly with the information of the X -plane.

As the fiber plane is not perpendicular to the path of the incident particle path, the result should be corrected for this angle. For this reason it is convenient to define the following variables:

$$\begin{aligned} \Theta &= \alpha - \alpha_0 \\ X &= ((\text{ch } X - \text{ch } X_0) \times 0.83 \text{ mm}) \times \cos \alpha_0 \end{aligned} \quad (4.7)$$

where α is the incident angle of the particle in the fiber detector as calculated in eq. 4.2, α_0 is the incident angle of the central momentum particle at the fiber

detector. The reconstructed angle of the central momentum is $\alpha_0 = 71.42^\circ \approx 1.25$ rad. The fiber detector channels are scaled with respect to the central channel $ch X_0=1152$ which defines the central momentum and then expressed in millimeters in fiber diameters. The result is corrected with respect to the angle α_0 .

With the simulation able to reproduce real data (sec. 4.3), it is possible to determine the momentum acceptance of the fiber detector in the X -plane. Figure 4.16 shows the momentum acceptances for different fields without the scale correction. It shows that the channels acceptance does not depend on the field. The momentum acceptance reduced with respect to the central channel for our configuration ($B=1.4\text{ T} \rightarrow p_0 = 482.7\text{ MeV}$) is shown in figure 4.17 for different emission angle Θ_0 , -10° , -5° , 0° , 5° and 10° . It shows that the momentum acceptance is around 20 % to -25 % with respect to the central momentum.

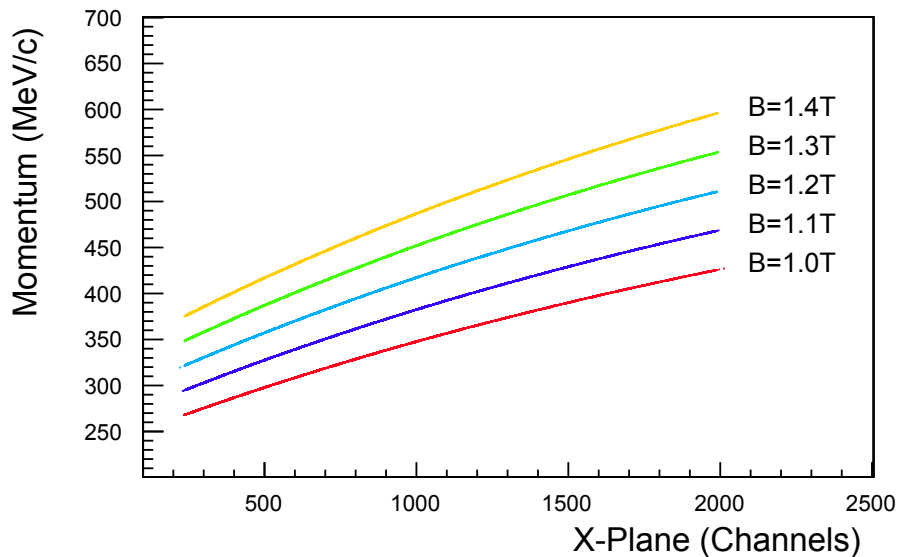


Figure 4.16: Momentum acceptance for $B=1.4\text{ T}$, 1.3 T , 1.2 T , 1.1 T , 1.0 T , magnetic field configurations.

Also, the angular acceptance, fig. 4.18, could be determined. It was simulated assuming a broad acceptance at the entrance of the spectrometer, $[-15^\circ, 15^\circ]$, although it is smaller. It was calculated for momenta of -10% , -5% , 0% , 5% and 10% of central momentum. It shows that the fiber detector has a wide acceptance for low momentum decreasing for small angles as the momentum increases.

In a similar way, is possible to calculate the angular acceptance as a function of the momentum. As done before, the emission angle was varying between $[-15^\circ, 15^\circ]$ range, in one degree steps. The result is shown in figure 4.19, every color strip represent one step. It shows that momentum angular acceptance is limited for small emission angles, but is quite wide for angles greater than -5° , even the momentum acceptance changes along the emission angle.

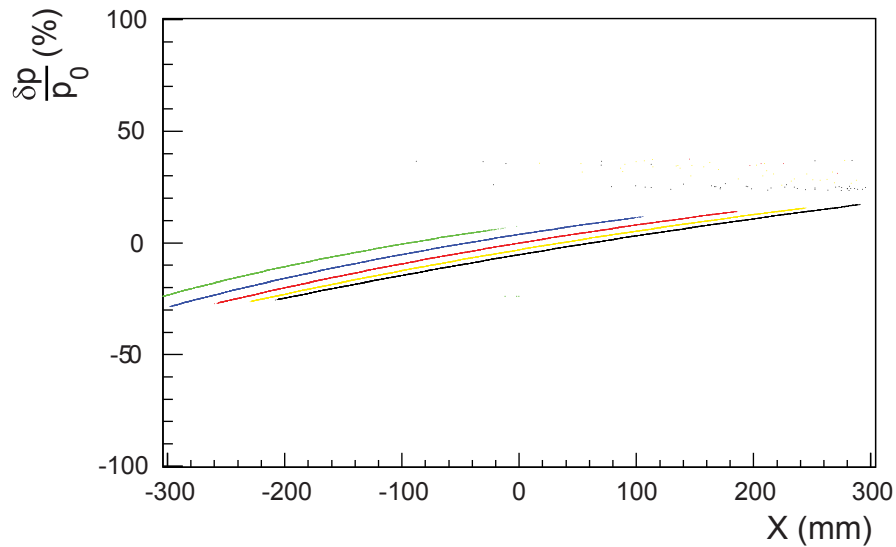


Figure 4.17: Momentum acceptance reduced with respect to the central momentum for emission angle, Θ_0 , -10° (green), -5° (blue), 0° (red), 5° (yellow) and 10° (black). It can be measured so the momentum acceptance is in the order of 20% to -25% with respect to the central momentum.

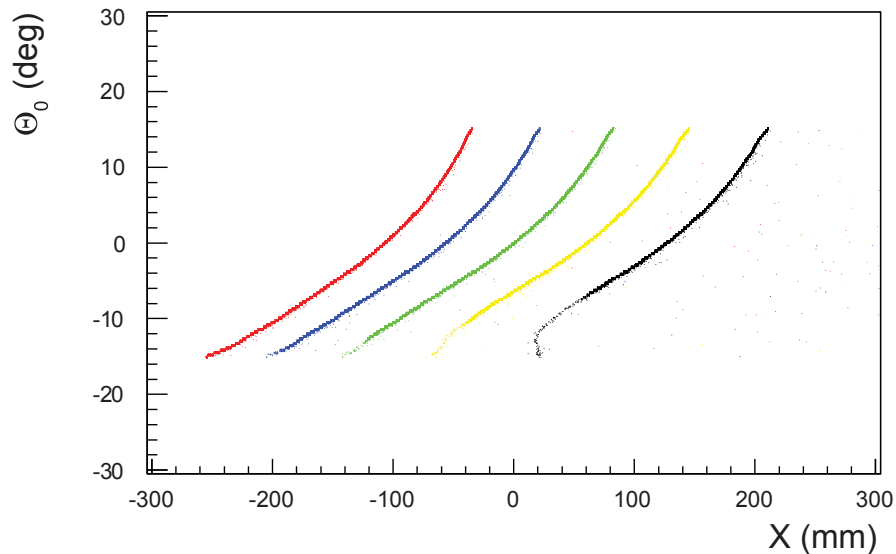


Figure 4.18: Spatial angular acceptance of -10% (red), -5% (blue), 0%, (green), 5% (yellow) and 10% (black) of the central momentum. For higher momenta, the angular acceptance becomes narrow though for momenta of -10%, -5% and 0% has practically the same length.

Both calculations show that for small emission angles, *i.e.* angles $< -5^\circ$, the acceptance of KAOS is quite compromised, but since its real entrance acceptance range is smaller than that used for the simulation, the plots show that the fiber detector had a nice response for angular acceptance.

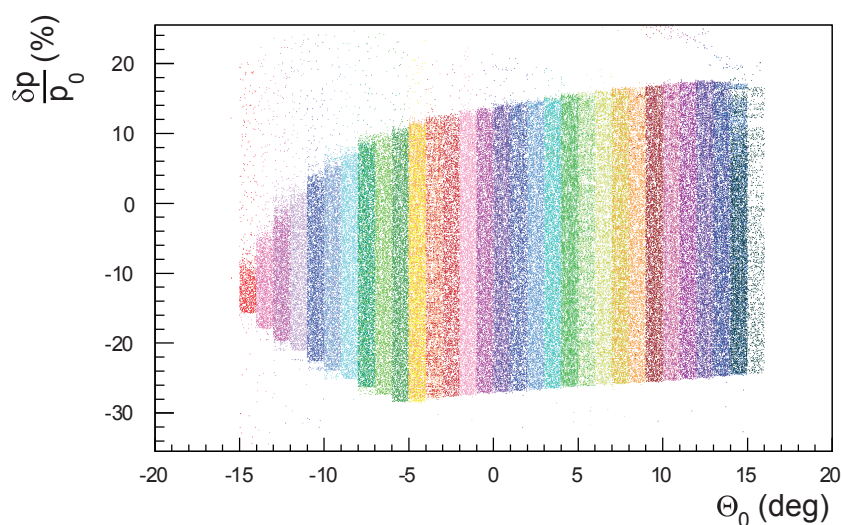


Figure 4.19: Momentum angular acceptance as a function of the emission angle. Every color strip represent a fixed emission angle. It shows that for angles lower than -5° the momentum acceptance is quite compromised becoming smaller, meanwhile at bigger angles it is practically wide constant even it changes along higher angles.

The path length of the central momentum was determined by the simulation to be 3679 mm. This length includes a variable distance from the target to a reference point within KAOS, where the field and detectors are referenced. In this simulation this distance is 1325 mm. This variable distance could be different depending of the final set-up, but it does not influence the calculus of the matrix elements. The knowledge of the path length is primordial in the implementation of an efficient trigger in order to subtract particle coming directly from the target, which have a smaller path length than particles coming through the magnet (sec. 4.1).

In a similar way to before, it is possible to determine the variation of the path length depending on different parameters. Figure 4.20 shows the variation of the path length with respect to the position corrected, for different emission angle Θ_0 : -10° , -5° , 0° , 5° and 10° .

With the same variation of emission angles as before, the variation of the path length with respect to the momentum is show in fig. 4.21.

Finally, with variation of momentum of -10%, -5%, 0%, 5% and 10% with respect to central momentum the variation of the path length respect to the emission angle was determined (fig. 4.22). The range of Θ_0 is $[-15^\circ, 15^\circ]$, as was made in previous plots.

All these calculations show that the path length varies from a minimum of 2600 mm to a maximum of 4800 mm. These extreme values could be smaller, since they were calculated for extreme variations of the parameters.

The determination of the different elements of the transfer matrix were made introducing small variations respect to the initial conditions and mea-

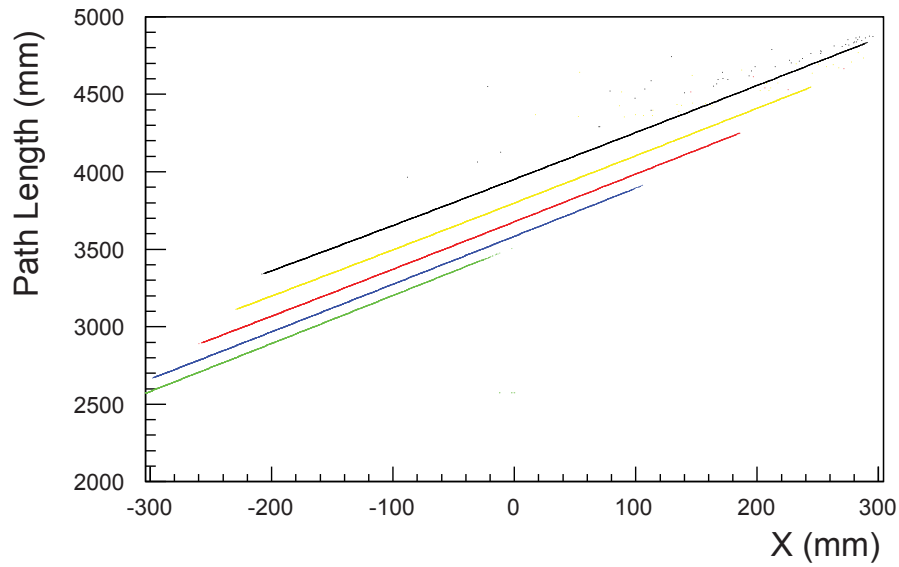


Figure 4.20: Variation of the path length with respect to the position corrected, for different emission angles Θ_0 : -10° (green), -5° (blue), 0° (red), 5° (yellow) and 10° (black).

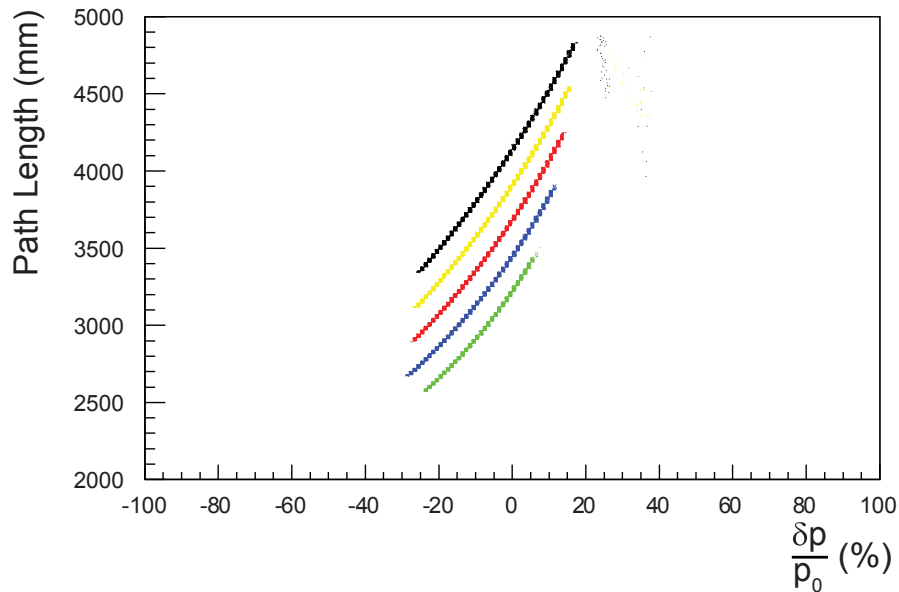


Figure 4.21: Variation of the path length with respect to the reduced momentum, for different emission angles Θ_0 , -10° (green), -5° (blue), 0° (red), 5° (yellow) and 10° (black).

suring the response of the detector to the variation.

In figure 4.23 is shown how to determine the elements $\langle x|x_0 \rangle$, $\langle x|\Theta_0 \rangle$ and $\langle x|\delta \rangle$ schematically. The matrix elements $\langle \Theta|x_0 \rangle$, $\langle \Theta|\Theta_0 \rangle$ and $\langle \Theta|\delta \rangle$, are determined in a similar way, but in this case the use of the second plane in order to reconstruct the incident angle of the particles is mandatory.

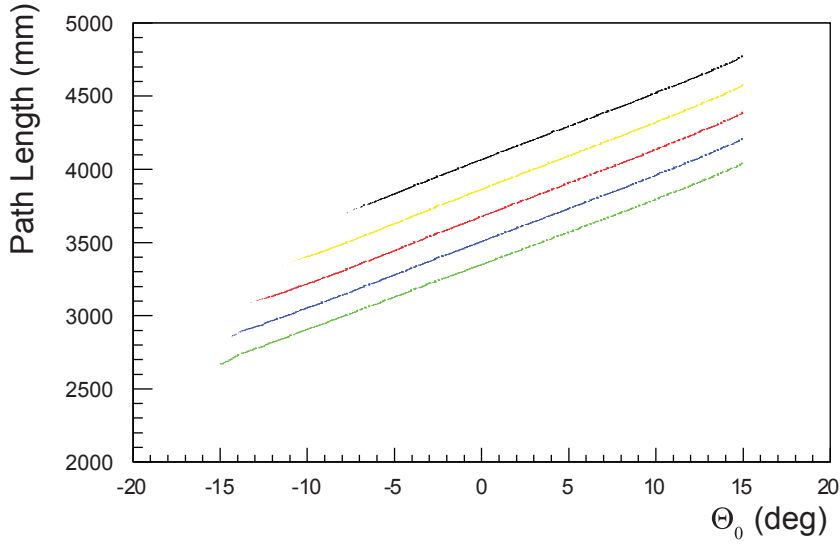


Figure 4.22: Variation of the path length with respect to emission angle, for different momentum of -10% (green), -5% (blue), 0% (red), 5% (yellow) and 10% (black) respect to central momentum. The range of Θ_0 is $[-15^\circ, 15^\circ]$

The elements $\langle I|x_0 \rangle$, $\langle I|\Theta_0 \rangle$ and $\langle I|\delta_0 \rangle$ are calculated knowing the path length of the central momentum from the target to the X-plane given by the simulation which is 3679 mm.

The transfer matrix elements for the fiber detector in the KAOS spectrometer are summarized in table 4.2.

Table 4.2: Transfer matrix elements for the KAOS spectrometer.

\mathbf{R}_f matrix elements	KAOS—
$\langle \mathbf{x} \mathbf{x}_0 \rangle$	-0.66
$\langle \mathbf{x} \Theta_0 \rangle$ (cm/mrad)	0.0459
$\langle \mathbf{x} \delta \rangle$ (cm/%)	1.18
$\langle \Theta \mathbf{x}_0 \rangle$ (mrad/cm)	-9.28
$\langle \Theta \Theta_0 \rangle$	-0.87
$\langle \Theta \delta \rangle$ (mrad/%)	5.86
$\langle I \mathbf{x}_0 \rangle$	-2
$\langle I \Theta_0 \rangle$ (cm/mrad)	26.3
$\langle I \delta_0 \rangle$ (cm/%)	3.81

In reduced matrix form only for terms calculated for the fiber detector:

$$\mathbf{X} = \mathbf{R}_f \mathbf{X}_0 \rightarrow \begin{pmatrix} \mathbf{x}(t) \\ \Theta(t) \\ I(t) \\ \delta(t) \end{pmatrix} = \begin{pmatrix} -0.66 & 0.0459 & 0 & 1.18 \\ -9.28 & -0.87 & 0 & 5.86 \\ -2 & 2.63 & 1 & 3.81 \\ 0 & 0 & 0 & 1 \end{pmatrix} \begin{pmatrix} \mathbf{x}_0 \\ \Theta_0 \\ I_0 \\ \delta_0 \end{pmatrix}$$

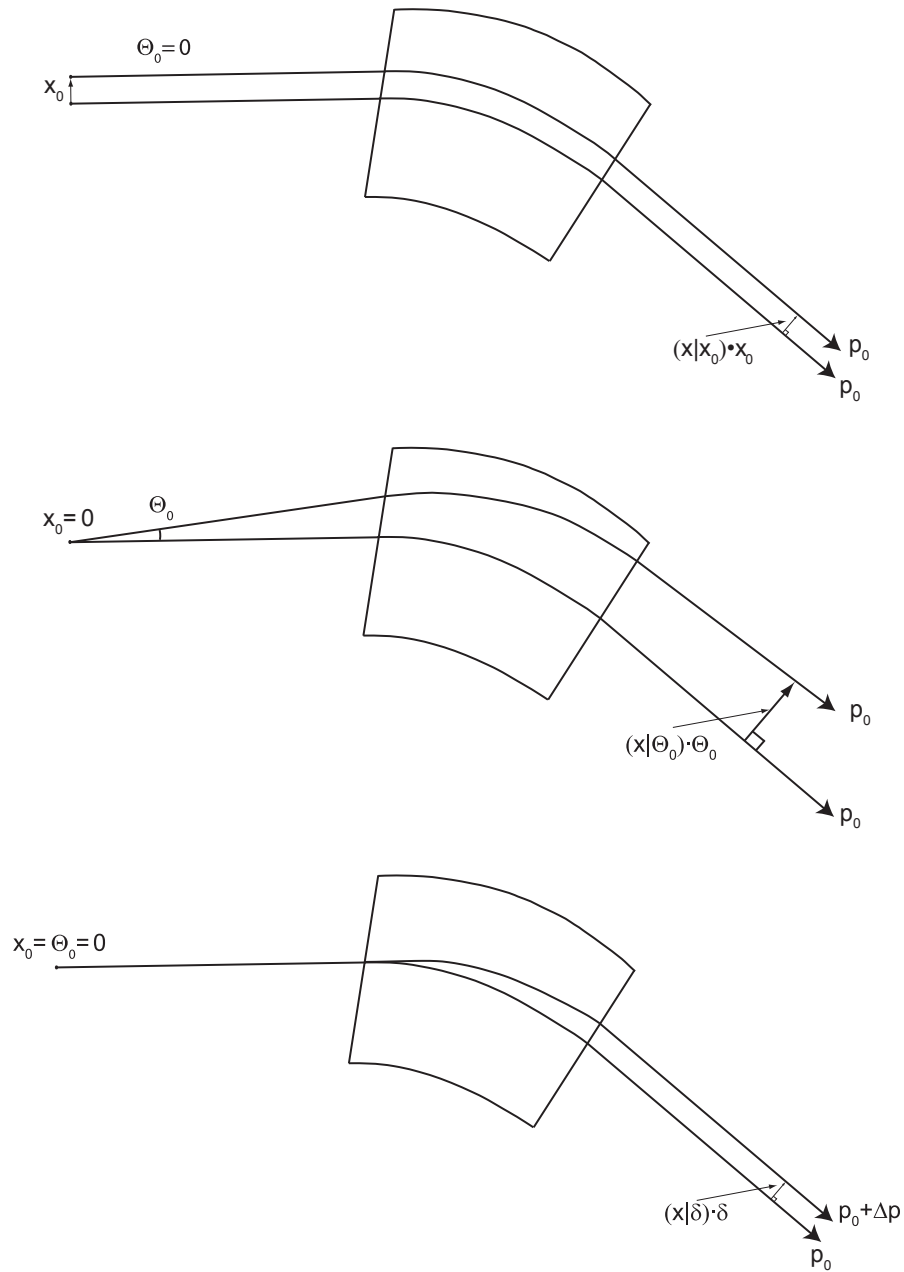


Figure 4.23: Graphical scheme showing how to determine some elements of the transfer matrix: $\langle x|x_0 \rangle$ (top), $\langle x|\Theta_0 \rangle$ (middle) and $\langle x|\delta \rangle$ (bottom). Measuring the response of the detector (in this case, the position difference with respect to the central momentum path) the matrix element is easily determined. Figures inspired from [134].

This transfer matrix gives the parameters for calculating the coordinates *target*→*detector* (eq. 4.6) or forward direction. Since, in real experiments, what is measured is the data from the detector in order to get information of the target, the calculus of the *detector*→*target* or backward matrix \mathbf{R}_b is mandatory.

The backward matrix is calculated through the following transfer coefficients.

$$\Theta_0 = \sum_{i,j=0}^n (\Theta_0 | x^i \Theta^j) x^i \Theta^j$$

$$\delta_0 = \sum_{i,j=0}^n (\delta_0 | x^i \Theta^j) x^i \Theta^j$$

In first order approximation, and with the use of the forward matrix elements, *i.e.* inverting the appropriate elements, the backward matrix is:

$$X_0 = \mathbf{R}_b X \rightarrow \begin{pmatrix} \delta_0 \\ \Theta_0 \end{pmatrix} = \begin{pmatrix} 4.52 & -0.91 \\ 0.67 & 0.035 \end{pmatrix} \begin{pmatrix} x(t) \\ \Theta(t) \end{pmatrix}$$

Table 4.3: Backward transfer matrix elements for the KAOS spectrometer.

\mathbf{R}_b matrix elements	
$\langle \Theta_0 x \rangle$ (mrad/cm)	4.52
$\langle \Theta_0 \Theta \rangle$	-0.91
$\langle \delta x \rangle$ (%/cm)	0.67
$\langle \delta \Theta \rangle$ (%/mrad)	0.035

The backward transfer matrix was incorporated in the analysis software of the A1 collaboration, `Cola++` [123], and with the use of the same set of data used for the simulation, a magnetic field of KAOS of $B=-1.621$ T, to extract the information from the target. The analysis had shown that with the use of a CH_2 target, the signal detected was dominated by the quasielastic scattering from the carbon nucleus.

The reconstructed proton momentum is shown in fig. 4.24. The maximum of the fit is located at 553 MeV/c although it is expected at a value of 568 MeV/c from the elastic kinematics (sec. 4.2). But considering the mean binding energy per nucleon in ^{12}C nuclei of 25 MeV, in the kinematics, the momentum of the proton for detection is 555 MeV/c in KAOS at 37.5° with a beam energy of 510 MeV.

It is confirmed from the reconstruction of the beam energy, fig. 4.25, from the information of the reconstructed proton momentum, the emission angle, the spectrometer C detection angle as a parameter and the subtraction of the mean binding energy for a nucleon in ^{12}C nuclei of 25 MeV. The reconstructed

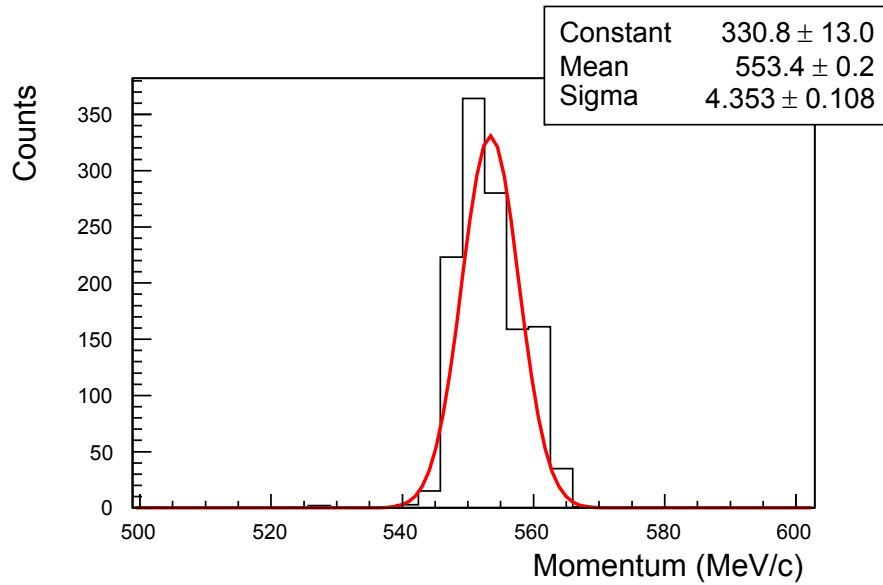


Figure 4.24: Proton momentum reconstructed with the use of the backward matrix calculated from the simulation. The fit shows a value of 553.4 ± 4.4 MeV/c. The nominal value from the kinematics is 555 MeV, so the deviation from this value is of 0.3%.

energy has a $\Delta E/E \sim 3.3\%$ (FWHM) and shows a deviation from the nominal value of the beam energy of 0.3%. The momentum measured corresponds to the information of one coordinate, *i.e.* from the dispersion plane, but since Spectrometer C triggered the reaction from electrons which scatter out of the dispersion plane of KAOS, the momentum measured at the fiber detector is slightly smaller than that corresponding to scattering within the dispersive plane.

Figure 4.26 shows the reconstructed emission angle at target with a gaussian fit between the limits used as a cut for the previous calculations of -5.5° and -2° . This data was used to correct the position angles of the spectrometers, which were given as fixed parameters for an elastic reaction, in the previous reconstructed parameters. As the reaction was considered elastic, the reconstructed angle in KAOS should be centered at 0° , but since the quasielastic reaction is dominant, there is a deviation from the nominal detection angles.

In spite of the issue of quasielastic scattering dominating the reaction that was alleged as elastic, the use of first order parameters in the transfer matrix, the low statistics in the test data and the lack of information for ϕ in the fiber detector, the reconstruction of the parameters at target have shown good accuracy and the feasibility of its use as focal plane detector for momentum reconstruction.

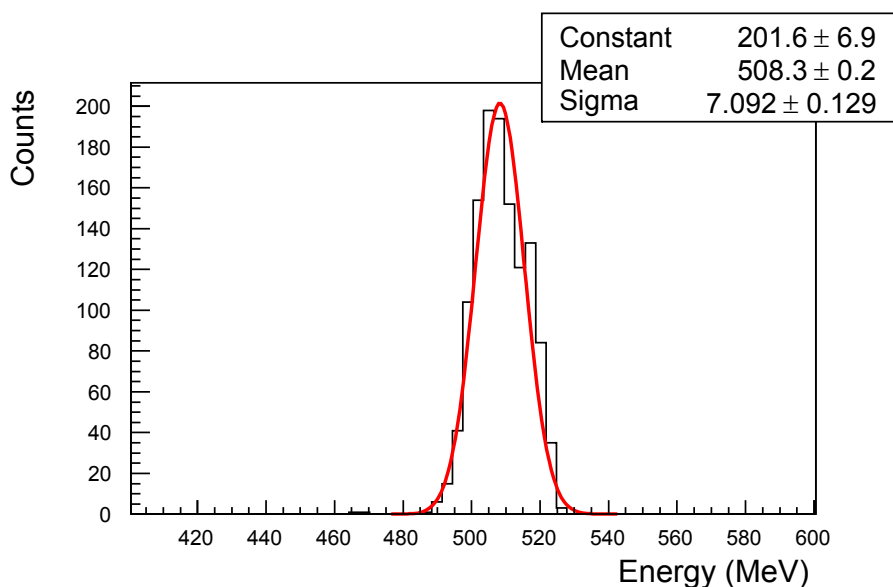


Figure 4.25: Beam energy reconstructed from the reconstructed proton momentum and the emission reconstructed angle with the angle of electron, detected in Spectrometer C, as a parameter. In the reconstruction the mean binding energy for a nucleon in ^{12}C nuclei of 25 MeV was subtracted.

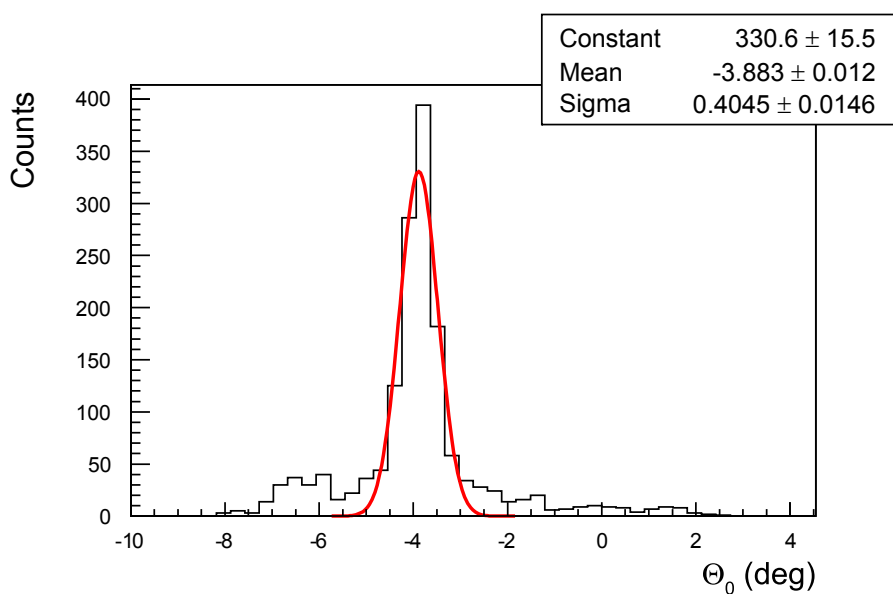


Figure 4.26: Proton emission angle reconstructed and adjusted with a Gaussian curve between -5.5° and -2° , showing a mean value of -3.9° . This data was used to correct the position angles of the spectrometers, which were given as fixed parameters, for the reconstructed parameters where this information is used.

Summary

For more than sixty years, strangeness had been an useful tool for study of the strong interaction and its contribution to understanding the particle puzzle with the postulation of the quark model as the fundamental representation of the group $SU(3)$. Out of pioneering research with cosmic rays, with the use of accelerators, the production of strangeness had been done with different production mechanisms.

Production of strangeness provides relevant information in the meson production which is fundamental information for phenomenological theories of Quantum Chromodynamics (QCD) at low energies. In the production of strangeness in bound systems, hypernuclei, one has an opportunity to study the strong interaction, through the YN interaction. Because the hyperon does not experience Pauli blocking, it makes it easy for it to interact with deeply bound nucleons.

In last years, the improvement of high quality continuous wave electron beams had provided a powerful tool for production of open strangeness. In 2007, the Mainzer Mikrotron (MAMI), managed by Institut für Kernphysik of Mainz (IKPH), had been upgraded to provide an electron energy beam of 1.5 GeV, which is over the strangeness production threshold.

Strangeness experiments in Mainz can be made at the three spectrometer facility handled by the A1 collaboration. But the use of the existing high resolution spectrometers was not efficient for strangeness research. The acquisition, commissioning and upgrading of the Kaon Spectrometer (KAOS) from GSI allows one to solve the drawbacks of the long path length of the existing spectrometers, allowing a more efficient detection of the kaons associated with the electroproduction of strangeness.

KAOS can be used in association with the other spectrometer, but for hypernuclear production, and the condition of very forward detection angles, this combination is not longer suitable for this kind of experiments. Due to the geometry of the pole shoe, KAOS can be used as a double spectrometer at 0° . In this case, KAOS should be implemented with detectors at the electron side.

A state-of-the-art scintillator fiber hodoscope had been designed, built and tested. As was seen, it consists of two planes of a length of ~ 2 m each and a height of ~ 43 cm. The planes consist in 18432 scintillator fibers of 0.83 mm diameter, grouped in 4 fibres per read out channel and 32 channels per module. The read out is made with the use of a Multi anode PhotoMultiplier (MaPMT) from HAMAMATSU model H7259K with 32 channels. This has the particularity that, instead of supplying power to them through a voltage divider, as with common PMTs. They are powered with voltage multiplier cells by means of a Cockroft-Walton circuit. Its use reduces the use of stiff and expensive high voltage cables for flexible flat cables, which provides power, 140 V dc, and control of each cell.

The signal is processed with the use of Double Threshold Discriminators (DTDs) developed at the IKPH, which eliminates the walk effect. The output signal is distributed among TDC-CATCH Mezzanine Card (TDC-CMC) modules, for timing measurements, and VME Universal PROcessing Module (VUPROM) modules, for trigger purposes.

Two prototypes were tested at GSI with a carbon beam, measuring a time resolution of ~ 220 ps and a spatial resolution of $460 \mu\text{m}$.

In 2010 the fiber hodoscope was tested in its working position in KAOS under electron beam conditions measuring the resulting protons from an elastic reaction with a plastic target. It was used to characterize the detector under real conditions and to compare with simulations to extract the opto-magnetic parameters of the spectrometer. The transfer matrix was calculated to first order.

The resulting parameters were tested with the collected data in order to reconstruct the elastic reaction at target and showed a good agreement with the calculated values. It shows the good performance of the detector and the good accuracy in the calculation of the transfer matrix.

With the characterization of the fiber hodoscope it is possible to use it with the set-up using the chicane. This is because with the use of the chicane, the electron beam passes through the pole shoe making the magnetic configuration of KAOS more restricted in order to keep the beam into the beam dump.

This scintillating fiber hodoscope is the appropriate detector to complete KAOS in order to achieve appropriate conditions for hypernuclear experiments.

Technical drawings

A.1 The fiber-photomultiplier interface

The fiber bundle is attached to an interface, called cookie, in order to set the fibers, corresponding to a read out channel, into the corresponding MaPMT pixel, keep the MaPMT aligned and fixed against the fibers and provide enough vacuum tight when is attached to the supporting frame.

The cookie is made of PVC and is designed with a shape to fit its corresponding projected space over the triple board (sec.2.2.2). The cookie holds two clamping plates made of aluminium for fixing purposes of the MaPMT (fig.A.1).

The holes for placing the fibers form a matrix in a way that the light produced in the fibers of a given channel interfere the less possible to the neighbor channel. Each hole for the fibers is of 0.9 mm diameter, since the diameter of the fiber choose is of 0.83 mm. Even so, this extra space permits to leak some glue surrounding the fiber, giving more tightness to the fiber with the cookie and assuring a good vacuum seal.

The thickness of the PVC in the matrix for the fibers is of 2.5 mm, because the drill cannot make longer holes in this material without deviate the direction or broke the drill itself. This is important to take care, since this part should be polished with the high precision saw, reducing the thickness 0.5 mm in every pass.

Figure A.4 shows the technical drawing of the cookie with all specifications. Figure A.5 shows the CAD drawing of the clamping plate used to attach the PMT to the cookie.

A.2 Position matrix plate

The construction of the fiber bundles makes use of a plate with positioning grooves in order to fix the position of the fiber during their assamble. It



Figure A.1: Picture of the cookie with the clamping plates. It shows the groove for the O-ring for vacuum purposes. The hole in the middle is the place for glueing the fibers.

is made in aluminium and four pieces were manufactured in the mechanical workshop of the IKPH. The CAD drawing of the plate is shown in fig. A.6.

A.3 Supporting plate

The fiber modules are attached to an aluminium plate, designed in such a way that keeps an optimal vacuum seal and keeps the fiber plane in a fixed position thanks to clamps attached to the plate (fig. A.2). A global O-ring keeps the vacuum tight of the whole plate, meanwhile the design of the cookie with its own O-ring (app. A.1) helps to keep the vacuum seal in the individual pass-trough holes of the fiber bundles. Figure A.7 shows the CAD drawing of the supporting plate designed by J. Rosche from the IKPH.

A.4 Vacuum chamber

The vacuum chamber for the fiber hodoscope was designed as an attachment to the existing vacuum chamber of KAOS. It comprises a double purpose, support the plates of the two planes of the fiber hodoscope and serve as an adapter to the beam dump. Since the chicane will deviate the beam, to direct



Figure A.2: Left. Photography of the crimping tool to keep the verticality of the fiber plane. Right. Side photography of the fiber plane showing how the crimping tool fits the plane.

it to KAOS at 0° , the beam dump will suffer also a deviation (a scheme of the beam trajectory through the chicane and KAOS can be seen in fig. 1.12). Figure A.3 shows a photograph of the new vacuum chamber, attached to KAOS. The vacuum chamber is not symmetric respect to the dispersive plane (middle plane, parallel to floor) in order to increase the acceptance in the non-dispersive plane as can be seen in fig A.8 and fig A.9.

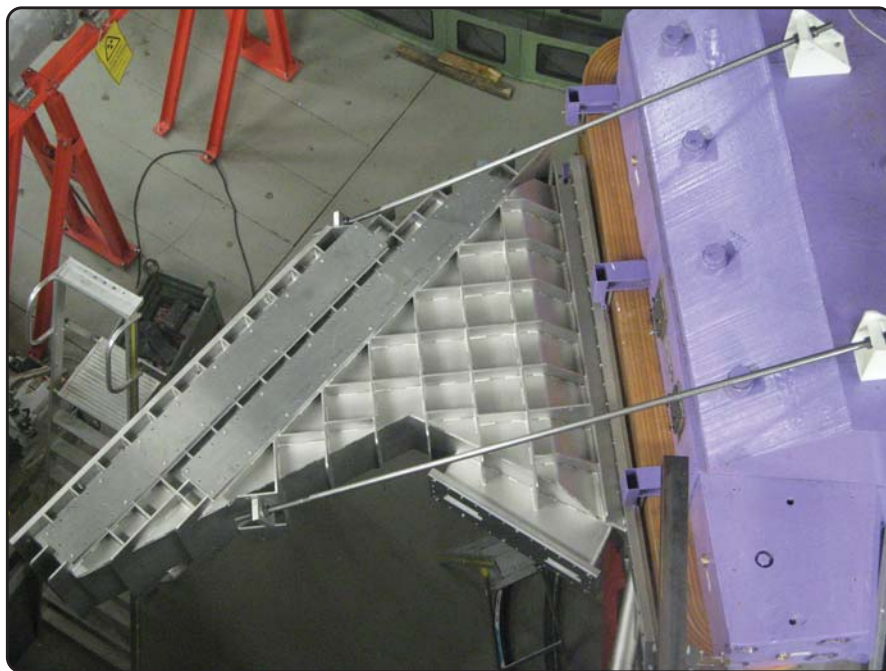


Figure A.3: Photography of the new vacuum chamber. It shows two plates, at left, were the two planes of the fiber detector will be located. In center below is located the plate were the slanted beam dump will be connected.

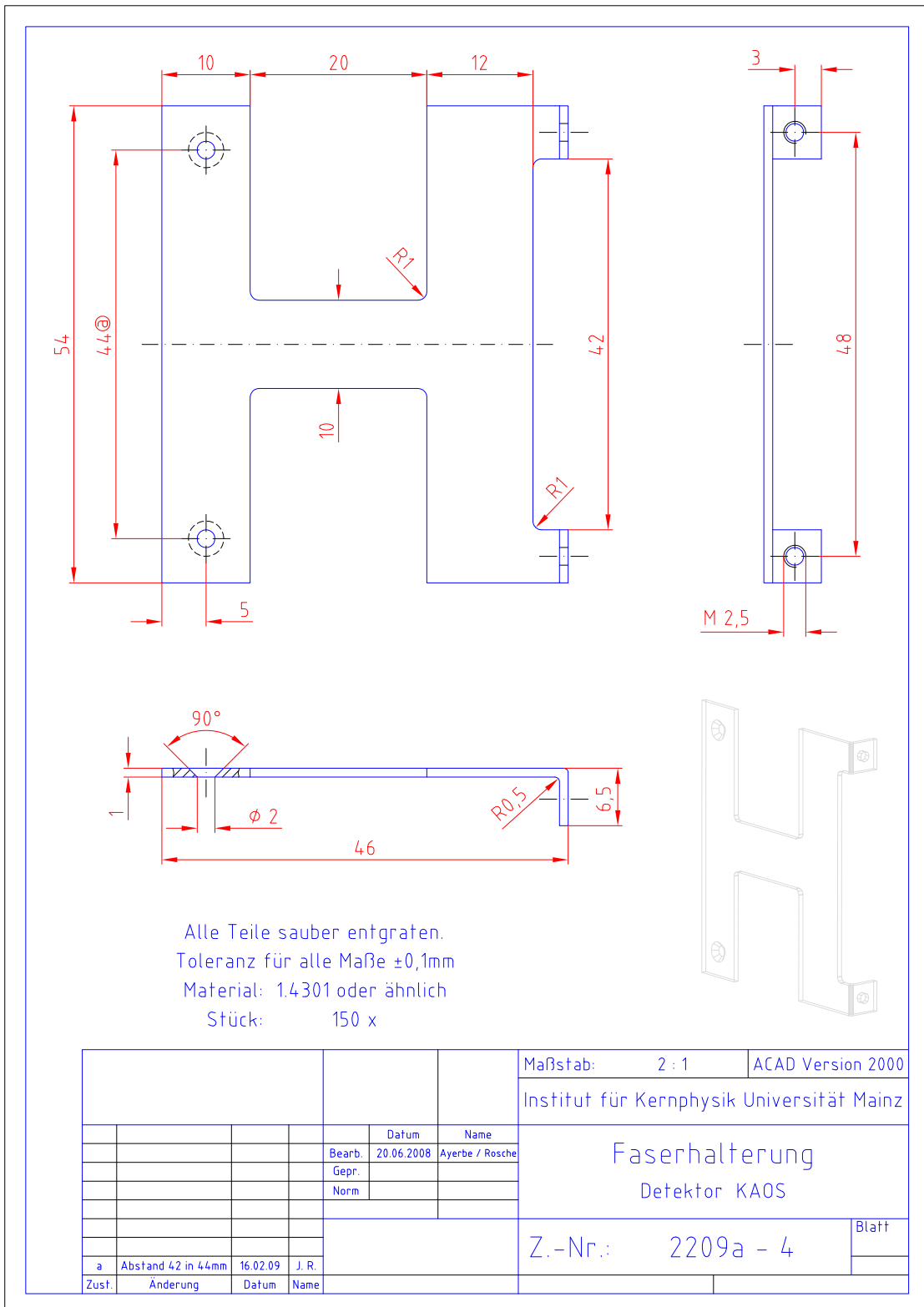


Figure A.5: Technical drawing of the of the aluminium clamping plates.

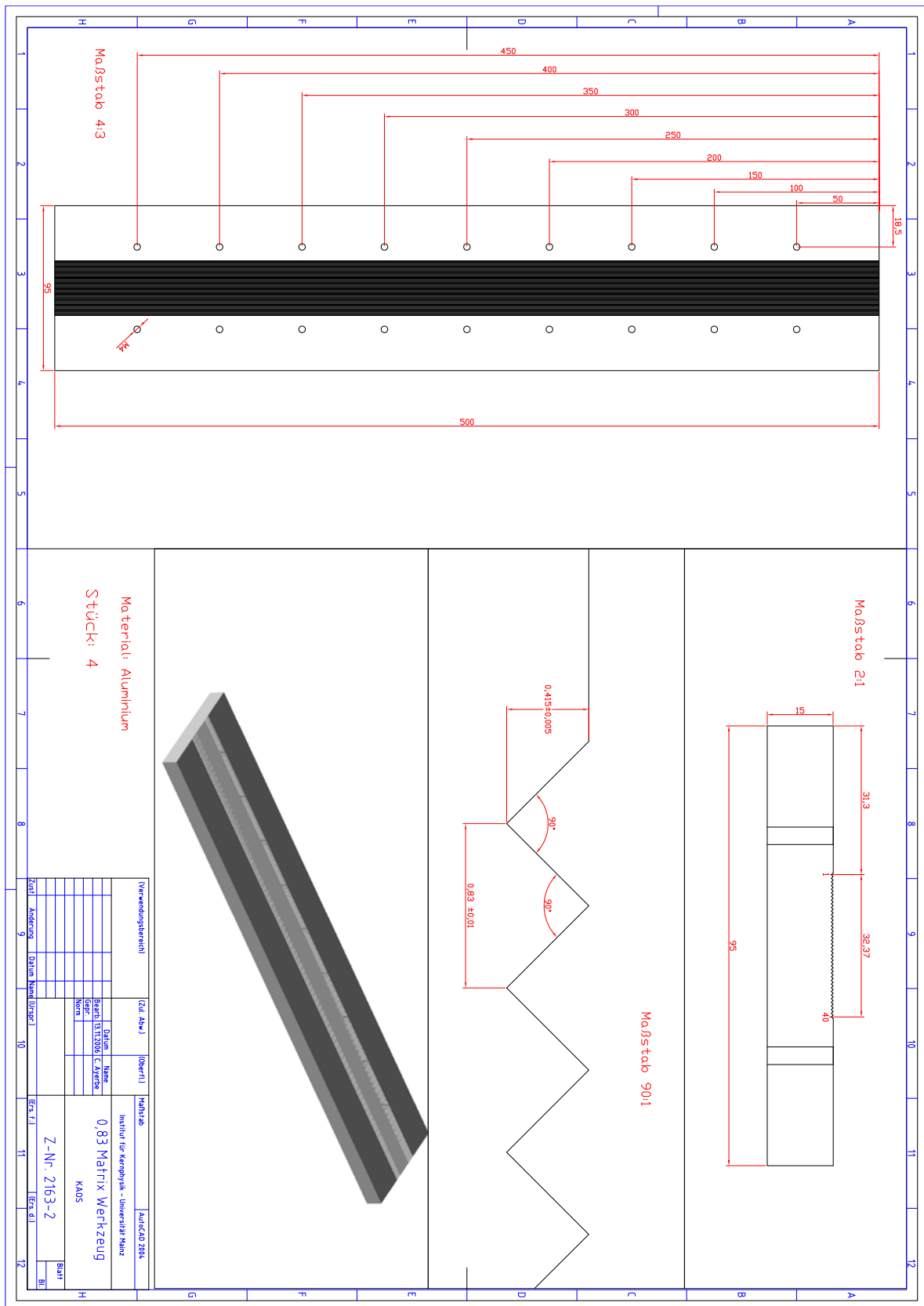


Figure A.6: Technical drawing of the supporting plate.

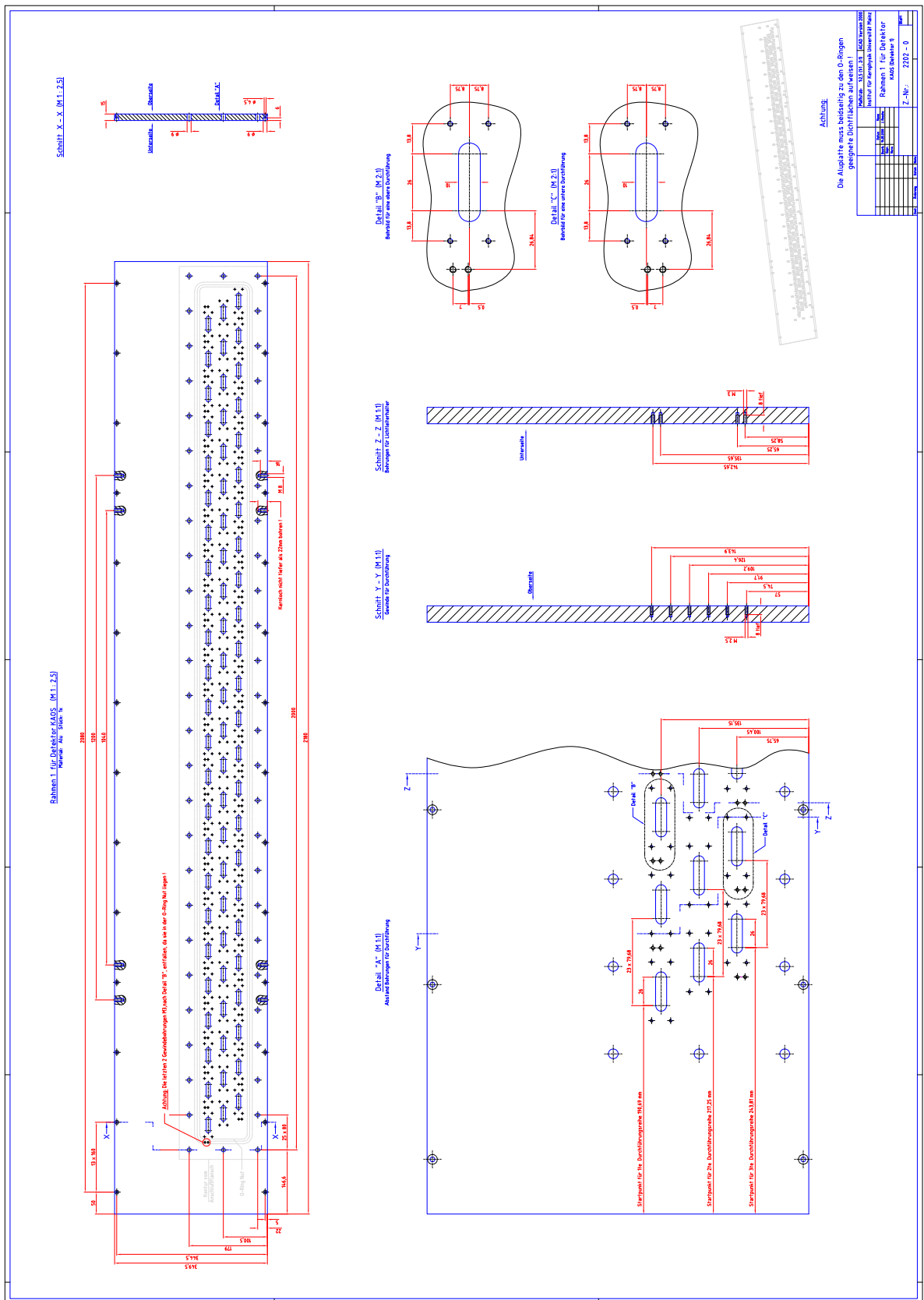


Figure A.7: Technical drawing of the supporting plate.

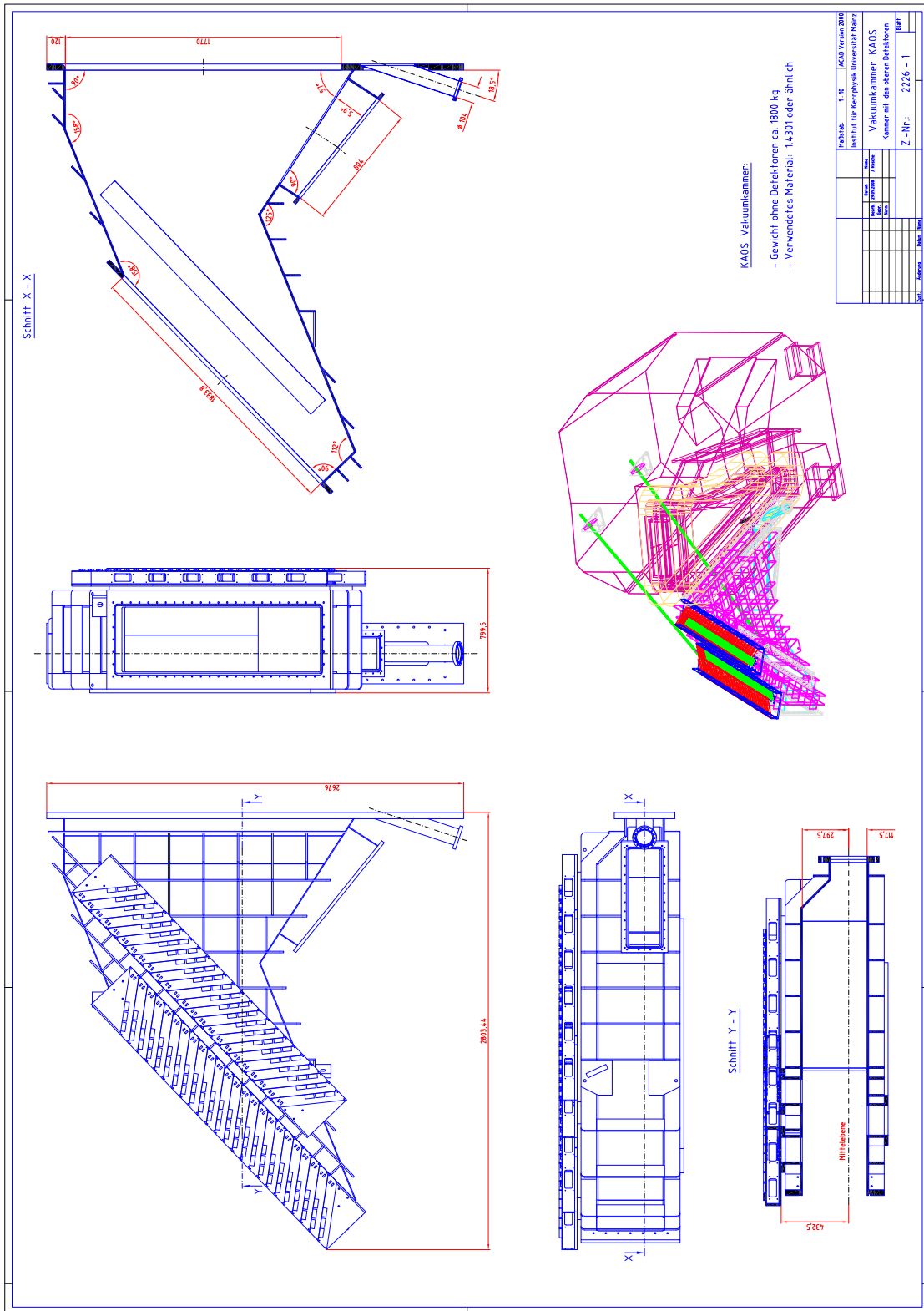


Figure A.9: Technical drawing of the new vacuum chamber.

Appendix **B**

DTD piggyback channels mapping

As was mentioned (sec. 2.3.1), to the DTD module can be attached a piggyback board (fig. 3.2) in order to obtain a full access to the analog signal from the PMT. The separation of the PMT signals in odd and even channels makes mandatory the mapping of such channels when go through the DTD.

Figure B.1 shows the scheme of the PMT channels mapping and the corresponding output through the piggyback.

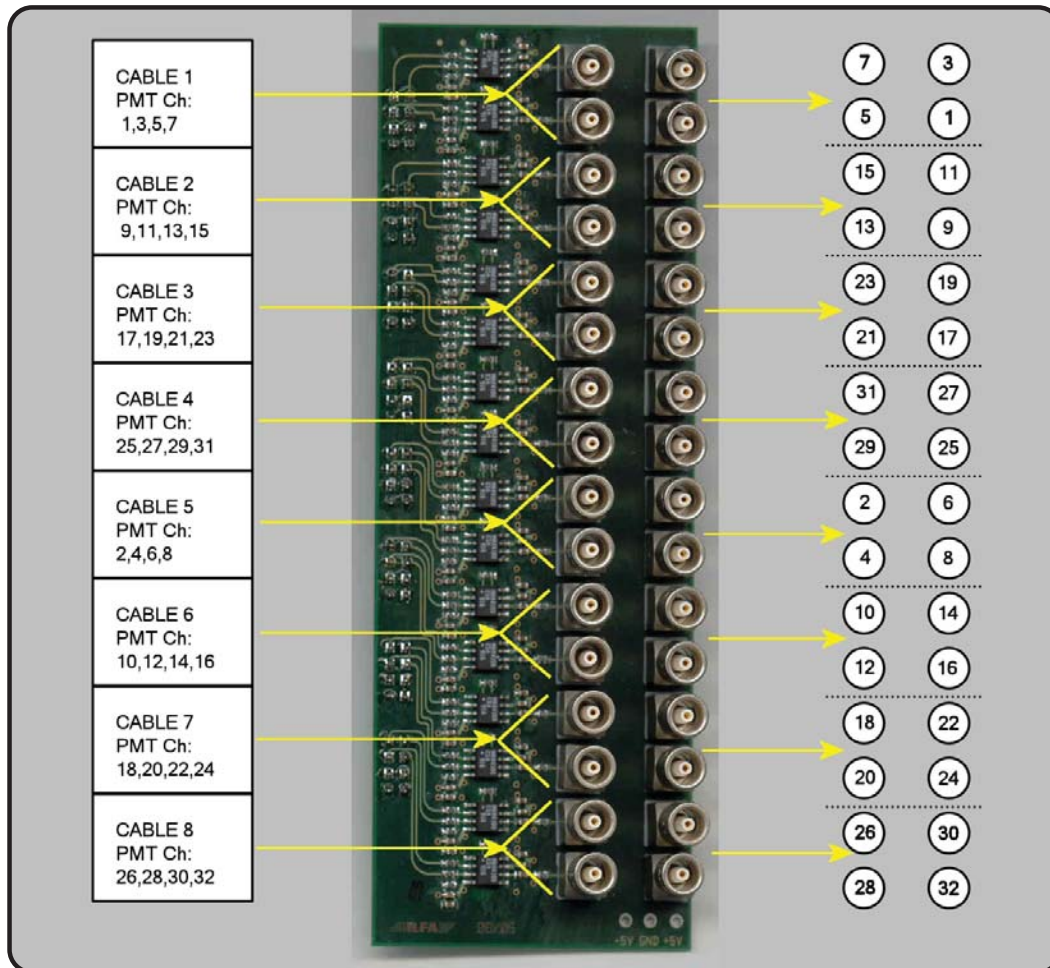


Figure B.1: Connection scheme of the DTD piggyback, showing the correct order of the PMT output through the board.

Bibliography

- [1] J. C. David, C. Fayard, G. H. Lamot, and B. Saghai. Electromagnetic production of associated strangeness. *Phys. Rev. C*, 53:2613–2637, 1996.
- [2] T. Mart and C. Bennhold. Evidence for a missing nucleon resonance in kaon photoproduction. *Phys. Rev. C*, 61:012201, 1999.
- [3] P. Vancraeyveld, L. De Cruz, J. Ryckebusch, and T. Van Cauteren. Regge-model predictions for K^+ Sigma photoproduction from the nucleon. *AIP Conference Proceedings*, 1182(1):619–622, 2009.
- [4] G. D. Rochester and C. C. Butler. Evidence for the Existence of New Unstable Elementary Particles. *Nature*, 160:855–857, 1947.
- [5] R. Armenteros, K.H. Barker, C.C. Butler, and A. Cachon. The Properties of Neutral V -Particles. *Phil. Mag.*, 42, 1951.
- [6] R. B. Leighton, S. Dean Wanlass, and William L. Alford. On the Decay of Neutral V -Particles. *Phys. Rev.*, 83(4):843–845, 1951.
- [7] Y. Nambu, K. Nishijima, and Y. Yamaguchi. On the nature of V -Particles, I,II. *Prog. Theor. Phys.*, 6(4):615–622, 1951.
- [8] K. Aizu and T. Kinoshita. On a possible model of the V -particle. *Prog. Theor. Phys.*, 6(4):630–631, 1951.
- [9] H. Miyazawa. A model for V -particles. *Prog. Theor. Phys.*, 6(4):631–633, 1951.
- [10] S. Ôneda. Note on the theory of V -particles and τ -mesons. *Prog. Theor. Phys.*, 6(4):633–635, 1951.
- [11] A. Pais. Some remarks on the V -particles. *Phys. Rev.*, 86(5):663–672, 1952.
- [12] W. B. Fretter, M. M. May, and M. P. Nakada. A study of neutral V particles. *Phys. Rev.*, 89(1):168–180, 1953.

- [13] R. B. Leighton, S. D. Wanlass, and C. D. Anderson. The Decay of V^0 Particles. *Phys. Rev.*, 89(1):148–167, 1953.
- [14] Congrès International sur le Rayonnement Cosmique. Bagnères-de-Bigorre, 1953. University of Toulouse.
- [15] E. Amaldi et al. Symbols for fundamental particles. *Il Nuovo Cimento*, 11:213–214, 1954. 10.1007/BF02782921.
- [16] T. D. Lee and C. N. Yang. Question of parity conservation in weak interactions. *Phys. Rev.*, 104(1):254–258, 1956.
- [17] C. S. Wu, E. Ambler, R. W. Hayward, D. D. Hoppes, and R. P. Hudson. Experimental test of parity conservation in beta decay. *Phys. Rev.*, 105(4):1413–1415, 1957.
- [18] M. Gell-Mann. Isotopic spin and new unstable particles. *Phys. Rev.*, 92(3):833–834, 1953.
- [19] M. Gell-Mann. The interpretation of the new particles as displaced charge multiplets. *Il Nuovo Cimento*, 4:848–866, 1956.
- [20] Tadao Nakano and Kazuhiko Nishijima. Charge independence for V -particles. *Prog. Theor. Phys.*, 10(5):581–582, 1953.
- [21] R. Plano, N. Samios, M. Schwartz, and J. Steinberger. Demonstration of the existence of the Σ^0 hyperon and a measurement of its mass. *Il Nuovo Cimento*, 5:216–219, 1957.
- [22] Luis W. Alvarez et al. Neutral cascade hyperon event. *Phys. Rev. Lett.*, 2(5):215–219, 1959.
- [23] V. E. Barnes et al. Observation of a hyperon with strangeness minus three. *Phys. Rev. Lett.*, 12(8):204–206, 1964.
- [24] M. Danysz and J. Pniewski. Delayed disintegration of a heavy nuclear fragment: I. *Philos. Mag. Series 7*, 44(350):348–350, 1953.
- [25] D.A. Tidman, G. Davis, A.J. Herz, and R.M. Tennent. Delayed disintegration of a heavy nuclear fragment: II. *Philos. Mag. Series 7*, 44(350):350–352, 1953.
- [26] J. Crussard and D. Morellet. Emission Probable d'un Fragment Nucléaire Contenant une Particule V^0 . *Comptes Rendus de l'Académie des Sciences*, 236:64, 1953.
- [27] W.B. Cheston and H. Primakoff. Remarks on the Interpretation of Unstable Heavy Fragments. in [14], page 179, 1953.

- [28] W. Cheston and H. Primakoff. "Nonmesonic" Bound V-Particle Decay. *Phys. Rev.*, 92(6):1537–1541, 1953.
- [29] M. Grilli and R. Levi Setti. Report of the committee on unstable fragments. *Il Nuovo Cimento*, 12:466–471, 1954.
- [30] W. F. Fry, J. Schneps, and M. S. Swami. Disintegration of hyperfragments. *Phys. Rev.*, 99(5):1561–1572, 1955.
- [31] M. Danysz et al. Observation of a Double Hyperfragment. *Phys. Rev. Lett.*, 11(1):29–32, 1963.
- [32] M. Y. Han and Y. Nambu. Three-Triplet Model with Double $SU(3)$ Symmetry. *Phys. Rev.*, 139(4B):B1006–B1010, 1965.
- [33] O. Hashimoto and H. Tamura. Spectroscopy of hypernuclei. *Prog. Part. Nucl. Phys.*, 57(2):564 – 653, 2006.
- [34] Carl B. Dover. Strangeness exchange reactions and hypernuclei. *Report BNL-31674*, 1982.
- [35] Patrick Achenbach. The KAOS spectrometer at the Mainz microtron and first measurements of kaon electro-production. Habilitationsschrift, Fachbereich Physik, Mathematik und Informatik der Johannes Gutenberg-Universität Mainz, 2010.
- [36] R.E. Chrien et al. States of ${}_{\Lambda}^{12}\text{C}$ Formed in the Reaction ${}^{12}\text{C} (\text{K}^-, \pi^-)$. *Phys. Lett.*, B89:31, 1979.
- [37] M. May et al. Observation of Levels in ${}_{\Lambda}^{13}\text{C}$, ${}_{\Lambda}^{14}\text{N}$, and ${}_{\Lambda}^{18}\text{O}$ Hypernuclei. *Phys. Rev. Lett.*, 47:1106–1109, 1981.
- [38] W. Bruckner et al. Hypercharge Exchange Reactions on Nuclei. *Phys. Lett.*, B55:107, 1975.
- [39] W. Bruckner et al. Spin - Orbit Interaction of Lambda Particles in Nuclei. *Phys. Lett.*, B79:157, 1978.
- [40] H. Akikawa et al. Hypernuclear fine structure in ${}_{\Lambda}^9\text{Be}$. *Phys. Rev. Lett.*, 88:082501, 2002.
- [41] M. Ukai et al. Gamma-Ray Spectroscopy of ${}_{\Lambda}^{16}\text{O}$ and ${}_{\Lambda}^{15}\text{N}$ Hypernuclei via the ${}^{16}\text{O} (\text{K}^-, \pi^- \gamma)$ reaction. *Phys. Rev.*, C77:054315, 2008.
- [42] H. Tamura, R.S. Hayano, H. Outa, and T. Yamazaki. Study of Lambda-hypernuclei with stopped K^- reaction. *Prog. Theor. Phys. Suppl.*, 117:1–15, 1994.

- [43] M. Agnello et al. First results on ${}_{\Lambda}^{12}\text{C}$ production at DAΦNE. *Phys. Lett.*, B622:35–44, 2005.
- [44] M.W. Ahmed et al. Experimental study of the ${}^{12}\text{C}(K_{\text{stopped}}^-, \pi^0)_{\Lambda}^{12}\text{B}$ reaction. *Phys. Rev.*, C68:064004, 2003.
- [45] S. Ajimura et al. Polarization and weak decays of Lambda hypernuclei produced by the (π^+, K^+) reaction on ${}^{12}\text{C}$. *Phys. Lett.*, B282:293–298, 1992.
- [46] H. Hotchi et al. Spectroscopy of medium heavy lambda hypernuclei via the (π^+, K^+) reaction. *Phys. Rev.*, C64:044302, 2001.
- [47] C. Milner et al. Observation of lambda hypernuclei in the reaction ${}^{12}\text{C}(\pi^+, K^+)_{\Lambda}^{12}\text{C}$. *Phys. Rev. Lett.*, 54:1237–1240, 1985.
- [48] T. Motoba, M. Sotona, and K. Itonaga. Photoproduction of polarized hypernuclei. *Prog. Theor. Phys. Suppl.*, 117:123–133, 1994.
- [49] John J. LeRose et al. Hypernuclear spectroscopy via $(e, e'K^+)$ in JLab's Hall A. *Nucl. Phys.*, A804:116–124, 2008.
- [50] J. Reinhold and B. Zeidman. Electroproduction of Kaons and Light Hypernuclei. Experiment E91-016, 1991. http://www.jlab.org/exp_prog/proposals/91prop.html.
- [51] D. Abbott et al. Kaon electroproduction on deuterium. *Nucl. Phys.*, A639:197–204, 1998.
- [52] R.E. Chrien, L.G. Tang, and E.V. Hungerford. Investigation of the spin dependence of the ΛN effective interaction in the p shell. Experiment E89-009, 1989. http://www.jlab.org/exp_prog/proposals/89/.
- [53] S.N. Nakamura et al. Future hypernuclear program at JLab Hall C. *Nucl. Phys.*, A754:421–429, 2005.
- [54] J. Pochodzalla. Future hypernuclear physics at MAMI-C and PANDA-GSI. *Nucl. Phys.*, A754:430–442, 2005.
- [55] S. Nozawa and T.S.H. Lee. Electroproduction of pions on the nucleon (I). *Nucl. Phys.*, A513:511–542, 1990.
- [56] C.W. Leemann, D.R. Douglas, and G.A. Krafft. The Continuous Electron Beam Accelerator Facility: CEBAF at the Jefferson Laboratory. *Ann. Rev. Nucl. Part. Sci.*, 51:413–450, 2001.
- [57] J. Alcorn et al. Basic instrumentation for Hall A at Jefferson Lab. *Nucl. Instrum. Meth. A*, 522(3):294 – 346, 2004.

- [58] B.A. Mecking et al. The CEBAF large acceptance spectrometer (CLAS). *Nucl. Instrum. Meth. A*, 503(3):513 – 553, 2003.
- [59] R. Ent. Recent results from Jefferson Lab. *Nucl. Phys. A*, 631(0):385 – 405, 1998. Few-Body Problems in Physics.
- [60] Kees de Jager. Future Research Program at JLab: 12 GeV and Beyond. *Nucl. Phys. A*, 805(1–4):494c – 501c, 2008. INPC 2007, Proceedings of the 23rd International Nuclear Physics Conference.
- [61] Elton S. Smith. The 12 GeV JLab Upgrade Project. *Nucl. Phys. A*, 827(1–4):599c – 604c, 2009. PANIC08, Proceedings of the 18th Particles and Nuclei International Conference.
- [62] Kees de Jager. Research perspectives at Jefferson lab: 12 GeV and beyond. *Nucl. Phys. A*, 737(0):301 – 305, 2004.
- [63] Wendy Latrece Hinton. Quasifree electroproduction of a Λ , Σ^0 and Σ^- hyperons on carbon and aluminium. PhD Thesis, Graduate College of Hampton University, 2001.
- [64] F. Dohrmann et al. Quasifree Λ , Σ^0 , and Σ^- electroproduction from ^1H , ^2H , ^3He , ^4He and carbon. *Phys. Rev.*, C76:054004, 2007.
- [65] J.E. Spencer and H.A. Enge. Split-pole magnetic spectrograph for precision nuclear spectroscopy. *Nucl. Instrum. Meth.*, 49(2):181 – 193, 1967.
- [66] D.J. Millener. In L. Tang and O. Hashimoto, editors, *Proceedings of the JLab Workshop on Hypernuclear Physics with Electromagnetic Probes*. Hampton University, Hampton, VA, 1999.
- [67] T. Miyoshi et al. High resolution spectroscopy of the $^{12}_{\Lambda}\text{B}$ hypernucleus produced by the $(e, e'K^+)$ reaction. *Phys. Rev. Lett.*, 90:232502, 2003.
- [68] Yuichi Okayasu. *Spectroscopic study of light Λ hypernuclei via the $(e, e'K^+)$ reaction*. PhD thesis, Department of Physics, Tohoku University, 2008.
- [69] L. Yuan et al. Hypernuclear spectroscopy using the $(e, e'K^+)$ reaction. *Phys. Rev. C*, 73:044607, 2006.
- [70] M. Iodice et al. High resolution spectroscopy of $^{12}_{\Lambda}\text{B}$ by electroproduction. *Phys. Rev. Lett.*, 99:052501, 2007.
- [71] S. N. Nakamura. Future hypernuclear experiments at JLab. In Josef Pochodzalla and Thomas Walcher, editors, *Proceedings of The IX International Conference on Hypernuclear and Strange Particle Physics*, pages 51–56. Springer Berlin Heidelberg, 2007.

- [72] P. Senger et al. The kaon spectrometer at SIS. *Nucl. Instrum. Meth. A*, 327(2):393 – 411, 1993.
- [73] P. Senger. Kaon production in nucleus-nucleus collisions. In Josef Pochodzalla and Thomas Walcher, editors, *Proceedings of The IX International Conference on Hypernuclear and Strange Particle Physics*, pages 375–380. Springer Berlin Heidelberg, 2007.
- [74] Sosuke Horikawa. The scintillating fiber tracker for the COMPASS experiment at CERN. Nuclear Physics Colloquium at RCNP, Osaka University, 2001.
- [75] S. Horikawa et al. A scintillating fiber tracker with high time resolution for high-rate experiments. *IEEE Trans. Nucl. Sci.*, 49:950–956, 2002.
- [76] A. Jankowiak et al. The first two years of operation of the 1.5 GeV cw electron accelerator MAMI C. Presented at Particle Accelerator Conference (PAC 09), Vancouver, BC, Canada, 4-8 May 2009.
- [77] B.H. Wiik and P.B. Wilson. Design of a high energy, high duty cycle, racetrack microtron. *Nucl. Instrum. Meth.*, 56(2):197 – 208, 1967.
- [78] B1 Collaboration - Mainzer Mikrotron MAMI, Johannes Gutenberg Universität Mainz. <http://www.kph.uni-mainz.de/B1/>, 2010.
- [79] T. Walcher. Physics at the electron accelerator MAMI. *Prog. Part. Nucl. Phys.*, 34:1 – 15, 1995.
- [80] A2 Collaboration - Experiments with Real Photons, Johannes Gutenberg Universität Mainz. <http://wwwa2.kph.uni-mainz.de/A2/>, 2011.
- [81] A4 Collaboration at MAMI - Parity Violating Electron Scattering, Johannes Gutenberg Universität Mainz. <http://www.kph.uni-mainz.de/A4>, 2008.
- [82] K. I. Blomqvist et al. The three-spectrometer facility at the mainz microtron mami. *Nucl. Instrum. Meth. A*, A403:263–301, 1998.
- [83] Michael Otto Distler. Aufbau und Test einer vertikaler Driftkammer. Diplomarbeit, Institut für Kernphysik, Johannes Gutenberg-Universität Mainz, 1990.
- [84] Marko Kahrau. Aufbau der vertikalen Driftkammern des Spektrometers C an MAMI. Diplomarbeit, Institut für Kernphysik, Johannes Gutenberg-Universität Mainz, 1993.
- [85] Ralph Böhm. Eichung der Szintillations-Triggerdetektoren des Spektrometers A an MAMI. Diplomarbeit, Institut für Kernphysik, Johannes Gutenberg-Universität Mainz, 1993.

- [86] Lars Nungesser. Aufbau und Simulation de KAOS-Spektrometer für Koinzidenzmessung in der assoziierten Kaonproduction. PhD Thesis, Institut für Kernphysik, Johannes Gutenberg-Universität Mainz, 2009.
- [87] A. Sartorius. Aufbau und Test einer Vieldrahtproportionalkammer zum Teilchennachweis am Kaonenspektrometer. Diplomarbeit, Technische Hochschule Darmstadt, 1991.
- [88] Georges Charpak and F. Sauli. Multiwire Proportional Chambers and Drift Chambers. *Nucl. Instrum. Meth.*, 162:405–428, 1979.
- [89] Maria del Mar Gómez Rodríguez de la Paz. Strahltest und Betrieb von Vieldrahtproportionalkammern für das Kaos-Spektrometer. Diplomarbeit, Institut für Kernphysik, Johannes Gutenberg-Universität Mainz, 2008.
- [90] Michael Bösz. Datenerfassung und Spurerkennung mit den Vieldrahtproportionalkammern für das Kaos-Spektrometer an MAMI. Diplomarbeit, Institut für Kernphysik, Johannes Gutenberg-Universität Mainz, 2009.
- [91] J. Wellendorf Pedersen, Patrick Achenbach, Salvador Sanchez Majos, and Josef Pochodzalla. Operation of Multiwire Proportional Chambers for the kaon spectrometer at MAMI. Internal Report, 2007. Institut für Kernphysik, Johannes Gutenberg-Universität Mainz.
- [92] P. Achenbach et al. Particle tracking in kaon electroproduction with cathode-charge sampling in multi-wire proportional chambers. *Nucl. Instrum. Meth.*, A641:105–113, 2011.
- [93] Andreas Wagner. Flugzeitmessungen am Kaonenspektrometer. Diplomarbeit, Technische Hochschule Darmstadt, 1992.
- [94] B. Kohlmeyer, W. Konrad, H. Pöppel, B. Schlei, and F. Pühlhofer. Status of the TOF-Detectors for the Kaon Spectrometer at SIS. Scientific Report, GSI, Darmstadt, Germany, 1989.
- [95] Patrick Achenbach, Salvador Sanchez Majos, and Florian Schulz. Operation of Multiwire Proportional Chambers for the kaon spectrometer at MAMI. Internal Report, 2011. Institut für Kernphysik, Johannes Gutenberg-Universität Mainz.
- [96] Florian Schulz. Teilchenidentifikation unter kleinen Streuwinkeln in der Pionzerfallsspektroskopie von Hyperkernen. Diplomarbeit, Institut für Kernphysik, Johannes Gutenberg-Universität Mainz, 2011.

- [97] Patrick Achenbach and Satoshi Hirose. Beam-test of a Scintillator Paddle combined with Time-of-Flight walls in the Kaos spectrometer. Internal Report, 2010. Institut für Kernphysik, Johannes Gutenberg-Universität Mainz.
- [98] Luka Debenjak. Simulation of the aerogel threshold Cerenkov counter for KAOS. Internal Report, 2008. The University of Ljubljana.
- [99] P. Achenbach et al. Strange hadronic physics in electroproduction experiments at the Mainz Microtron. *Nucl. Phys. A*, (0), 2012.
- [100] Patrick Achenbach et al. Front-end electronics for the KAOS spectrometer at MAMI. *IEEE Trans.Nucl.Sci.*, 56:316–319, 2009.
- [101] R. C. Ruchti. The use of scintillating fibers for charged-particle tracking. *Annu. Rev. Nucl. Part. S.*, 46(1):281–319, 1996.
- [102] Carsten Patrick Achenbach. Active optical fibres in modern particle physics experiments. 2004. arXiv: nucl-ex/0404008.
- [103] William R. Leo. *Techniques for Nuclear and Particle Physics Experiments*. Springer-Verlag, 1987.
- [104] C.M. Hawkes et al. Decay time and light yield measurements for plastic scintillating fibers. *Nucl. Instrum. Meth. A*, 292(2):329 – 336, 1990.
- [105] J.M. Ryan et al. A scintillating plastic fiber tracking detector for neutron and proton imaging and spectroscopy. *Nucl. Instrum. Meth. A*, 422(1-3):49 – 53, 1999.
- [106] B. Dolgoshein et al. Status report on silicon photomultiplier development and its applications. *Nucl. Instrum. Meth. A*, 563(2):368 – 376, 2006. TRDs for the Third Millenium. Proceedings of the 3rd Workshop on Advanced Transition Radiation Detectors for Accelerators and Space Applications. 3rd Workshop on Advanced Transition Detectors for Accelerators and Space Applications.
- [107] S. Sánchez Majos et al. Noise and radiation damage in silicon photomultipliers exposed to electromagnetic and hadronic radiation. *Nucl. Instrum. Meth. A*, 602(2):506 – 510, 2009.
- [108] Hamamatsu Photonics K.K. *Photomultiplier Tubes, Basics and Applications*, 3rd edition, 2007.
- [109] Dubna, Russia. *HV cells for Photomultiplier Tubes (PMT)*, 2005. Online available at http://www.hvsys.dubna.ru/pmt_cells.html.

- [110] GSI experiment electronics, Darmstadt. *Double Threshold Discriminator (DTD) Chip*, 2005. Online available at <http://www.gsi.de/informationen/tt/Double-Threshold-1.html>.
- [111] P. Abbon et al. The COMPASS experiment at CERN. *Nucl.Instrum.Meth.*, A577:455–518, 2007.
- [112] G. Braun et al. F1: An eight channel time-to-digital converter chip for high rate experiments. 1999.
- [113] J. Hoffmann, N. Kurz, S. Minami, W. Ott, and S. Voltz. Programmable Trigger Processing Module, VUPROM. Scientific Report, GSI, Darmstadt, Germany, 2007.
- [114] P. Achenbach, L. Nungesser, and J. Pochodzalla. Design criteria for multi-layered scintillating fibre arrays with inclined columns. *Nucl. Instrum. Meth. A*, 591(2):406 – 410, 2008.
- [115] S. Agostinelli et al. Geant4 - a simulation toolkit. *Nucl. Instrum. Meth. A*, 506(3):250 – 303, 2003.
- [116] S Horikawa et al. Development of a scintillating-fibre detector with position-sensitive photomultipliers for high-rate experiments. *Nucl. Instrum. Meth. A*, 516(1):34 – 49, 2004.
- [117] C. Ayerbe Gayoso. Development of a fibre detector for a kaon spectrometer at mami. Diplomarbeit, Institut für Kernphysik, Johannes Gutenberg-Universität Mainz, 2004.
- [118] P. Achenbach et al. In-beam tests of scintillating fibre detectors at MAMI and at GSI. *Nucl. Instrum. Meth. A*, 593(3):353 – 360, 2008.
- [119] Optical Society Of America. *Handbook of Optics, Vol. 2: Devices, Measurements, and Properties, Second Edition*. McGraw-Hill Professional, 2 edition, 1994.
- [120] Anselm Esser, 2011. Private communication.
- [121] Luka Debenjak. Measurements with Scintillating Fibers for Prototype Detector of Spectrometer Kaos. Diploma Thesis, University of Ljubljana, 2007.
- [122] A. Esser, P. Achenbach, C. Ayerbe Gayoso, M. Biroth, P. Gülker, and J. Pochodzalla. Characterization and calibration of a scintillating fibre detector with >4000 multi-anode photomultipliers channels. Proceedings of NDIP 2011, Lyon, France. To be published.

- [123] Michael O. Distler, Harald Merkel, and Markus Weis. Data acquisition and analysis for the 3-spectrometer-setup at MAMI. 2001. Proceedings of the 12th IEEE Real Time Congress on Nuclear and Plasma Sciences, Valencia.
- [124] Patrick Achenbach. Performance of a fiber detector in a ^{12}C beam of a 2AGeV energy at GSI. Internal Report, 2006. Institut für Kernphysik, Johannes Gutenberg-Universität Mainz.
- [125] Patrick Achenbach. Performance of a fiber detector in a ^{12}C beam of a 2AGeV energy and in a $p/\pi^+/d$ cocktail beam of 3.3tm magnetic rigidity at GSI. Internal Report, 2007. Institut für Kernphysik, Johannes Gutenberg-Universität Mainz.
- [126] P. Achenbach et al. A Large-Scale FPGA-Based Trigger and Dead-Time Free DAQ System for the Kaos Spectrometer at MAMI. *IEEE Trans.Nucl.Sci.*, 58:1677, 2011.
- [127] Anselm Esser. Teilchennachweis und Triggerung mit dem Faserdetektor im Kaos-Spektrometer am Mainzer Mikrotron. Diplomarbeit, Institut für Kernphysik, Johannes Gutenberg-Universität Mainz, 2010.
- [128] L. Schmitt et al. The DAQ of the COMPASS experiment. *IEEE Trans.Nucl.Sci.*, 51:439–444, 2004.
- [129] Eberhard Haug and Werner Nakel. *The elementary process of Bremsstrahlung*. World Scientific Lecture Notes in Physics. World Scientific, New Jersey, NJ, 2004.
- [130] G.H. Xu and E.V. Hungerford. Electron distributions in bremsstrahlung and virtual photon production. *Nucl. Instrum. Meth.*, A501:602–614, 2003.
- [131] Gideon Alexander and Iuliana Cohen. Møller scattering polarimetry for high-energy $e^+ e^-$ linear colliders. *Nucl. Instrum. Meth.*, A486:552–567, 2002.
- [132] Radha R Roy and Robert D Reed. *Interactions of photons and leptons with matter*. Academic Press, New York, NY, 1968.
- [133] Karl L. Brown. A First and Second-Order Matrix Theory for the Design of Beam Transport Systems and Charged Particle Spectrometers. *Adv. Part. Phys.*, 1:71–134, 1968.
- [134] Karl L. Brown and R. Servranckx. First and Second-Order Charged Particle Optics. *AIP Conf.Proc.*, 127:62–138, 1985.
- [135] D.C. Carey. *The optics of charged particle beams*. Accelerators and storage rings. Harwood Academic Publishers, 1987.

Curriculum Vitae

Name: Carlos Antonio Ayerbe Gayoso
Born : 03.09.1970 in Caracas - Venezuela
Address: Rheinstrasse 37
55119 Mainz
Civil status: Single

Secondary Studies:

1984 – 1986 Colegio San Agustin - Caracas
1986 – 1987 Colegio Rambam - Caracas
1987 – 1988 Colegio El Alba - Caracas

University Studies:

Sep. 1988 – Jun. 1990 Basic courses
Universidad Simon Bolivar - Venezuela
Oct. 1990 – Apr. 2001 Physics degree
in Unversitat de Valencia - Spain
01.04.2004 Diplom in Physik
in Institut für Kernphysik der Universität Mainz
From August 2004 PhD in Experimental Nuclear Physics
in Institut für Kernphysik der Universität Mainz